Characterizing the Cytotoxic Response of Three-Dimensional Microtissues using Multi-Assay Outputs and Optical Coherence Tomography

Ahbid Zein-Sabatto

Sc.M., Biomedical Engineering

Brown University, 2019

B.E., Biomedical Engineering

Vanderbilt University, 2016

A dissertation submitted in partial fulfilment of the requirements for the degree of Doctor of Philosophy in Biomedical Engineering at Brown University

Providence, Rhode Island

October 2025

This dissertation by Ahbid Zein-Sabatto is accepted in its present form by the Department of Biomedical Engineering as satisfying the dissertation requirement for the degree of Doctor of Philosophy.

Date_____ _____
Jonghwan Lee, Ph.D., Advisor

Recommended to the Graduate Council

Date_____ _____
Eric M. Darling, Ph.D., Reader

Date_____ _____
Diane Hoffman-Kim, Ph.D., Co-Advisor & Reader

Date_____ _____
Jeffrey R. Morgan, Ph.D., Reader

Date_____ _____
Kimani C. Toussaint, Ph.D., Reader

Approved by the Graduate Council

Date_____ _____
Thomas A. Lewis, Ph.D., Dean of the Graduate School

CURRICULUM VITAE

Ahbid Zein-Sabatto | ahbid_zein-sabatto@brown.edu

Education

Doctor of Philosophy, Ph.D. Biomedical Engineering May 2025
Brown University, Providence, Rhode Island

Master of Science, Sc.M. Biomedical Engineering May 2019
Brown University, Providence, Rhode Island

Bachelor of Engineering, B.E. Biomedical Engineering May 2016
Vanderbilt University, Nashville, Tennessee

Publications

Calvao, D., Vecchio, F., Ocitti, M., **Zein-Sabatto, A.,** Schmidt, A., Shub, M., Kesari, H., Viapiano, M., Lawler, S., & Hoffman-Kim, D. A brain-cancer microtissue model for studying tumor cell behavior and cancer-neural cell interactions. *Sci. Rep.* Under Review.

Zein-Sabatto, A., St. Angelo, K., Madnick, S., Hoffman-Kim, D., Morgan, J.R., & Lee, J. Multi-assay assessment of cytotoxicity reveals multiple mechanisms of action in 3D microtissues. *Sci. Rep.* **15**, 3090 (2025).

Makowski, A.J., Pence, I.J., Uppuganti, S., **Zein-Sabatto, A**., Huszagh, M.C., Mahadevan-Jansen, A., & Nyman, J.S. Polarization in Raman spectroscopy helps explain bone brittleness in genetic mouse models. *J. Biomed. Opt.* **19**, 117008 (2014).

Nyman, J.S., Gorochow, L.E., Horch, R.A., Uppuganti, S., **Zein-Sabatto, A**., Manhard, M.K., & Does, M.D. Partial removal of pore and loosely bound water by low-energy drying decreases cortical bone toughness in young and old donors. *J. Mech. Behav. Mater.* **22**, 136–145 (2013).

Presentations

Zein-Sabatto, A.*, Bico, A., Woo, M., Fariha, R., Ip, B., Hoffman-Kim, D., Morgan, J., Lee, J. (2024, April). *OCT viability imaging of 3D microtissues* [Conference Presentation] Optica Biophotonics Congress: Biomedical Optics, Fort Lauderdale, Florida, United States.

Zein-Sabatto, A., Lee, S.J., Kuhn, M., Aponte, I., Felalaga, B., Sevetson, J., Ip, B., Hoffman-Kim, D., Morgan, J., Lee, J.* (2019, March). *Label-free cellular viability imaging in 3D tissue spheroids with dynamic optical coherence tomography* [Conference Presentation]. SPIE BiOS, San Francisco, California, United States.

Makowski, A.J.*, Uppuganti, S., **Zein-Sabatto, A.**, Huszagh, M., Granke, M., & Nyman, J.S. (2014, March). *Loss in Tissue Heterogeneity Corresponds with the Age-Related Decrease in Fracture Toughness of Bone.* [Poster Presentation]. Orthopedic Research Society Annual Meeting, New Orleans, Louisiana, United States.

Makowski, A.J.*, Uppuganti. S., **Zein-Sabatto, A.**, Whitehead, J., Granke, M., Mahadevan-Jansen, A., & Nyman, J.S. (2013, October). *Measuring Bone Heterogeneity with Raman Spectroscopy to Explain Aging Differences in Human Fracture Toughness*.

[Poster Presentation]. American Society for Bone and Mineral Research Annual Meeting, Baltimore, Maryland, United States.

Granke, M.*, Uppuganti, S., Makowski, A.J., **Zein-Sabatto, A.**, Schultze, A.K., Whitehead, J, & Nyman, J.S. (2013, October). *Does Reference Point Indentation Assess the Fracture Toughness of Human Cortical Bone?* [Poster Presentation]. American Society for Bone and Mineral Research Annual Meeting, Baltimore, Maryland, United States.

Makowski, A.J.*, Uppuganti, S., **Zein-Sabatto, A.**, Yang, X., Rowland, B.J., & Nyman, J.S. (2013, January). *Transcription Factor ATF4 Regulates the Fracture Resistance of Bone.* [Poster Presentation]. Orthopedic Research Society Annual Meeting, San Antonio, Texas, United States.

(*) Indicates presenting author

Patents

Hicks A, Fross B, Mendoza J, Piper L, Schlunk S, Stedman E, **Zein-Sabatto A**. Systems, Devices, and Methods for Administering Low-Level-Light Therapy. U.S. Patent Application 2018/0304094 A1. Publication Date: Oct. 25, 2018.

Teaching and Mentorship Experience

Teaching Assistant, ENGN 1930B Biomedical Optics Spring 2020, 2021, & 2023
Brown University, Providence, Rhode Island
Instructor: Dr. Jonghwan Lee
Assisted instructor in grading assignments and lab reports
Hosted regular office hours to support and enhance student learning

Professional Tutor, Bridges to Belmont Jan 2017-Apr 2017

Belmont University, Nashville, Tennessee

Supervisor: Dr. Nadi Bishop

Tutored undergraduate students in various subjects

Assisted students in developing studying and note-taking techniques

Student Outreach, Vanderbilt Student Volunteers for Science Aug 2012-May 2016

Vanderbilt University, Nashville, Tennessee

Supervisor: Patricia C. Tellinghuisen

Maintained and replenished science experiment kits used by middle school students in the Nashville metropolitan area and surrounding counties

Conducted in-class science experiments to enrich teaching curriculum

Directed and trained peers to enhance workflow

Research Experience

Graduate Research Assistant Aug 2017- May 2025

Department of Biomedical Engineering, Brown University, Providence, Rhode Island

Advisors: Dr. Jonghwan Lee & Dr. Diane Hoffman-Kim

Evaluated the use of high-throughout, noninvasive, and label-free OCT imaging techniques to assess cellular viability of 3D cell cultures

Implemented multivariate statistical approaches to analyze multi-assay data

Established tissue culture capabilities in a newly acquired research space and facilitated the training of incoming students

Undergraduate Researcher Jun 2015-Aug 2015

Searle Undergraduate Research Program, Vanderbilt University, Nashville, Tennessee

Advisors: Dr. Matthew Walker III, Dr. Amanda Lowery, & Dr. Christina Marasco

Designed and developed a medical device that utilizes low level light therapy to treat chronic diabetic foot ulcers

Undergraduate Research Assistant Jan 2011-Aug 2013

Department of Orthopedic Surgery, Vanderbilt University, Nashville, Tennessee

Advisor: Dr. Jeffry S. Nyman

Investigated the effects of age, disease, genetics, and other factors on bone toughness

Advanced the understanding of bone fractures and their predictors in high-risk patients

Honors and Awards

Thomas G. Arnold Prize for Biomedical Engineering System Design May 2016

Vanderbilt University, Department of Biomedical Engineering

Nashville, Tennessee

Best in Healthcare Award Apr 2016

Vanderbilt University, Senior Design Day

Nashville, Tennessee

ACKNOWLEDGMENTS

It has been a blessing and honor to be supported by wonderful mentors, colleagues, family, and friends throughout my academic journey. Thank you, Dr. Jonghwan Lee, for being an amazing advisor and welcoming me into your lab. Your extraordinary mentorship, guidance, and knowledge established a research environment that allowed me to thrive. Your kindness and support made my time at Brown genuinely delightful. Thank you, Dr. Diane Hoffman-Kim, for co-advising me and also welcoming me into your lab. I am truly grateful for the opportunities that were made possible by your commitment to fostering rigorous research and kindness. Thank you, Dr. Jeffrey Morgan, for your invaluable contributions to this collaborative research. Your expertise and insight propelled my research and critical thinking to the next level. I also want to extend my heartfelt gratitude to Dr. Eric Darling and Dr. Kimani Toussaint for serving on my committee, providing vital feedback, and sharing thoughtful scientific discussions. This research would not have been possible without the help and support from Dr. Blanche Ip, Dr. Samantha Madnick, Katerina St. Angelo, and Madeleine Marx.

I would like to thank the members of the Lee and Hoffman-Kim labs for their friendship, support, and thoughtful discussions. I am lucky to have you as colleagues. A special thanks to Daniel Chait, Yuwei Liu, and Luke Xu for being amazing team members and to lab alumni Adrian Bico, Madison Woo, and Dr. Ramisa Fariha for their early contributions to this research.

Finally, I would like to thank my family and friends for their everlasting love and support. I am eternally grateful for all of you.

TABLE OF CONTENTS

LIST OF TABLES

LIST OF FIGURES

CHAPTER 1: INTRODUCTION

1.1 Cancer Overview

1.1.1 Background and Epidemiology

The human body is made up of tens of trillions of cells responsible for maintaining and sustaining life.[1] Healthy cells regularly replicate to replace aging or damaged cells in a controlled manner; however, genetic mutations may deregulate this process resulting in uncontrollable proliferation. Solid tumors may form when these abnormal and highly proliferative cells amass. Tumors may be classified as benign or malignant depending on their growth rate, morphology, and potential for metastasis.[2] If left unchecked, malignant tumors can spread to other parts of the body, disrupt essential organ functions, and cause death. The diseases characterized by this pathophysiology are known as cancer.

The American Cancer Society (ACS) alongside the National Cancer Institute (NCI) provide annual reports regarding the healthcare impact of cancer in the United States. In 2024 alone, there were approximately 2,001,140 new cancer cases and 611,720 cancer fatalities in the United States.[3] It was also estimated that roughly 40% of people in the United States will be diagnosed with cancer in their lifetime.[3] Breast, prostate, lung, and colorectal cancers were among the most common sites for cancer (in descending order).

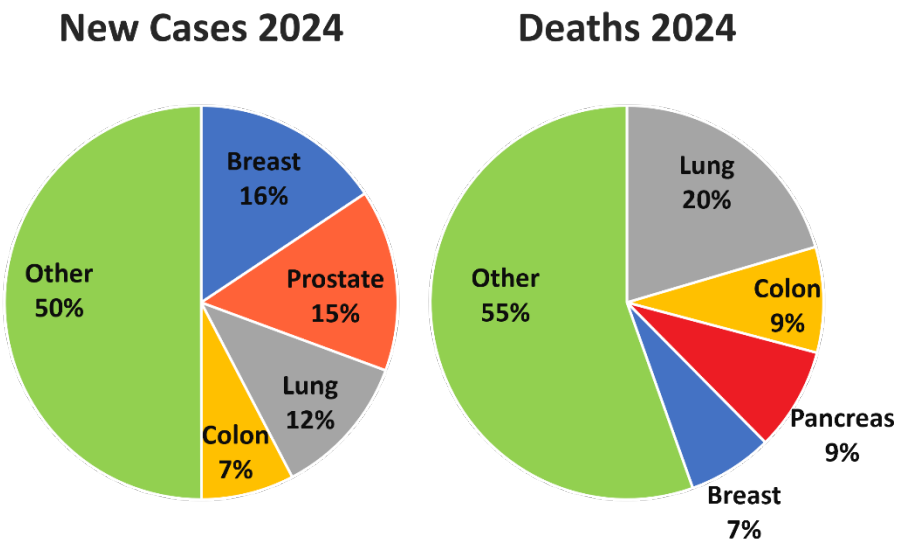

Figure 1. Selected statistics from the 2024 National Cancer Institute's Surveillance, Epidemiology, and End Results Program. The four cancer sites responsible for the most new cases (left) and deaths (right) were reported as a percentage of all cancers.

Nevertheless, lung cancer disproportionately accounted for the most deaths among men and women (Fig. 1). Despite the overall decrease in cancer mortality, incidence rates from 2015-2019 annually increased by 0.6%-1% for breast, pancreas, and uterine corpus cancers and by 2%-3% annually for prostate, liver, and kidney cancers.[3] The epidemiological data collected by the ACS and NCI highlight the current healthcare burden imposed by cancer and emphasize the projected increase in prevalence for the near future. Advancements in cancer prevention, detection, and treatment will be crucial to counteract this challenging disease.

1.1.2 Advancements in Cancer Therapy

Conventional Therapy

Prior to the 1900s, cancer therapy heavily relied on resection and cauterization as the only means of treatment.[4] Advancements in the early to mid-1900s saw the introduction of radiotherapy and chemotherapy. Many new cancer therapies have emerged and revolutionized the pharmaceutical industry over recent years; nevertheless, resection, radiation, and chemotherapy remain as the fundamental basis for cancer therapy. The primary scope of this thesis will focus on pharmacological approaches for cancer treatment.

Chemotherapies cover a broad range of pharmacologically active compounds that aim to inhibit tumor cell proliferation through cytotoxic mechanisms. Many classes of chemotherapies are approved for various cancer types including alkylating agents, antimetabolites, and taxanes. According to the Food and Drug Administration (FDA) database, mechlorethamine hydrochloride (nitrogen mustard) was the first chemotherapy approved in 1949. This organic compound is classified as an alkylating agent. Alkylating agents target DNA through intercalation and crosslinking which ultimately results in the inhibition of DNA replication and repair.[5–7] Antimetabolites such as purine and pyrimidine analogs permeate into cells and compete with normal metabolites of DNA to inhibit replication.[7,8] At higher concentrations, these analogs may be inserted into DNA more frequently. Ultimately, when these analogs accumulate, they improperly trigger DNA mismatch repair and form DNA fragments leading to apoptotic cell death.[7,8] Taxanes form another class of drugs that disrupt the polymerization or depolymerization of microtubules within the cell.[7,9] The cell's failure to form a mitotic spindle during M-phase prevents it

from dividing and results in cell death.[7] In general, the cytotoxic properties of chemotherapies differentially impact faster replicating cells like tumors; however, they are commonly associated with systemic toxicity and negative side effects.

Traditionally, chemotherapies have been administered following recommended guidelines developed by oncologists based on population metrics and broad clinical trials. One retrospective study estimated that 52.3% of patients eligible for chemotherapy will respond positively to their first-line treatment.[10] The variability in treatment response may be explained by inter and intra tumor heterogeneity found across all cancers.[11] This characteristic property of tumors has shifted the foundations of cancer treatment toward a more patient-centric approach.

Precision Oncology

One approach to improve patient response to cancer treatment involves precision oncology. Precision oncology relies on identifying key, patient-specific markers that drive tumorigenesis. Genes, environmental factors, and lifestyle choices are evaluated for each individual patient to provide them with the most appropriate treatment regimen. Technological advancements in gene sequencing, proteomics, and metabolomics have given precision medicine initiatives momentum in the fight against cancer.[12] Most notably, tumor gene sequencing has provided great insight towards uncovering biological mechanisms driving tumorigenesis.[13] The ability to identify the specific protein interactions, signaling cascades, and immunogenic factors that contribute to cancer development is crucial for targeted therapeutic approaches. Under precision oncology, a patient with breast cancer would receive a genetic screen to identify which tumor subtype

they express: Luminal A, Luminal B, human epidermal growth factor receptor 2 (HER2)-positive, or triple-negative breast cancer.[14] A patient with HER2-positive cancer may receive Trastuzumab (a HER2 inhibitor) while a patient with triple-negative cancer would be eligible for Olaparib (a PARP inhibitor).[14–16] Ultimately, the patients would be given a treatment with the maximal therapeutic capacity tailored specifically to their cancer.

Genomic-based precision oncology has its share of limitations. Most notably, precision approaches underestimate the genetic heterogeneity of tumors. In breast cancer, ~50% of genetic variants that predispose patients to tumor formation are unexplained.[17] Patients with unexplained mutations cannot be matched with a targeted therapy and would receive traditional first-line therapy instead. Systemic analysis of over 4,000 cancers from The Cancer Genome Atlas (TCGA) revealed that 18% of cases had one or more rare mutations in 624 genes associated with cancer.[18] Similarly, a study conducted on the TCGA found that solid tumors have approximately 30 cancer-related alterations, but only 17% of them can be targeted.[19] Another study conducted on 4,068 pan-cancer samples identified only 241 cases (5.9%) that had FDA-approved drugs following their primary indications.[20] It is currently impractical for the drug discovery pipeline to develop targeted therapies for all genetic variants of tumors. Challenges associated with genetic heterogeneity also extend to intratumor variability. Multiregional sequencing of four tumors revealed spatially unique somatic mutations leading to phenotypic intratumor diversity.[21] Sampling bias may lead to incomplete genetic profiling and the selection of partially effective therapies. Finally, genetic screens captured at a single timepoint do not predict clonal evolutionary branching due to genomic instability, extrinsic factors, or iatrogenic pressure.[22,23]

Functional Precision Medicine

Unlike precision oncology, functional precision medicine (FPM) aims to empirically test the effectiveness of treatments using patient-derived samples and predictive biomarker screens (Fig. 2).[24] This approach has the potential to predict the phenotypic patient-drug response in a relatively short amount of time. It would also enable oncologists to simultaneously assess the performance of multiple drug regimens for each patient. Different combinations, concentrations, and sequences of treatments can be tested using FDA approved drugs, drugs undergoing clinical trials, and molecularly relevant drugs repurposed outside their primary indication. This is advantageous for patients since they would be pre-screened and treated with the best available therapy for their tumor (Fig. 2).

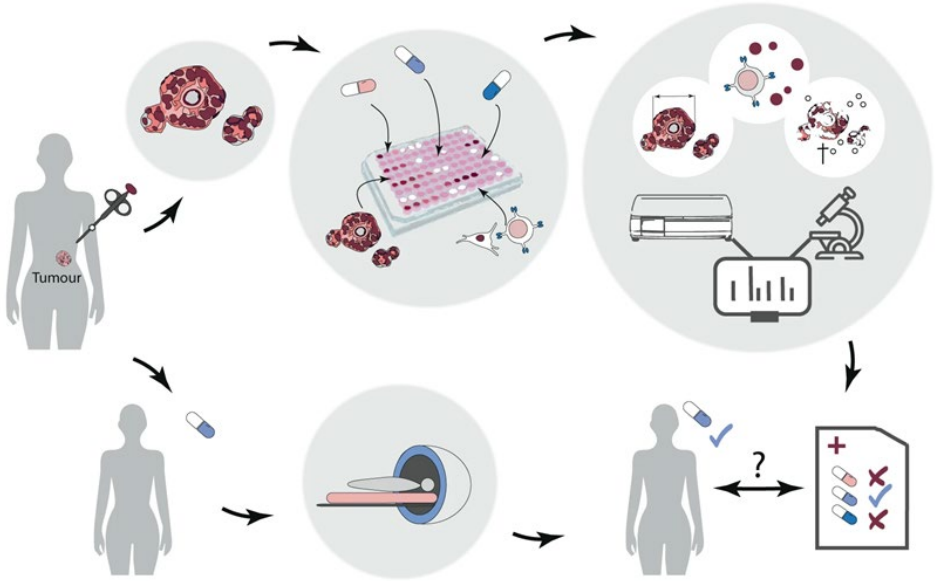

Figure 2. Illustration of functional precision medicine in oncology. Tumor cells are first extracted from the patient via a biopsy and cultured *in vitro* (top left, clockwise). Once cultured, a variety of therapies can be screened directly in the cells. Various predictive biomarker tests can be implemented to identify which candidate therapy has the best therapeutic potential in the patient. The efficacy of the treatment can be confirmed using medical imaging techniques. Adapted from Wensink G.E., et al., 2021.

Technological Challenges Limiting FPM Implementation

FPM requires the growth and culture of tumor cells extracted from patient biopsy tissue. Human tumor cells are relatively easy to culture in two-dimensional (2D) *in vitro* models; however, many studies have challenged their ability to reliably mimic the clinical response.[25–27] 2D cultures are generally more sensitive to treatments, do not recapitulate the native tumor microenvironment, and have altered gene expression that challenge their clinical relevance.[28,29] Patient-derived xenograft (PDX) models address these *in vitro* challenges and are commonly established by engrafting human tumor cells into an immunodeficient rodent.[30] Successful engraftments result in tumor vascularization and proliferation. PDX models have been shown to consistently and reliably predict clinical outcomes of the tumor drug response in patients.[31–33] The high clinical relevance of PDX models is due to their ability to maintain similar tumor microenvironments, gene expressions, and mechanisms of chemoresistance found in the original patient tumor.[31,34] Nevertheless, the widespread implementation of PDX models for FPM applications is challenging. Successful tumor take rates depend on cancer type and vary from ~60% for colorectal cancer, 15-24% for breast cancer, and 10-15% for prostate cancer.[34–36] Ethical concerns, cost, and resources involved in PDX platforms are nontrivial and preclude its widespread implementation in FPM. As a result, there is a critical need for the development of testing platforms that are easily scalable and accurately predict the patient drug response.

The successful implementation of FPM will also depend on analyzing drug screening outputs using a high-throughput approach. Cell viability assays are commonly used tools to assess cell health and rely on quantifying the presence of certain biomarkers within a sample. Many assays employ colorimetric changes, fluorescent tagging, or

enzyme-substrate interactions to produce an output signal. This is often achieved through the addition of exogenous reagents with cytotoxic properties (e.g., propidium iodide and trypan blue) or the implementation of cell lysis in their protocols (e.g., CellTiter-Glo ATP assay). Terminal assays provide viability data from a single timepoint; therefore, temporal changes in viability are captured by increasing the sample size and sequentially analyzing a subset of the population over time. Furthermore, multiple terminal assays cannot be conducted within the same sample. This is also addressed by increasing the sample size and allocating subsets of the sample population to each assay. If these traditional cell viability assays are implemented, then high-throughput FPM applications will require sufficiently large sample sizes for an effective screen. This is a major challenge facing FPM since patient biopsy sizes can be limited.[37,38] Live-cell imaging dyes help circumvent these limitations; however, they are susceptible to photobleaching and phototoxicity.[39] Next-generation luminescence assays that offer multiplexing compatibility are becoming more available. These assays can provide continuous readouts from the same sample for up to 72 hours; however, there are associated limitations.[40] One limitation involves the depletion of enzyme pro-substrates in metabolically active cells over time.[40] This requires the careful calibration of cell seeding density and incubation time to ensure the assay output remains linear as cells continue to proliferate. Another limitation of assays, particularly those that require substrates to permeate into live cells, involves efflux pumps. P-glycoprotein, an efflux pump commonly attributed to multidrug resistance in tumors, has been shown to actively reduce the accumulation of dyes and other probes within the cell.[41,42] These challenges highlight the second obstacle to implementing FPM which necessitates the development of viability testing that can be applied to limited sample sizes without

sacrificing analytical outputs. Ideally, this approach should be sensitive, nondestructive, and feasible for longitudinal high-throughput screening (HTS) applications.

1.2 Addressing FPM Challenges

1.2.1 Three-Dimensional In Vitro Models of Cancer

The development of next-generation, three-dimensional (3D) culturing platforms has transformed disease modeling, drug discovery, and tissue engineering. These models help address the technological gap between traditional 2D *in vitro* and complex *in vivo* models. Compared to 2D models, 3D culturing platforms better emulate the microenvironment found *in vivo* while maintaining the high-throughput and cost-effective nature of the *in vitro* model.[43,44] Several studies have emphasized the improved clinical relevance of 3D models and their ability to maintain *in vivo*-like cellular characteristics including morphology, proliferation, gene expression, protein synthesis, and drug response.[25–29,43–45] Patient-derived organoids (PDOs) have been crucial for FPM feasibility studies. PDOs are formed by extracting tumor cells from a patient's biopsy followed by enzymatic and mechanical dissociation. Single-cell suspensions are most commonly seeded in 3D Matrigel; however, they can also be grown in basement membrane extracts, air-liquid interfaces, and in self-assembling suspensions.[46] PDOs have been cultured from a variety of cancers including those from the most lethal sites (i.e., lung, colorectal, pancreas, breast, and brain).[46–49] Similar to PDX models, the success rates for different cancers may vary; however, optimizing media or imposing stricter quality control guidelines during harvest may improve culture success rates. Some common complications

for creating PDOs include insufficient tumor cell count, bacterial infection of tissue, and prior treatment with radiotherapy.[47,48]

The implementation of PDOs for chemotherapy screening is promising. One study predicted patient response to therapy with 100% sensitivity and 93% specificity in metastatic gastrointestinal cancers.[50] A study conducted on pancreatic cancers also found that PDOs derived from treatment naïve and previously treated tumors predicted the patients' response to neoadjuvant therapy with 100% and 71% accuracy, respecitvely.[47] The predictive power of PDOs is not absolute. A study conducted on metastatic colorectal cancer had an accuracy of ~80% at predicting monotherapy patient response but was unable to predict the response of fluorouracil-oxaliplatin combinatory therapy.[48] Nuances in the tumor microenvironment between the PDO model and source tumor including the absence of stroma and an immune system in the PDOs were hypothesized to be potential explanations for the observed discrepancy.[48] It is also important to note that a single assay output was used to analyze the efficacy of all the treatments; consequently, a single assay approach may be unable to accurately predict the complex response from combinatory therapies. Further improvements to the accuracy and sensitivity of the FPM chemotherapy screen may involve the implementation of multi-metric approaches to comprehensively assess changes to cell viability.

Although patient-derived tissues are best suited for FPM applications, this study exclusively generated 3D cultures using cell line tumors and primary neonatal cortical tissue. The 3D Petri Dish (24-96 small spheroids, Microtissues Inc) culturing platform was selected due to its ease of use, reproducibility, and scalability. Ultimately, the study findings can be adapted to a variety of culture methods and tissue types. Overall, 3D *in vitro*

culturing platforms address many limitations associated with the implementation of large-scale screens while maintaining the clinical relevance necessary to predict patient treatment outcomes.

1.2.2 Optical Coherence Tomography Viability Imaging

Advancements in 3D *in vitro* cultures have not been met with improvements in analytical approaches used to assess cell viability. In addition to the challenges mentioned in *Section 1.1.2: Advancements in Cancer Therapy*, conventional cell viability assays are not optimized for 3D cultures. Assays that rely on the uptake of labeling molecules do not efficiently resolve core regions of 3D samples. This may be due to a variety of factors including diffusion-dependent penetration of the molecules, imaging depth of the optical system, and light scattering properties of the tissue.[51,52] Moreover, current HTS viability assays cannot accomplish region-specific analysis of 3D cultures which underutilizes the physiologically relevant differences caused by nutrient, pH, and metabolic gradients within the sample.[53,54] These metabolic zones are known factors of tumor heterogeneity that impact the tumor drug response.[55,56] Finally, implementing multiple assays in a HTS study is challenging. To our knowledge, many published studies focused on one analytical output which diminishes their ability to holistically measure cell viability.[46-50]

This study proposes to overcome these challenges through the development and optimization of optical coherence tomography (OCT) viability imaging in 3D cultures. Changes in optical scattering properties between live and dead cells form the foundational premise behind OCT viability imaging. Organelles and other subcellular components

contribute to the scattering profile of cells, and changes to their morphology due to decreased viability could impact the cell's scattering profile.[57–61] Cells undergoing apoptotic or necrotic cell death display morphological characteristics that are optically distinguishable (Fig. 3).[62] Apoptotic cell death is induced by cell signaling and is carried out by caspase pathways that result in cytoplasmic shrinkage, nuclear fragmentation, and the formation of dense apoptotic bodies;[63,64] meanwhile, necrotic cell death may be induced by environmental injuries and are associated with increased membrane permeability, cellular swelling, and the expulsion of organelles (Fig. 3).[64,65]

Another characteristic of viable cells involves the presence of ATP-dependent motion and trafficking. Dead cells are metabolically inactive and terminate all intracellular motility. Previous studies have investigated whether OCT metrics are sensitive to differences in optical scattering and intracellular motility. OCT metrics that measure the intensity of backscattered light,[63,66–68] optical scattering attenuation,[69–73] spheroid geometry,[74,75] and time-dependent changes in signal (i.e., autocorrelation decay or signal decorrelation)[76–81] have all been investigated as promising indicators of viability.

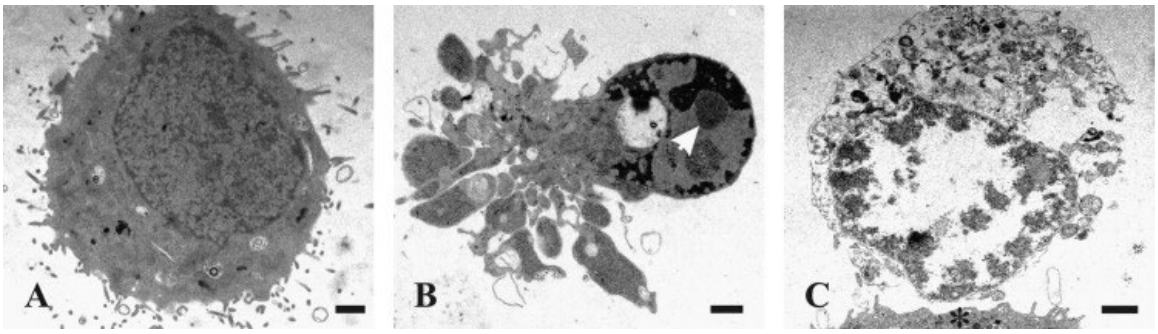

Figure 3. Transmission electron microscopy images of fibrosarcoma cells. (a) A healthy, unstimulated fibrosarcoma cell maintained its spherical appearance with smooth nuclei and well-preserved organelles. (b) Fibrosarcoma cell exposed to agonistic anti-Fas for one hour induced apoptotic cell death. Dense apoptotic bodies formed, and nuclear condensation (white arrowhead) occurred. (c) Fibrosarcoma cell exposed to human TNF for seven hours induced necrotic cell death. Cellular features were swollen and spread apart due to significant deterioration of the plasma membrane. A nearby macrophage (asterisk) can be seen at the bottom of the image. Scale bars: 1 μm. Adapted from Krysko D.V., et al., 2008.

Collectively, these studies highlighted the feasibility of OCT viability imaging; however, they did not extensively validate how different mechanisms of cell death impacted their metrics. Many studies conducted their experiments on a limited number of biological samples and drug treatments. This restricted their scope to a few mechanisms of cell death which challenges the reproducibility and clinical relevance of their findings. In addition, despite the 3D capabilities of OCT imaging, many studies did not include region-specific analysis of their outputs. This undermines the advantage of using a 3D imaging modality in a 3D culture platform. Finally, none of the previous studies (to our knowledge) applied OCT viability imaging to a clinically relevant HTS-FPM study. To overcome these challenges, this study aims to more comprehensively correlate OCT metrics with commonly used cell viability assays; it also sets forth an analytical framework for the processing and implementation of OCT-based FPM approaches.

1.3 Specific Aims

Advancements in cancer therapy are constantly pursued to improve patient outcomes and quality of life. FPM aims to achieve this goal by screening various therapies in patient-derived samples to predict the patient's clinical drug response. This approach has the potential to outperform genetic and molecular screens; however, FPM has not been clinically implemented due to two major challenges: loss of clinical translatability of *in vitro* testing and scarcity of biopsied tissue which restricts the effective screening of therapies. The first limitation can be addressed using 3D *in vitro* platforms that reliably capture *in vivo* characteristics of tumors. To address the second challenge, this study investigated the use of OCT viability imaging to overcome the technological limitations

imposed by current cell viability assays. To achieve this goal, we aimed to develop and validate OCT-based viability imaging metrics that are sensitive and specific to multiple cellular perturbations and applicable to multiple tissue types.

Aim 1: Optimizing Microtissue Dose-Response Curves

The objective of the first aim involved optimizing the dose ranges of all treatments for the three types of microtissues used in the study. The mechanism of action for each treatment was matched with an assay that best captured its specified injury (i.e., treatments that target metabolism were optimized using an ATP assay). The concentrations of treatments that elicited 25, 50, and 75 percent cell death after 24 hours of exposure were derived using the dose-response curves from the matched assays. These concentrations were referred to as lethal concentrations (LCs) and used for later aims of the study.

Aim 2: Implementing Multivariate Analysis of Cell Viability Data

The objective of the second aim was to develop a multivariate approach to analyze multi-metric data. Cell viability data from all treatment conditions was collected using the previously determined LC values to generate the multi-metric data. This resulted in data collection from three microtissue types, seven treatments, and four assays. The multivariate approaches involved Linear Mixed Effects (LME) models and Principal Component Analysis (PCA). The second aim had a dual impact. First, it served as a standalone approach to analyzing multi-assay data in a comprehensive and holistic manner through LME regression slopes, PCA loadings, and a new lethal concentration metric termed multi-mechanisms LC_{50} ($MMLC_{50}$). Second, this aim sought to investigate analytical methods

that can be applied to multi-metric OCT outputs. The multi-assay data collected from this aim was also used to develop a prediction model of cell viability in the third aim.

Aim 3: Characterizing OCT Viability Metrics

The goal of the third aim was to characterize the OCT viability metrics. Microtissues were treated using the predetermined LC values from the first aim and imaged using OCT after 24 hours. OCT metrics were then extracted and correlated with the assay data collected from the second aim. Multivariate approaches were used to develop a prediction model that relates OCT metrics with the selected assays' responses. Ultimately a framework was proposed for the prediction of cell viability using OCT metrics.

1.4 References

1. Hatton, I. A. *et al.* The human cell count and size distribution. *Proc. Natl. Acad. Sci. U.S. A.* **120**, e2303077120.

2. Patel, A. Benign vs Malignant Tumors. *JAMA Oncol.* **6**, 1488 (2020).

3. Siegel, R. L., Giaquinto, A. N. & Jemal, A. Cancer statistics, 2024. *CA. Cancer J. Clin.* **74**, 12–49 (2024).

4. Falzone, L., Salomone, S. & Libra, M. Evolution of Cancer Pharmacological Treatments at the Turn of the Third Millennium. *Front. Pharmacol.* **9**, 1300 (2018).

5. Andrés, C. M. C., Pérez de la Lastra, J. M., Munguira, E. B., Andrés Juan, C. & Pérez Lebeña, E. Dual-Action Therapeutics: DNA Alkylation and Antimicrobial Peptidesfor Cancer Therapy. *Cancers* **16**, 3123 (2024).

6. Dasari, S. & Tchounwou, P. B. Cisplatin in cancer therapy: molecular mechanisms of action. *Eur. J. Pharmacol.* **740**, 364–378 (2014).

7. Amjad, M. T., Chidharla, A. & Kasi, A. Cancer Chemotherapy. in *StatPearls* (StatPearls Publishing, Treasure Island (FL), 2025).

8. Sampath, D., Rao, V. A. & Plunkett, W. Mechanisms of apoptosis induction by nucleoside analogs. *Oncogene* **22**, 9063–9074 (2003).

9. Schiff, P. B., Fant, J. & Horwitz, S. B. Promotion of microtubule assembly in vitro by taxol. *Nature* **277**, 665–667 (1979).

10. Maldonado, E. B., Parsons, S., Chen, E. Y., Haslam, A. & Prasad, V. Estimation of US patients with cancer who may respond to cytotoxic chemotherapy. *Future Sci. OA* **6**, FSO600.

11. Dagogo-Jack, I. & Shaw, A. T. Tumour heterogeneity and resistance to cancer therapies. *Nat. Rev. Clin. Oncol.* **15**, 81–94 (2018).

12. Collins, F. S. & Varmus, H. A new initiative on precision medicine. *N. Engl. J. Med.* **372**, 793–795 (2015).

13. Zhao, E. Y., Jones, M. & Jones, S. J. M. Whole-Genome Sequencing in Cancer. *Cold Spring Harb. Perspect. Med.* **9**, a034579 (2019).

14. Mandapati, A. & Lukong, K. E. Triple negative breast cancer: approved treatment options and their mechanisms of action. *J. Cancer Res. Clin. Oncol.* **149**, 3701–3719 (2023).

15. Early Breast Cancer Trialists' Collaborative group (EBCTCG). Trastuzumab for early-stage, HER2-positive breast cancer: a meta-analysis of 13 864 women in seven randomised trials. *Lancet Oncol.* **22**, 1139–1150 (2021).

16. Eikesdal, H. P. *et al.* Olaparib monotherapy as primary treatment in unselected triple negative breast cancer. *Ann. Oncol.* **32**, 240–249 (2021).

17. Couch, F. J., Nathanson, K. L. & Offit, K. Two Decades After BRCA: Setting Paradigms in Personalized Cancer Care and Prevention. *Science* **343**, 1466–1470 (2014).

18. Lu, C. *et al.* Patterns and functional implications of rare germline variants across 12 cancer types. *Nat. Commun.* **6**, 10086 (2015).

19. Dienstmann, R., Jang, I. S., Bot, B., Friend, S. & Guinney, J. Prospective: Database of genomic biomarkers for cancer drugs and clinical targetability in solid tumors. *Cancer Discov.* **5**, 118–123 (2015).

20. Rubio-Perez, C. *et al.* In Silico Prescription of Anticancer Drugs to Cohorts of 28 Tumor Types Reveals Targeting Opportunities. *Cancer Cell* **27**, 382–396 (2015).

21. Gerlinger, M. *et al.* Intratumor Heterogeneity and Branched Evolution Revealed by Multiregion Sequencing. *N. Engl. J. Med.* **366**, 883–892 (2012).

22. Greaves, M. & Maley, C. C. Clonal evolution in cancer. *Nature* **481**, 306–313 (2012).

23. Hiley, C. T. & Swanton, C. Spatial and temporal cancer evolution: causes and consequences of tumour diversity. *Clin. Med.* **14**, s33–s37 (2014).

24. Wensink, G. E. *et al.* Patient-derived organoids as a predictive biomarker for treatment response in cancer patients. *Npj Precis. Oncol.* **5**, 1–13 (2021).

25. Jensen, C. & Teng, Y. Is It Time to Start Transitioning From 2D to 3D Cell Culture? *Front. Mol. Biosci.* **7**, 33 (2020).

26. Kapałczyńska, M. *et al.* 2D and 3D cell cultures - a comparison of different types of cancer cell cultures. *Arch. Med. Sci. AMS* **14**, 910–919 (2018).

27. Xu, F. X., Sun, R., Owens, R., Hu, K. & Fu, D. Assessing Drug Uptake and Response Differences in 2D and 3D Cellular Environments Using Stimulated Raman Scattering Microscopy. *Anal. Chem.* **96**, 14480–14489 (2024).

28. Abbas, Z. N., Al-Saffar, A. Z., Jasim, S. M. & Sulaiman, G. M. Comparative analysis between 2D and 3D colorectal cancer culture models for insights into cellular morphological and transcriptomic variations. *Sci. Rep.* **13**, 1–16 (2023).

29. Alwahsh, M. *et al.* Cytotoxic and molecular differences of anticancer agents on 2D and 3D cell culture. *Mol. Biol. Rep.* **51**, 721 (2024).

30. Fu, X., Guadagni, F. & Hoffman, R. M. A metastatic nude-mouse model of human pancreatic cancer constructed orthotopically with histologically intact patient specimens. *Proc. Natl. Acad. Sci.* **89**, 5645–5649 (1992).

31. Gao, H. *et al.* High-throughput screening using patient-derived tumor xenografts to predict clinical trial drug response. *Nat. Med.* **21**, 1318–1325 (2015).

32. Tentler, J. J. *et al.* Patient-derived tumour xenografts as models for oncology drug development. *Nat. Rev. Clin. Oncol.* **9**, 338–350 (2012).

33. Rosfjord, E., Lucas, J., Li, G. & Gerber, H.-P. Advances in patient-derived tumor xenografts: From target identification to predicting clinical response rates in oncology. *Biochem. Pharmacol.* **91**, 135–143 (2014).

34. Julien, S. *et al.* Characterization of a Large Panel of Patient-Derived Tumor Xenografts Representing the Clinical Heterogeneity of Human Colorectal Cancer. *Clin. Cancer Res.* **18**, 5314–5328 (2012).

35. Marangoni, E. *et al.* A New Model of Patient Tumor-Derived Breast Cancer Xenografts for Preclinical Assays. *Clin. Cancer Res.* **13**, 3989–3998 (2007).

36. Lam, H.-M., Nguyen, H. M. & Corey, E. Generation of Prostate Cancer Patient-Derived Xenografts to Investigate Mechanisms of Novel Treatments and Treatment Resistance. *Methods Mol. Biol. Clifton NJ* **1786**, 1–27 (2018).

37. Halfter, K. *et al.* Prospective cohort study using the breast cancer spheroid model as a predictor for response to neoadjuvant therapy--the SpheroNEO study. *BMC Cancer* **15**, 519 (2015).

38. Mulholland, T. *et al.* Drug screening of biopsy-derived spheroids using a self-generated microfluidic concentration gradient. *Sci. Rep.* **8**, 14672 (2018).

39. Gerlich, D. & Ellenberg, J. 4D imaging to assay complex dynamics in live specimens. *Nat. Cell Biol.* **Suppl**, S14-19 (2003).

40. Riss, T. L. *et al.* Cell Viability Assays. in *Assay Guidance Manual* (eds. Markossian, S. et al.) (Eli Lilly & Company and the National Center for Advancing Translational Sciences, Bethesda (MD), 2004).

41. Pasquier, J. *et al.* P-Glycoprotein-Activity Measurements in Multidrug Resistant Cell Lines: Single-Cell versus Single-Well Population Fluorescence Methods. *BioMed Res. Int.* **2013**, 676845 (2013).

42. Chaudhary, P. M. & Roninson, I. B. Expression and activity of P-glycoprotein, a multidrug efflux pump, in human hematopoietic stem cells. *Cell* **66**, 85–94 (1991).

43. Baker, B. M. & Chen, C. S. Deconstructing the third dimension – how 3D culture microenvironments alter cellular cues. *J. Cell Sci.* **125**, 3015–3024 (2012).

44. Antoni, D., Burckel, H., Josset, E. & Noel, G. Three-Dimensional Cell Culture: A Breakthrough in Vivo. *Int. J. Mol. Sci.* **16**, 5517–5527 (2015).

45. Dingle, Y.-T. L. *et al.* Three-Dimensional Neural Spheroid Culture: An In Vitro Model for Cortical Studies. *Tissue Eng. Part C Methods* **21**, 1274–1283 (2015).

46. Wang, E., Xiang, K., Zhang, Y. & Wang, X.-F. Patient-derived organoids (PDOs) and PDO-derived xenografts (PDOXs): New opportunities in establishing faithful pre-clinical cancer models. *J. Natl. Cancer Cent.* **2**, 263–276 (2022).

47. Demyan, L. *et al.* Pancreatic Cancer Patient-Derived Organoids Can Predict Response to Neoadjuvant Chemotherapy. *Ann. Surg.* **276**, 450–462 (2022).

48. Ooft, S. N. *et al.* Patient-derived organoids can predict response to chemotherapy in metastatic colorectal cancer patients. *Sci. Transl. Med.* **11**, eaay2574 (2019).

49. Larsen, B. M. *et al.* A pan-cancer organoid platform for precision medicine. *Cell Rep.* **36**, 109429 (2021).

50. Vlachogiannis, G. *et al.* Patient-derived organoids model treatment response of metastatic gastrointestinal cancers. *Science* **359**, 920–926 (2018).

51. Riss, T. & Trask, O. J. Factors to consider when interrogating 3D culture models with plate readers or automated microscopes. *In Vitro Cell. Dev. Biol. Anim.* **57**, 238–256 (2021).

52. Thurber, G. M. & Wittrup, K. D. Quantitative spatiotemporal analysis of antibody fragment diffusion and endocytic consumption in tumor spheroids. *Cancer Res.* **68**, 3334–3341 (2008).

53. Pandkar, M. R., Dhamdhere, S. G. & Shukla, S. Oxygen gradient and tumor heterogeneity: The chronicle of a toxic relationship. *Biochim. Biophys. Acta Rev. Cancer* **1876**, 188553 (2021).

54. Mueller-Klieser, W. Tumor biology and experimental therapeutics. *Crit. Rev. Oncol. Hematol.* **36**, 123–139 (2000).

55. Smith, E. A. & Hodges, H. C. The spatial and genomic hierarchy of tumor ecosystems revealed by single-cell technologies. *Trends Cancer* **5**, 411–425 (2019).

56. Vaziri-Gohar, A. *et al.* Limited nutrient availability in the tumor microenvironment renders pancreatic tumors sensitive to allosteric IDH1 inhibitors. *Nat. Cancer* **3**, 852–865 (2022).

57. Mourant, J. R. *et al.* Mechanisms of light scattering from biological cells relevant to noninvasive optical-tissue diagnostics. *Appl. Opt.* **37**, 3586–3593 (1998).

58. Mourant, J. R. *et al.* Light scattering from cells: the contribution of the nucleus and the effects of proliferative status. *J. Biomed. Opt.* **5**, 131–137 (2000).

59. Wu, T. T., Qu, J. Y. & Xu, M. Unified Mie and fractal scattering by biological cells and subcellular structures. *Opt. Lett.* **32**, 2324–2326 (2007).

60. Drezek, R., Dunn, A. & Richards-Kortum, R. Light scattering from cells: finite-difference time-domain simulations and goniometric measurements. *Appl. Opt.* **38**, 3651–3661 (1999).

61. Beauvoit, B. & Chance, B. Time-resolved spectroscopy of mitochondria, cells and tissues under normal and pathological conditions. *Mol. Cell. Biochem.* **184**, 445–455 (1998).

62. Krysko, D. V., Vanden Berghe, T., D'Herde, K. & Vandenabeele, P. Apoptosis and necrosis: Detection, discrimination and phagocytosis. *Methods* **44**, 205–221 (2008).

63. Pasternack, R. M., Zheng, J.-Y. & Boustany, N. N. Optical scatter changes at the onset of apoptosis are spatially associated with mitochondria. *J. Biomed. Opt.* **15**, 040504 (2010).

64. Majno, G. & Joris, I. Apoptosis, oncosis, and necrosis. An overview of cell death. *Am. J. Pathol.* **146**, 3–15 (1995).

65. Fink, S. L. & Cookson, B. T. Apoptosis, Pyroptosis, and Necrosis: Mechanistic Description of Dead and Dying Eukaryotic Cells. *Infect. Immun.* **73**, 1907–1916 (2005).

66. Holmes, C., Tabrizian, M. & Bagnaninchi, P. O. Motility imaging via optical coherence phase microscopy enables label-free monitoring of tissue growth and viability in 3D tissue-engineering scaffolds. *J. Tissue Eng. Regen. Med.* **9**, 641–645 (2015).

67. Martucci, N. J. *et al.* Nondestructive Optical Toxicity Assays of 3D Liver Spheroids with Optical Coherence Tomography. *Adv. Biosyst.* **2**, 1700212 (2018).

68. Farhat, G., Yang, V. X. D., Czarnota, G. J. & Kolios, M. C. Detecting cell death with optical coherence tomography and envelope statistics. *J. Biomed. Opt.* **16**, 026017 (2011).

69. Vermeer, K. A., Mo, J., Weda, J. J. A., Lemij, H. G. & Boer, J. F. de. Depth-resolved model-based reconstruction of attenuation coefficients in optical coherence tomography. *Biomed. Opt. Express* **5**, 322–337 (2014).

70. Stefan, S. *et al.* Determination of confocal profile and curved focal plane for OCT mapping of the attenuation coefficient. *Biomed. Opt. Express* **9**, 5084–5099 (2018).

71. Li, K., Liang, W., Yang, Z., Liang, Y. & Wan, S. Robust, accurate depth-resolved attenuation characterization in optical coherence tomography. *Biomed. Opt. Express* **11**, 672–687 (2020).

72. Liu, J. *et al.* Optimized depth-resolved estimation to measure optical attenuation coefficients from optical coherence tomography and its application in cerebral damage determination. *J. Biomed. Opt.* **24**, 1–11 (2019).

73. van der Meer, F. J. *et al.* Apoptosis- and necrosis-induced changes in light attenuation measured by optical coherence tomography. *Lasers Med. Sci.* **25**, 259–267 (2010).

74. Jung, Y., Klein, O. J., Wang, H. & Evans, C. L. Longitudinal, label-free, quantitative tracking of cell death and viability in a 3D tumor model with OCT. *Sci. Rep.* **6**, 27017 (2016).

75. Huang, Y. *et al.* Optical Coherence Tomography Detects Necrotic Regions and Volumetrically Quantifies Multicellular Tumor Spheroids. *Cancer Res.* **77**, 6011–6020 (2017).

76. Apelian, C., Harms, F., Thouvenin, O. & Boccara, A. C. Dynamic full field optical coherence tomography: subcellular metabolic contrast revealed in tissues by interferometric signals temporal analysis. *Biomed. Opt. Express* **7**, 1511–1524 (2016).

77. Jeong, K., Turek, J. J. & Nolte, D. D. Volumetric motility-contrast imaging of tissue response to cytoskeletal anti-cancer drugs. *Opt. Express* **15**, 14057–14064 (2007).

78. Arezza, N. J. J., Razani, M. & Kolios, M. C. Dynamic light scattering optical coherence tomography to probe motion of subcellular scatterers. *J. Biomed. Opt.* **24**, 1–7 (2019).

79. El-Sadek, I. A. *et al.* Three-dimensional dynamics optical coherence tomography for tumor spheroid evaluation. *Biomed. Opt. Express* **12**, 6844–6863 (2021).

80. Dunkers, J. P., Lee, Y. J. & Chatterjee, K. Single cell viability measurements in 3D scaffolds using in situ label free imaging by optical coherence microscopy. *Biomaterials* **33**, 2119–2126 (2012).

81. Bagnaninchi, P. O., Holmes, C., Drummond, N., Daoud, J. & Tabrizian, M. Two-dimensional and three-dimensional viability measurements of adult stem cells with optical coherence phase microscopy. *J. Biomed. Opt.* **16**, 086003 (2011).

CHAPTER 2: OPTIMIZING MICROTISSUE DOSE-RESPONSE CURVES

Zein-Sabatto, A., St. Angelo, K., Madnick S.J., Hoffman-Kim, D., Morgan J.R., & Lee, J. Multi-assay assessment of cytotoxicity reveals multiple mechanisms of action in 3D microtissues. *Sci. Rep.* **15**, 3090 (2025).

2.1 Introduction

Cell viability assays are an integral component of the *in vitro* testing landscape. Viability data has become ubiquitous in research, especially in studies that evaluate the effects of different perturbations, treatments, and diseases on cell health. Many assays exist that cover a wide range of biological processes involved in viability. In general, assays measure changes to specific biomarkers that are correlated with viability. Assays may utilize the fluorescent tagging of cellular components or rely on enzyme-substrate interactions to indicate the presence or lack of viable cells.[1] The data from assays is often collected using microscopy or plate readers to measure colorimetric changes, fluorescence, luminescence, or changes in cellular morphology.[1] Traditionally, these assays were developed for 2D cultures grown in well plates; however, many manufacturers include protocols for 3D platforms or provide 3D-compatible versions for many products. It is essential that assays are optimized for each *in vitro* platform since cell density and tissue

dimensions are important factors that influence assay readouts. Cells grown on 2D surfaces produce consistent and reproducible cell counts across passages; however, 3D cultures incorporate more batch heterogeneity. Inadequately optimized 3D cultures may not reach the minimum detection limit or saturate the assay output depending on cell count. Furthermore, cells are homogenously exposed to assay reagents when grown in 2D monolayers; however, 3D cell cultures inherently produce diffusion gradients across their depth. This necessitates the optimization of incubation times and wash cycles to ensure consistent exposure/removal of reagents throughout the culture's depth. Finally, some 3D platforms are embedded in or grown on hydrogels which can dilute, retain, or block reagents thereby impacting assay outputs. These challenges, coupled with a lack of standardized protocols, highlight the need for careful experimental planning and optimization prior to data collection.

One approach to analyzing cell viability data involves plotting dose-response curves. This analysis determines the relationship between treatment dose and biological impact.[2] In addition to treatment concentration, the dose is dependent on exposure time, delivery, frequency, and other properties like cell permeability of the compound.[2] Most biological dose-responses can be modeled using sigmoidal curves. Low doses have a negligible effect on response output until a certain threshold is reached.[3] Once the threshold dose is surpassed, the response effect begins to increase then plateaus at higher doses. Increasing the dose beyond the asymptotic concentration yields little change in response output which is characteristic of the ceiling effect.[3] For the purposes of this study, the response variable was measured as a change in viability and therefore reported as a lethal concentration. This approach allows for the comparison of toxicities across compounds,

particularly by comparing the LC_{50}. Compounds with smaller LC_{50} are considered more potent since they are able to induce 50% cell death at a lower dose.[3] We were particularly interested in measuring lethal concentrations that elicited 25, 50, and 75 percent cell death which were extrapolated from the sigmoidal curves using Nonlinear Mixed Effects (NLME) models. Developing the dose-response curves served as the first step in the study to elicit cytotoxicity in a reproducible manner while simultaneously determining the sensitivity range of the assays. In order to capture a broad range of cellular responses, we created 3D microtissues from multiple tissue types including hepatocellular carcinoma (HepG2), breast adenocarcinoma (MCF7), and primary neonatal cortical rat tissue which were also referred to as neurospheroids. We then utilized seven compounds to elicit cell death: 2-Deoxy-D-glucose (2DG), oligomycin A, Triton X-100, melittin, cisplatin, melphalan, and paclitaxel. The mechanism of action of these drugs includes metabolic inhibition, membrane poration, DNA damage, and cytoskeletal disruption. Multi-fold serial dilutions for all treatments ensured that the linear range of the dose-response curves were captured.

2.2 Methods

2.2.1 Cell Culture

Human Hepatocellular Carcinoma Culture

Human hepatocellular carcinoma cells (HB-8065, HepG2) were obtained from the American Type Culture Collection (ATCC). Cells were expanded in T-75 flasks containing Eagle's Minimum Essential Media (EMEM, 50-238-2632, ATCC) supplemented with 10%

fetal bovine serum (FBS, 50-753-2981, GeminiBio) and 1% penicillin-streptomycin (15140122, Gibco). Cells were fed every other day and passaged weekly after reaching ~75-80% confluency. Passage counts were kept under 10 to prevent culture drift. Once ready for passage, the cell monolayer was washed twice with 2 mL of 0.25% trypsin-EDTA (25-200-056, Gibco). After the second wash, 3 mL of trypsin was added and allowed to incubate with the cells at 37°C and 5% CO_2 for seven minutes. Cellular detachment was confirmed visually, and 12 mL of warmed media was added to neutralize the trypsin and suspend the cells. The bottom of the flask was rinsed twice to maximize the retrieval of cells. The 15 mL cell suspension was transferred to a 50 mL conical tube and centrifuged at 125 G for six minutes. This process effectively aggregated the cells into a pellet and allowed for the removal of the supernatant. The pellet was then vigorously disaggregated by firmly grasping one end of the tube with one hand and striking the other end with the other hand. After visually confirming the disassociation of the pellet, a 5 mL serological pipette was used to add 4 mL of warmed media along the edges of the tube. The cell suspension was further mixed by repetitively pipetting six times with the tip firmly pressed against the bottom of the tube and six times with the tip against the tube wall. Cells were counted using a hemacytometer using a 1:10 solution of Trypan Blue (15-250-061, Gibco) to cell suspension. The appropriate volume of cell suspension that contained 1.25 million cells was added to a T-75 flask containing 15 mL of warmed media using a 1 mL stripette. The flask was then gently rocked 20 times in the upright position and then placed flat and swirled four times using a “figure eight” pattern to ensure an even distribution of cells within the flask. The flask was then placed in the incubator set to 37°C and 5% CO_2.

Human Mammary Gland Adenocarcinoma Culture

Human mammary gland adenocarcinoma cells (HTB-22, MCF7) were also obtained from the ATCC. Cells were cultured in T-75 flasks using EMEM supplemented with 10% FBS, 1% penicillin-streptomycin, and 0.01 mg/mL human recombinant insulin (I9278, Sigma-Aldrich). Passage and culture protocols were similar to those followed for HepG2 culture with a few exceptions. Once ready for passage, the MCF7 monolayer was washed twice with 2 mL of 0.25% trypsin and incubated with 2 mL of trypsin for seven minutes in the incubator at 37°C and 5% CO_2. Following the detachment of the cell layer, 13 mL of complete media was added to the flask and the bottom of the flask was rinsed twice. The cell suspension was transferred to a 50 mL conical tube and centrifuged at 125 G for 6 minutes. The supernatant was removed, and the pellet was disaggregated by firmly striking the tube as previously mentioned. Once the pellet was disaggregated, 4 mL of complete media was added, and the cell suspension was mixed six times with the pipette firmly pressed against the bottom of the tube and six times with the pipette tip against the tube wall. Cell counts were calculated using a hemacytometer using a 1:10 dilution of Trypan Blue to cell suspension. Flasks were seeded at 6 million cells in 15 mL of warmed media. To ensure uniform seeding, the flask was gently rocked upright for 20 cycles and then placed flat and gently swirled in a “figure eight” pattern for four cycles. Once complete, the flask was placed in the incubator set to 37°C and 5% CO_2.

Primary Neonatal Rat Cortical Cell Isolation

Untimed pregnant CD rats (embryonic day 15-17) were purchased from Charles River. Rat pups were collected between days 0-2 for cortical dissection. All animal

procedures were performed using protocols approved by the Institutional Animal Care and Use Committee (IACUC) at Brown University. Neonatal rats were euthanized following the American Veterinary Medical Association (AVMA) Guidelines for the Euthanasia of Animals (2020). All methods were reported in compliance with the ARRIVE guidelines. Neonatal pups were anesthetized using hypothermia. Pups were first wrapped in gauze and then plastic wrap to protect them from getting wet. The wrapped pups were placed in an ice bucket and completely covered with ice for 45 minutes. The effect of anesthesia was confirmed via a paw pinch, and the pups were euthanized via decapitation using a pair of sharp scissors. The skin was cut along the midline starting with a proximal incision starting from the neck and distally cutting toward the snout using a pair of fine point dissection scissors. The loosened skin was peeled back to expose the cranium which was cut in a similar fashion starting with a proximal incision and carefully proceeding distally without puncturing the brain. A spatula was then used to dislodge the brain and place it inside a 35 mm dish containing 4 mL of chilled buffer solution which consisted of Hibernate A (HA, TransnetYX), 1X B-27 Plus Supplement (A3582801, Gibco), and 0.5 mM GlutaMax (35050061, Gibco). A pair of bent forceps was used to stabilize the brain by holding the cerebellum in place while another pair of bent forceps was used to cut around the perimeter of the cortex. The cortex was then peeled laterally, excised, and placed into another 35 mm petri dish with 3 mL of chilled Hibernate A buffer solution. All cortices were removed in this manner. Next, bent forceps were used to remove the meninges from the surface of the cortices. Exposed cortices were manually cut into smaller pieces using the forceps and placed into a 15 mL conical tube containing 3 mL of digestion enzyme solution which consisted of 6 mg Papain (PAP, TransnetYX) dissolved in 3 mL of Hibernate A without

calcium chloride (HACA, TransnetYX). A total of four cortical hemispheres were placed in each vial which were digested for 30 minutes at 30°C while gently agitating the solution every 5 minutes. After digestion, the papain solution was removed without disrupting the cortical tissue, and a total of 2 mL of chilled Hibernate A buffer solution (with calcium chloride, B-27 Plus Supplement, and GlutaMax) was added to the tube. The cortical tissue was triturated with a fire-polished glass pipette until a homogenous cell suspension was made. The cell suspension was strained using a sterile 40 µm nylon strainer followed by a 2 mL rinse using chilled Hibernate A buffer solution. The collected suspension was centrifuged at 150 G for 5-7 minutes, and the supernatant was removed. The cell pellet was resuspended in 5 mL of warmed media which consisted of Neurobasal Plus medium (A3582901, Gibco), 1X B-27 Plus Supplement, 0.5 mM GlutaMax, and 1% penicillin-streptomycin. The cell suspension was filtered for a second time and rinsed with 2 mL of warmed media. This suspension was centrifuged at 150 G for 5-7 minutes and the supernatant removed. Another 5 mL of warmed media was used to resuspend the pellet, and the straining process was repeated for a third time. After the third centrifugation, the pellet was resuspended using 10 mL of warmed media. The final cell count was conducted using a hemacytometer with a 1:1 Trypan Blue to cell suspension solution. The appropriate number of cells needed to achieve the target seeding density was determined, and the volume of cell suspension needed to achieve this density was removed, centrifuged, and resuspended accordingly.

2.2.2 Three-Dimensional Microtissue Culture

Three-Dimensional spheroids were formed using the 24-96 small spheroid 3D Petri Dish from MicroTissues Inc. Agarose gels were made by dissolving 2 g of autoclave-sterilized UltraPure Agarose (16500500, Invitrogen) in 100 mL of phosphate buffered saline (PBS, 20012027, Gibco). The agarose-PBS solution was heated using a conventional microwave for 2 minutes while shaking the solution every 30 seconds until a homogenous liquid formed. Once molten, the liquid agarose was pipetted into the autoclave-sterilized MicroTissues micro-mold and allowed to cool into a gel. These gels contained 96 microwells with a diameter of 400 μm and depth of 800 μm. Gels were removed from the mold, inspected for defects, then placed in a 24-well plate. Depending on the tissue culture type, 1 mL of base media (i.e., EMEM or Neurobasal Plus medium with 1% penicillin-streptomycin alone) was added to each well. Gels were allowed to equilibrate with base media for a minimum of three days with media changes every 24 hours.

The base media was exchanged with fully supplemented media 2-3 hours prior to seeding. HepG2, MCF7, and cortical microtissues were seeded at 144,000, 24,000, and 384,000 cells per gel, respectively. Gels were seeded by aspirating all media within the well and reservoir directly above the microwells. Next, 70 μL of the recalculated cell suspension was added to each gel in a drop-wise fashion. Cells were allowed to settle into the microwells for at least 30 minutes in the incubator prior to the addition of 1 mL of the appropriate media to each well. The well plate was then placed back into the incubator set to 37°C and 5% CO_2. Media was replaced every 2-3 days.

2.2.3 Compound Treatment

A total of seven compounds with relatively well-known mechanisms of action were selected to induce cell death. 2DG (D8375, Sigma Aldrich) and oligomycin A (75351, Sigma Aldrich) were selected to metabolically challenge microtissues. Triton X-100 (X100, Sigma Aldrich) and melittin (M2272, Sigma Aldrich) were selected to perforate the cellular membrane. Cisplatin (P4394, Sigma Aldrich) and melphalan (M2011, Sigma Aldrich) were selected to crosslink and damage DNA. Finally, paclitaxel (T7191, Cell Signaling Technologies) was selected to over-stabilize the microtubules within the microtissues. Stock solutions for each compound were made using the following dilutions: 100 mg 2DG per 1 mL of media, 5 mg oligomycin A in 93.28 µL dimethyl sulfoxide (DMSO, D2650, Sigma Aldrich), 10 µL Triton X-100 into 990 µL media, 5 mg melittin in 1.743 mL of ultrapure water, 25 mg cisplatin in 13.887 mL of 0.9% saline in ultrapure water, 100 mg melphalan in 16.717 mL of 200 proof ethanol with 300 µL of HCl, and 1 mg paclitaxel in 41.82 µL DMSO. Table 1 summarizes how the stock solutions were made and their final concentrations. All compounds were purchased as lyophilized powders except Triton X-100 which came as a viscous liquid. Both Triton X-100 and 2DG were readily soluble in cell media and did not require the use of alternative vehicles. Stock solutions for both 2DG and Triton X-100 were made fresh while the remainder of the stock solutions were aliquoted and stored in appropriate conditions. All reconstituted compounds were made following solubility guidelines and used within two months of their creation. If a target concentration was not obtainable using the recommended solubility guidelines, the treatment was considered beyond the practical limit and excluded from the study.

Table 1. The amount of solute and solvent used to make the final stock solutions for each compound was reported. All compounds were reconstituted from a lyophilized powder except Triton X-100 which originated as a viscous liquid. Only the stock concentration of Triton X-100 was reported as a percentage. Both Triton and 2DG were readily soluble in media and did not require the use of alternative vehicles. DMSO: dimethyl sulfoxide, conc: concentration.

Solute	Solute Quantity	Solvent	Solvent Volume	Stock [conc.]
2DG	300 mg	Media	3000 µL	609.2 mM
Oligomycin A	5 mg	DMSO	93 µL	67.8 mM
Triton X-100	10 µL	Media	990 µL	1.0 %
Melittin	5 mg	Water	1743 µL	1.0 mM
Cisplatin	25 mg	0.9% Saline	13,887 µL	6.0 mM
Melphalan	100 mg	Ethanol	17,017 µL	19.6 mM
Paclitaxel	1 mg	DMSO	42 µL	28.0 mM

Working solutions were made by serial dilutions using the appropriate vehicles, then equal volumes of each working solution were added to warmed media to achieve the desired treatment concentration. Microtissues were treated by aspirating the 1 mL of media present within the well surrounding the gel followed by the addition of 1 mL of treated media. Final drug concentrations were increased by a factor of 1.4 to compensate for the displacement caused by the agarose gel. All microtissues were exposed to treatment for 24 hours.

2.2.4 CellTiter-Glo 3D Assay Protocol

The CellTiter-Glo 3D assay (G9683, Promega) was used to measure ATP content within the microtissues. This was chosen as the "best-fit" assay for microtissues treated with a glycolytic inhibitor, 2DG, and ATP synthase inhibitor, oligomycin A. Assay reagent was aliquoted in 15 mL conical tubes then stored at -20°C to limit the number of freeze-thaw cycles. Prior to the start of the assay, the reagent was removed from the freezer and allowed to steadily reach room temperature. Treated gels containing HepG2 or cortical

microtissues were transferred to 35 mm petri dishes containing 3 mL of warmed media. A P1000 pipette was used to gently flush individual microtissues from their microwells. A P200 pipette, with ~ 2 cm trimmed from the tip, was used to pick up individual microtissues along with 90 µL of media. The contents of the pipette were placed into a single well of a white-walled, clear bottom 96-well plate. Unlike HepG2 and cortical microtissues, MCF7 microtissues were not flushed from their microwells since they formed loosely aggregating spheroids that could not be individually placed into a 96-well plate. Instead, the entire gel was transferred to a well in a white-walled, opaque 24-well plate with 500 µL of media.

After plating the HepG2 and cortical microtissues into the 96-well plate, each spheroid was imaged for its cross-sectional area using a phase-contrast microscope (TC100 Eclipse, Nikon) using a 10X objective. MCF7 microtissues were not imaged for their cross-sectional area. The assay was conducted by adding an equal volume of reagent to media present per well (i.e., 90 µL of reagent for HepG2 and cortical microtissues and 500 µL for MCF7). All plates were mixed for 5 minutes using an orbital shaker at 125 rpm and incubated for an additional 25 minutes at room temperature. The luminescent output from each well was measured using a multimode plate reader (Cytation3, BioTek) using the default gain of 125 and 1 second integration time. Read height was adjusted to a vehicle-treated microtissue for each plate run.

2.2.5 Live/Dead Viability/Cytotoxicity Assay Protocol

The Live/Dead Viability/Cytotoxicity assay for mammalian cells (L3224, Invitrogen) was used to measure cytotoxicity induced by membrane poration. It was chosen for microtissues treated with a detergent, Triton X-100, and pore-forming toxin, melittin.

The Live/Dead assay consisted of adding 0.5 µL of calcein AM and 2 µL of ethidium homodimer per 1 mL of media. Live/Dead was conducted on whole gels by removing the treatment media from every well and replacing it with 1 mL of warmed media containing the Live/Dead reagents. The plate was protected from light and incubated at 37°C and 5% CO_2 for 30 minutes. Gels were imaged using a Zeiss Axiovert 100 inverted fluorescence microscope using a 10X objective. A total of 12 (4x3) tiles were acquired and stitched together using Zeiss's built-in software. Images were taken using brightfield, EGFP, and Alexa Fluor 568 channel presets. All images belonging to the same replicate and tissue culture type were acquired using identical exposure times and excitation intensity. Minor adjustments were allowed for exposure times between experiments to ensure optimal image signal brightness. The effects of these adjustments were addressed by data normalization and model fitting which effectively handle random effects within the dataset.

2.2.6 Caspase-Glo 3/7 3D Assay Protocol

The Caspase-Glo 3/7 3D assay (G8982, Promega) was used to measure apoptotic cell death through the presence of capsase-3 and caspase-7 within the microtissues. This assay was chosen to quantify cell death in microtissues treated with the alkylating agents, cisplatin and melphalan. The reconstituted assay reagents were also aliquoted into 15 mL conical tubes, and they were stored at 4°C. The assay reagent was allowed to reach room temperature prior to its addition to the samples. The protocol used for the caspase assay was very similar to the CellTiter-Glo 3D ATP assay. Treated gels containing HepG2 and cortical microtissues were transferred to a 35 mm petri dish containing 3 mL of warm media. Individual microtissues were flushed out of their microwells using a P1000 pipette.

Using a trimmed P200 pipette, 90 µL of media and a single microtissue were placed into a well in a white-walled, clear bottom 96-well plate. MCF7 microtissues were not removed from their microwells; instead, the entire gel was transferred to a white-walled, opaque 24-well plate alongside 500 µL of media. An equal volume of Caspase-Glo 3/7 3D reagent was added to each well relative to the media already present. Plates were mixed using an orbital shaker set to 125 rpm for 30 seconds at room temperature. Plates were left at room temperature for an additional 30 minutes prior to analysis. Luminescent output was measured with the Cytation3 plate reader using the same acquisition parameters of 125 gain and 1 second integration time. Read height was auto adjusted to a well containing a microtissue from the largest treatment group (i.e., the well with the highest potential for luminescent output).

2.2.7 Click-iT EdU Proliferation Assay Protocol

The Click-iT EdU Alexa Fluor 647 HCS assay (C10357, Invitrogen) was used to quantify the amount of proliferation occurring within the microtissues. This assay was chosen to analyze microtissues treated with the taxane, paclitaxel. After 24 hours of treatment, the media surrounding the gels was removed and replaced with warm media containing 5 µM of the 5-ethynyl-2'-deoxyuridine (EdU) component. The HepG2 and MCF7 cultures were incubated at 37°C and 5% CO_2 for six hours while cortical cultures were incubated for 24 hours. This allowed the EdU molecules sufficient time to incorporate into the newly synthesized DNA. One gel per experimental set was not treated with EdU and served as the "no primary" control. After the incubation period, the media surrounding the gels was replaced with 1 mL of a fixative solution containing 4% paraformaldehyde

and 8% sucrose in PBS. The plates were protected from light and fixed overnight at room temperature. Fixed gels were rinsed thrice with PBS for 30 minutes each and later stored at 4°C until they were stained. Prior to staining, the microtissues inside the gels were permeabilized twice with a 0.2% Triton X-100 solution in PBS for two hours each. The gels were then washed twice with PBS for 15 minutes each to remove the permeabilizing solution. Following the manufacturer's protocols, the Click-iT reagent cocktail was freshly prepared for each experiment and protected from light. Staining was accomplished by replacing the PBS in each well with 1 mL of Click-iT reagent cocktail for one hour. Next, the gels were rinsed with rinse buffer for 15 minutes. In order to visualize all nuclei, the rinse buffer was replaced with a 1X solution of Hoechst in PBS for one hour. Wells were then washed twice with PBS for 15 minutes each to remove the Hoechst solution. Finally, 1 mL of PBS was added to each well and the plate was wrapped in parafilm, protected from light, and stored at 4°C until it was imaged.

Prior to imaging, individual gels were cut using a size 10 scalpel blade to remove the four agarose walls surrounding the microwells. In a 24-well plate, a drop of PBS was added to the center of each well, and a cut gel was inverted over the PBS drop. This process ensured that no air bubbles formed when the gel was inverted to allow for better imaging of the microtissues. The PBS drop should not be large enough to cause the gel to float which would result in poor imaging outcomes. After all gels were inverted, pre-warmed 2% agarose was carefully added over the gels to secure them in place. The agarose was allowed to solidify, then 1 mL of PBS was added to each well to keep the gels hydrated. This entire process was conducted in a dimly lit room to prevent photobleaching of the fluorophore.

The microtissues were imaged using a Zeiss Axiovert 100 inverted fluorescence microscope using a 10X objective. A total of 12 tiles (4x3) were taken and stitched together using Zeiss's ZenPro software. Images were acquired using the brightfield, DAPI, and Cy5 channel presets. Exposure time and excitation intensity were kept consistent across all samples from within the same experiment. Minor adjustments to exposure time were made to ensure optimal image brightness between experiments. The effect of these adjustments was controlled through data normalization as well as random effects modeling.

2.2.8 Image Processing

Cross-Sectional Pixel Area Extraction

MATLAB code was developed to extract the cross-sectional pixel area from HepG2 and cortical microtissues. The phase-contrast images from HepG2 and cortical microtissues were saved in the jpeg format. Individual images were loaded into the code, and a modified built-in function, called *lazysnapping*, was used to extract foreground pixels from the image background. The performance of the extraction was assessed visually and repeated if necessary. Cross-sectional areas from the code were reported as pixel counts. Luminescent output from the ATP and caspase assays were divided by the cross-sectional pixel area to normalize them by spheroid size. This size normalization was not conducted for MCF7 outputs.

Live/Dead Fluorescence Image Processing

MATLAB code was developed to process and extract intensity values from the Live/Dead images. The Zeiss ZenPro software was able to export the multi-tiled, multi-

channel images into a single stitched tiff file. ImageJ software (Fiji) was used to split the brightfield, EGFP (for calcein AM), and Alexa Fluor 568 (for ethidium homodimer) channels into separate tiff files. These tiff files were loaded into a custom-made MATLAB code. Image processing included background noise correction followed by automated segmentation which included circle detection, adaptive thresholding-based binarization, and morphological opening/closing. Approximately 30-40 microtissues could be visualized in the field of view; however, the code segmented 20 microtissues with cross-sectional areas closest to the median for further analysis.

EdU Fluorescence Image Processing

EdU fluorescence images were processed in the same manner as the Live/Dead images. In brief, multi-channel images from the Zeiss microscope were split into single channels including brightfield, DAPI (for Hoechst), and Cy5 (for EdU) using ImageJ. Individual tiff images were loaded into the MATLAB code for image segmentation. Image pre-processing included background noise correction, and the segmentation pipeline involved circle detection, adaptive thresholding, and morphological opening/closing. Approximately 30-40 microtissues were captured per field of view. Only 20 microtissues with cross-sectional areas closest to the median were selected for further analysis.

2.2.9 Statistical Analysis

Dose-response curves from the CellTiter-Glo 3D and Caspase-Glo 3/7 3D assays were generated from eight HepG2 microtissues, eight cortical microtissues, and three intact MCF7 gels for each treatment condition. Live/Dead and EdU assay dose-response curves were generated from 20 microtissue per treatment condition. A total of 3-4 passage

replicates were obtained for all treatment conditions. All assay outputs, except for the caspase assay, were normalized by the average output from the vehicle control group. All assay outputs were plotted against the log-transformed treatment concentration. Nonlinear mixed effects (NLME) models were used to fit the dose-response curves in MATLAB. The equations used to fit the models were reported in section 2.3. The 95% confidence intervals were reported for each model fit, and the LC_{25}, LC_{50}, and LC_{75} were extrapolated from the NLME line fits. All figures and data analysis were generated in MATLAB.

2.3 Results

2.3.1 CellTiter-Glo 3D Assay

The CellTiter-Glo 3D assay was used to measure metabolic disruption in 2DG and oligomycin A treated microtissues. The change in normalized luminescence output was plotted against increasing treatment concentrations for HepG2, MCF7, and cortical microtissues (black lines, Fig. 4a, c). The highest tested doses for 2DG and oligomycin A were 218 mM and 90.3 μM, respectively. Initial testing started with 10-fold dilutions and later adjusted to 4-fold and 3-fold, respectively, for a total of nine conditions including controls. The total percentage of DMSO added to the media for oligomycin A treatment did not exceed 0.5% for HepG2 and MCF7 cultures and 0.1% for cortical cultures (also referred to as neurospheroids). As previously mentioned, 2DG was directly dissolved in media and did not require a vehicle.

The data was fitted to the logistic function from Equation 1 using a NLME model (black lines, Fig. 4)

Equation 1 $$f(x) = f_0 + \frac{1-f_0}{1+e^{k(x-x_0)}}$$

where f is the fractional output, x is the drug concentration in the log scale, f_0 represents the mean output of the blank sample, k represents the steepness of the line, and x_0 is the midpoint concentration of the logistic function in the log scale. Passage-specific random effects were incorporated into the model. The logistic functions were then used to extrapolate the concentrations that elicited 25, 50, and 75 percent cell death (Fig. 4b, d). Both 2DG and oligomycin A treatment could produce the full range of LC values in the microtissues except for oligomycin A in HepG2 cultures which could only induce a LC_{25}.

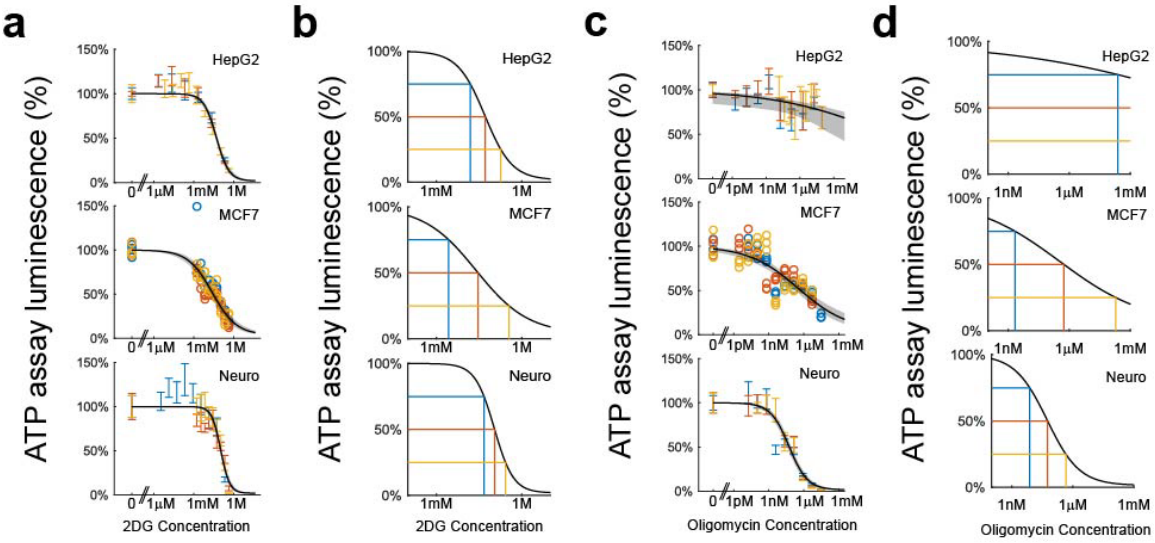

Figure 4. Dose-response curves for 2DG and oligomycin A treated microtissues. (**a**) Logistic-fitted, dose-response curves (black lines) for 2DG treated microtissues were made using a nonlinear mixed effects model (NLME). Each error bar represents the 95% confidence interval from eight individual microtissues for HepG2 and neurospheroids (n = 8 microtissues per condition; three independent experiments in different colors; HepG2 N = 248; neurospheroid N = 240) and three intact gels for MCF7 microtissues (n = 3 gels per condition; three independent experiments in different colors; N = 87). HepG2 and neurospheroid data were normalized by the cross-sectional area of the microtissues, then all data was normalized to its control group. The black lines and shaded gray regions surrounding them represent the NLME fit and its 95% confidence interval. (**b**) Lethal concentrations (LC) of 2DG were estimated from the NLME line fit. Line traces delineate LC_{25} (blue), LC_{50} (red), and LC_{75} (yellow) concentrations. (**c**) Dose-response curves for oligomycin A treated microtissues (HepG2 n = 8, N = 224; MCF7 n = 3, N = 90; neurospheroid n = 8, N = 224; three independent experiments) were generated in the same manner as shown in (**a**). (**d**) LCs of oligomycin A were derived in the same manner as shown in (**b**). Published in Zein-Sabatto A., et al., 2025.

2.3.2 Live/Dead Cytotoxicity Assay

The Live/Dead assay was used to quantify membrane damage in Triton X-100 and melittin treated microtissues (Fig. 5). Viability was measured through the live intensity fraction using Equation 2

$$\text{Equation 2} \qquad Live\ Intensity\ Fraction = \frac{I_{live}}{I_{live}+I_{dead}}$$

where I_{live} is the mean pixel intensity of the calcein AM signal in the EGFR channel and I_{dead} is the mean pixel intensity of the ethidium homodimer signal in the Alexa Fluor 568 channel. In an example dataset, HepG2 microtissues treated with melittin displayed a transition from healthy cells labeled with calcein AM to dead cells labeled with ethidium homodimer as the concentration increased (Fig. 5a). The gradual loss of viability was also captured by the live intensity fraction to produce the dose-response curves for Triton X-100 and melittin (Fig. 5b,d). The highest concentration tested for Triton X-100 and melittin were 0.018% and 25 μM, respectively. Initial testing started with 2-fold dilutions for Triton X-100 and 4-fold dilutions for melittin for a total of nine conditions including controls. The dilutions were later adjusted to 1.7-fold and 2-fold, respectively. The total percentage of water vehicle added to the media for the melittin treatment did not exceed 2%. Triton X-100 was directly dissolved in media and did not require a vehicle.

The data was fitted to Equation 3 using a NLME model (black lines, Fig. 5)

$$\text{Equation 3} \qquad f(x) = \frac{1}{1+e^{k(x-x_0)}}$$

where f is the fractional output of the assay, x is the concentration in log scale, k is the steepness of the slope, and x_0 is the midpoint concentration of the logistic function in the

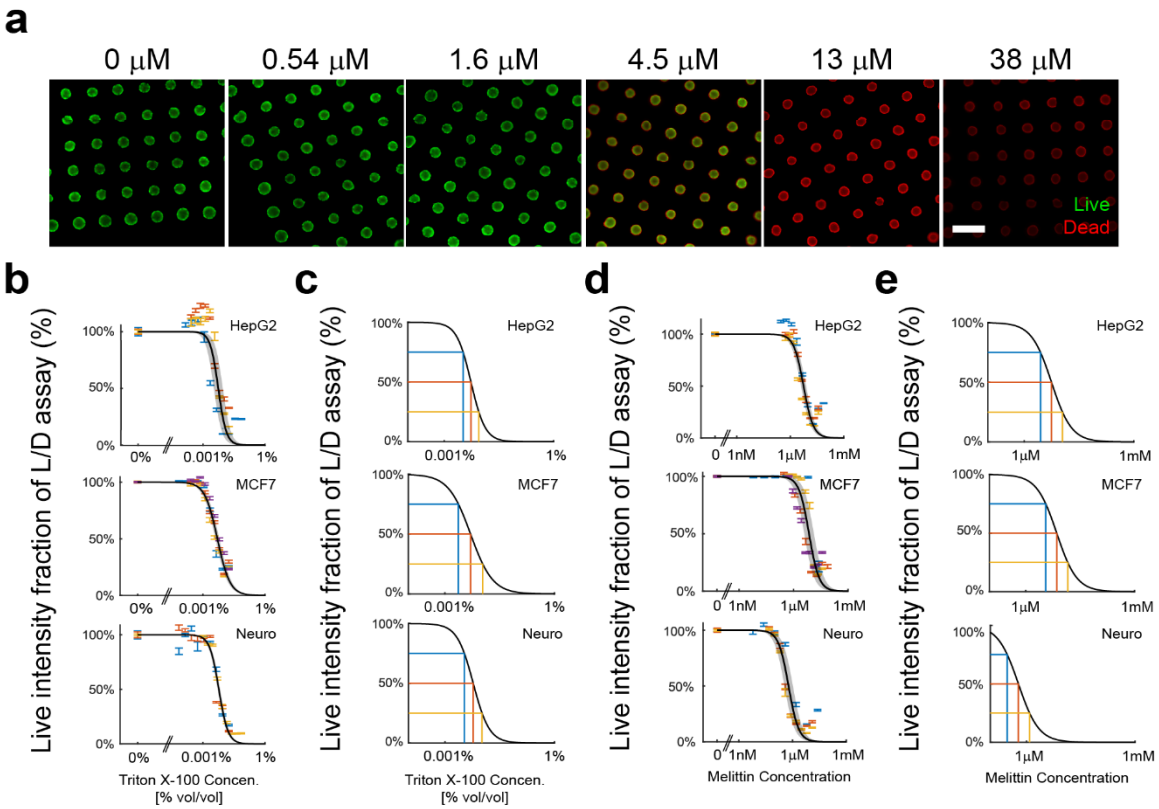

Figure 5. Dose-response curves for Triton X-100 and melittin treated microtissues. (a) Live/Dead images were captured for HepG2 microtissues treated with melittin at increasing concentrations. Multiple microtissues were imaged for every gel. Green: calcein AM (live), red: ethidium homodimer (dead). Scale bar 1 mm. (b) A logistic-fitted, dose-response curve (back lines) for Triton X-100 treated microtissues were made using a nonlinear mixed effects model (NLME). Each error bar represents the 95% confidence interval from 20 individual spheroids for HepG2, MCF7, and cortical microtissues (n = 20 microtissues per condition; 3–4 independent experiments in different colors; HepG2 N = 620; MCF7 N = 800; neurospheroid N = 600). All data was normalized by the control group. The black lines and shaded gray regions surrounding them represent the NLME fit and its 95% confidence interval. (c) Lethal concentrations (LC) of Triton X-100 were estimated from the NLME line fit. Line traces delineate LC_{25} (blue), LC_{50} (red), and LC_{75} (yellow) concentrations. (d) Dose-response curves and NLME fitting for melittin treated microtissues (n = 20 microtissues per condition; 3–4 independent experiments; HepG2 N = 600; MCF7 N = 800; neurospheroid N = 600) were generated in the same manner as shown in (b). (e) LCs for melittin were generated in the same manner as shown in (c). Published in Zein-Sabatto A., et al., 2025.

log scale. Passage-specific random effects were allowed for the midpoint concentration. The logistic functions were then used to extrapolate the concentrations that elicited 25, 50, and 75 percent cell death (Fig. 5c, e). Both Triton X-100 and melittin treatment could produce the full range of LC values in all the microtissues.

2.3.3 Caspase-Glo 3/7 3D Assay

The Caspase-Glo 3/7 3D assay was used to measure apoptotic cell death in microtissues treated with cisplatin and melphalan (Fig. 6). Output luminescence for HepG2 and cortical microtissues were normalized by the cross-sectional pixel area; meanwhile, MCF7 assay outputs were reported as raw values. Unlike the other assays, higher luminescence output from the caspase assay was attributed to lower viability. The highest concentration tested for cisplatin and melphalan were 286 µM and 190 µM, respectively. Initial testing started with 2-fold dilutions for cisplatin and melphalan for a total of 9-10 conditions including controls. The dilution factor was reduced to 1.5-fold for both MCF7

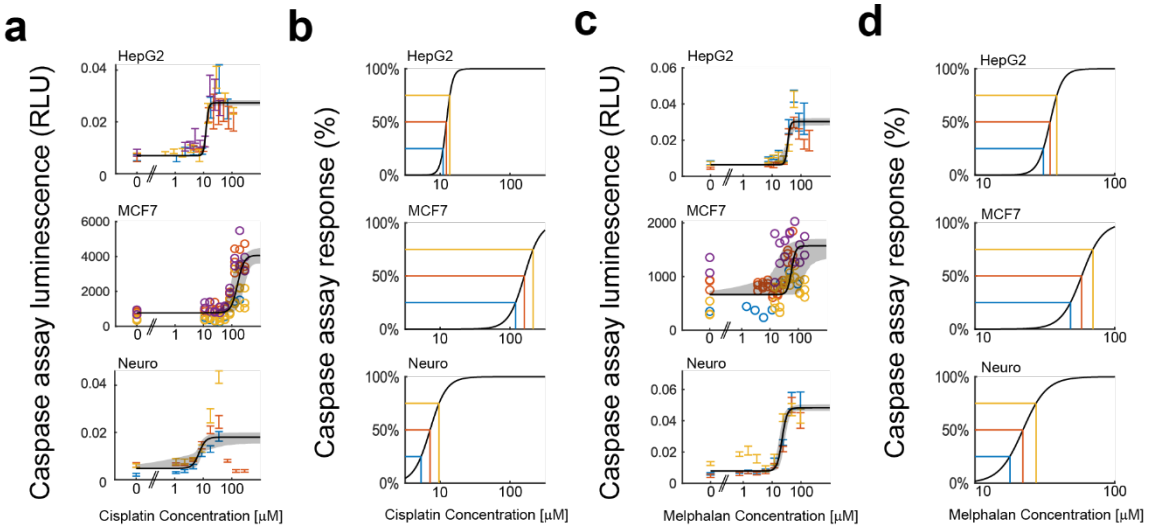

Figure 6. Dose-response curve of cisplatin and melphalan treated microtissues. (a) Logistic-fitted, dose-response curves (black lines) for cisplatin treated microtissues were made using a nonlinear mixed effects model (NLME). Each error bar represents the 95% confidence interval from eight individual microtissues for HepG2 and neurospheroids (n = 8 per condition; 3–4 independent experiments in different colors; HepG2 N = 320; neurospheroid N = 240) and three intact gels for MCF7 microtissues (n = 3 gels per condition; four independent experiments in different colors; N = 90). Only the HepG2 and neurospheroid data were normalized by cross-sectional area of the microtissues. The black lines and shaded gray regions surrounding them represent the NLME fit and its 95% confidence interval. (b) Lethal concentrations (LC) of cisplatin were estimated from the NLME line fit. Line traces delineate LC_{25} (blue), LC_{50} (red), and LC_{75} (yellow) concentrations. (c) Dose-response curves for melphalan treated microtissues (HepG2 n = 8, N = 240; MCF7 n = 3, N = 90; neurospheroid n = 8, N = 240; 3–4 independent experiments) were generated in the same manner as shown in (a). (d) LCs of melphalan were derived in the same manner as shown in (b). Published in Zein-Sabatto A., et al., 2025.

cultures treated with cisplatin and HepG2 cultures treated with melphalan. The remainder of serial dilutions were carried out in 2-fold reductions. The total percentage of saline vehicle added to media for cisplatin treatment did not exceed 5% for MCF7 and 2% for HepG2 and cortical cultures. The percentage of ethanol vehicle added to media for melphalan treatment did not exceed 0.5%. The dose-response curves were fitted to the logistic function in Equation 1 using a NLME model (black lines, Fig. 6). The logistic functions were then used to extrapolate the concentrations that elicited 25, 50, and 75 percent cell death (Fig. 6b, d). Both cisplatin and melphalan treatment could produce the full range of LC values in all the microtissues.

2.3.4 EdU Proliferation Assay

The EdU assay was used to measure proliferation in microtissues treated with paclitaxel (Fig. 7). The synthesis of new DNA, a requirement of proliferating cells, was measured using the intensity of the EdU signal normalized by the intensity of the Hoechst signal. This metric was termed proliferative capacity and calculated using Equation 4

Equation 4 $$Proliferative\ Capacity = \frac{I_{EdU}}{I_{Hoechst}}$$

where I_{EdU} is the mean pixel intensity of the EdU signal in the Cy5 channel and $I_{Hoechst}$ is the mean pixel intensity of the Hoechst signal in the DAPI channel. The effects of paclitaxel treatment on proliferation could be visualized in HepG2 microtissues which displayed a decrease in the number and intensity of EdU positive pixels at the highest concentration (Fig. 7a). The highest concentration tested for paclitaxel was 63 μM with an initial 3-fold dilution across a total of 10 conditions including controls. The dilution factor was later

changed to 2, 5, and 4-fold for HepG2, MCF7, and cortical cultures, respectively. The dose-response data was fitted to Equation 3 using a NLME model (black lines, Fig. 7b, c). The logistic functions were used to extrapolate the concentrations that elicited 25, 50, and 75

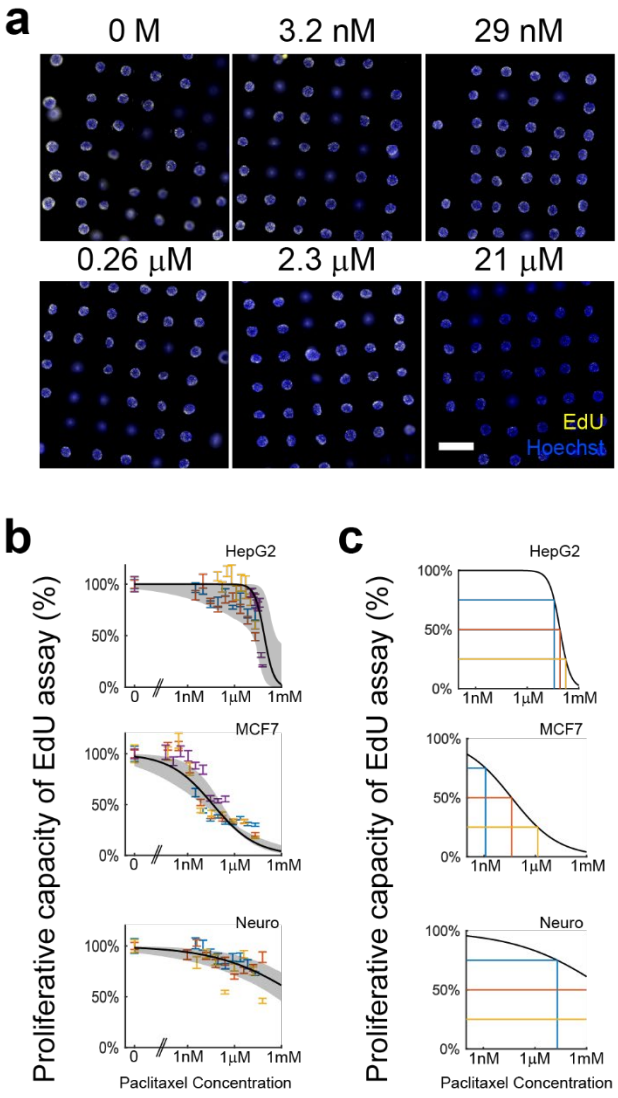

Figure 7. Dose-response curves for paclitaxel treated microtissues. (**a**) HepG2 microtissues were treated with increasing concentrations of paclitaxel. The mean fluorescent intensity of tagged EdU with Cy5 (yellow) and nuclei with Hoechst (blue) were quantified. Scale bar 1 mm. (**b**) Dose-response curves were generated by quantifying the change in EdU expression with respect to Hoechst. The curves were fit using a nonlinear mixed effects (NLME) model using a logistic function (black lines). Each error bar represents the 95% confidence interval from 17–20 individual microtissues (n = 17–20 microtissues per condition; 3–4 independent experiments in different colors; HepG2 n = 19–20, N = 794; MCF7 n = 17–20, N = 796; neurospheroid n = 20, N = 580). All data was normalized by the control group. The black lines and gray shaded regions surrounding them represent the NLME fit and its 95% confidence interval. (**c**) Lethal concentrations (LC) values for paclitaxel were estimated from the NLME line fit. Line traces delineate LC_{25} (blue), LC_{50} (red), and LC_{75} (yellow) concentrations. Published in Zein-Sabatto A., et al., 2025.

percent cell death (Fig. 7c). Paclitaxel treatment produced all LC values for the MCF7 cultures, up to LC_{50} for HepG2 cultures, and up to LC_{25} for cortical microtissues.

2.4 Discussion

Dose-response curves are useful tools that model the effect a molecule has on a biological system. In toxicological studies, dose-response curves can be used to profile the cytotoxicity of a treatment. In this aim, we reliably produced the characteristic "S" shaped logistic curves for most treatment conditions using 8-10 logarithmically spaced concentrations (Fig. 4-7). Assays and treatments were matched based on the ability of the assay to best capture the biological injury elicited by the treatment (i.e., the most sensitive assay for each treatment). Overall, dose-response curves provided a comparative assessment of treatment potency across our microtissue cultures. A table summarizing all reported LC values could be referenced in the *Appendix* (App. 1.1).

From the CellTiter-Glo 3D assay, we compared the effects 2DG and oligomycin A treatment had on the ATP content of microtissues. The decrease in ATP content was associated with metabolic inhibition and ultimately cell death. 2DG is a synthetic glucose analog that inhibits glycolysis due to the intracellular accumulation of its metabolite which competitively inhibits hexokinase.[4,5] In our data, an increase in 2DG concentration resulted in the decrease of ATP content as expected. In addition, 2DG was more potent in HepG2 and MCF7 cultures, with respective LC_{50} concentrations of 52 mM and 29 mM, compared to cortical microtissues which had a LC_{50} of 110 mM. The increased potency of 2DG in HepG2 and MCF7 microtissues was expected since tumor cells rely more heavily on

anaerobic respiration through glycolysis for their metabolic needs.[6,7] This phenomenon is known as the Warburg effect. The larger detrimental effect 2DG has on tumor microtissues is compounded by the increased expression of glucose transporter proteins, like Glut1, in both cancer types.[8,9] Collectively, the increased accumulation of 2DG in the tumor cells leads to cell death as cells struggle to meet their energy demands.

On the other hand, oligomycin A is an ATP synthase inhibitor that blocks proton translocation and ultimately oxidative phosphorylation.[10,11] Interestingly, cortical microtissues were the most susceptible to oligomycin A treatment. A study conducted in rat hippocampal slices showed that oxidative phosphorylation was the major metabolic pathway that supplied ATP for neuronal activity and pre/postsynaptic action potentials.[12] These findings coincide with the increased cytotoxicity elicited by oligomycin A treatment in neurospheroids (Fig. 4). Another interesting finding involved the inability of oligomycin A treatment to produce an LC_{50} or LC_{75} in HepG2 microtissues (Fig. 4). The increased potency of oligomycin A in MCF7 compared to HepG2 was also reflected by the results from another study.[13] The source of oligomycin A resistance in HepG2 microtissues may be explained by the expression of efflux pumps such as P-glycoprotein (Pgp). Pgp is a transmembrane protein pump that belongs to a family of ATP Binding Cassette transporters that acts upon a broad range of lipophilic and amphiphilic molecules. The Pgp efflux pump has been suggested to reduce the intracellular bioavailability of molecules by binding to them while they are traversing through the cell membrane and "flipping" them to the outer membrane leaflet.[14,15] Pgp has been extensively studied, and is a well characterized mediator of multidrug resistance in cancer.[16,17] Clinically, increased Pgp expression in patients with hepatocellular carcinoma was associated with significantly poorer treatment

response and prognoses.[18] Furthermore, a study found that Pgp expression was more than three times higher in HepG2 compared to MCF7 tumor cells treated with doxorubicin.[19] The contribution of Pgp on oligomycin A resistance in HepG2 could be elucidated by co-treating HepG2 microtissues with verapamil, a known Pgp inhibitor.[19] These study findings collectively support the differences in oligomycin A potency across tissue type.

The Live/Dead assay was used to measure the cytotoxic effects resulting from membrane damage induced by Triton X-100 and melittin. Triton X-100 is a nonionic surfactant that is commonly used as an emulsifier and detergent. The pores formed by Triton X-100 increase in diameter in a dose-dependent manner resulting in increased membrane permeabilization.[20] Interestingly, LC values were similar across all microtissue types. This suggested that Triton X-100 had a similar impact regardless of the biological origin of the tissue. This is contrasted by the ~10-fold difference in LC values across melittin treated tumor and cortical microtissues (Fig. 5). Melittin is a pore-forming venom extracted from the European honeybee that forms α-helical structures in the cell membrane.[21] It was posited that melittin may insert into the membrane with varying orientations; however, after a critical lipid-to-protein ratio is reached, melittin proteins transition to form stable pores.[21,22] The ability of the tumor microtissues to better tolerate melittin treatment compared to neurospheroids may be due to their membrane repair capabilities. Previous studies have shown that tumors overexpress annexin which consequently increases their ability to repair membrane damage.[23] Additional mechanisms including membrane blebbing, shedding, and endocytosis could also be upregulated in tumors to counteract the effects of membrane poration.[24] We hypothesize that the upregulation of membrane repair mechanisms provide tumor with mechanisms to

counteract the formation of smaller pores caused by melittin but not the larger scale solubilization induced by Triton X-100. Future experiments may image melittin and Triton X-100 treated tumor microtissues using transmission election microscopy to visualize the effects of both treatments on membrane pore size and disruption.

The Caspase-Glo 3/7 3D assay was used to measure apoptotic cell death caused by cisplatin and melphalan. The assay relies on intracellular caspase-3 and -7 to cleave a proluciferin substrate which then interacts with luciferase to emit light. Both cisplatin and melphalan are alkylating agents that form intra- and interstrand crosslinks in DNA.[25–27] The accumulation of DNA damage results in downstream signaling cascades including p53 and mitogen-activated protein kinase (MAPK) which in turn activate caspase and ultimately induce apoptosis.[28–31] Cisplatin and melphalan were most potent in cortical microtissues (Fig. 6). Between the tumor microtissues, cisplatin was more potent in HepG2 while melphalan was more potent in MCF7 microtissues (Fig. 6). The difference in potency may highlight the ability of the two chemotherapies to differentially recruit or induce additional signaling cascades that activate caspase-3 or caspase-7. Another finding involved the increase in assay output to a peak value followed by a decrease in signal at higher concentrations which was found in both HepG2 and cortical microtissue dose-response curves involving cisplatin (Fig. 6a). In general, dose-response curves exhibit a ceiling or floor effect such that increasing or decreasing treatment concentration beyond the asymptotic point does not elicit a substantial change in output, respectively. Similar trends involving caspase assay activity were reported for 2D cultured HepG2 cells treated with tamoxifen which became more prominent with increased concentration and exposure time.[32] The typical progression of apoptotic cell death involves the phagocytosis of cells;

however, cells *in vitro* are not efficiently cleared resulting in secondary necrosis.[33] Under these longer exposure times and high treatment concentrations, the accumulation of apoptotic cell death devolves into secondary necrosis which ultimately leads to the decrease in caspase-3 and -7 activity. These findings highlighted the dynamic nature of cytotoxicity and the need to consider temporal factors when measuring cell death.

Finally, the effect of paclitaxel induced microtubule over-stabilization was measured through the EdU proliferation assay (Fig. 7). The over-stabilization of microtubules prevents cells from forming the mitotic spindle which effectively flags the spindle assembly checkpoint during mitosis.[34] This results in cell cycle arrest; furthermore, the abrogation of checkpoint proteins Mad2 or BubR1 resulted in chemoresistance to paclitaxel which suggested that a functional spindle assembly checkpoint is necessary for paclitaxel chemosensitivity.[35] In this study, paclitaxel was unable to produce LC values beyond the LC_{25} in cortical microtissues (Fig. 7). The diminished EdU output in neurospheroids could be explained by the lower proliferation rate of cortical cells compared to tumor cells. The neonatal rat cortical microtissues contain neuronal progenitor cells; however, the overall growth rate of the microtissues plateaus after seven days in culture.[36] Consequently, few cells are dividing at any given time in the treated neurospheroids which limited the percentage of cells vulnerable to paclitaxel treatment; similarly, only a small percentage of cells were capable of incorporating EdU into their DNA which reduced the sensitivity of the assay. Increasing the exposure time of paclitaxel or EdU in neurospheroids has the potential to increase assay output. In the tumor microtissues, HepG2 cultures required a significantly larger dose of paclitaxel to elicit the LC_{25} and LC_{50} when compared to MCF7 (Fig. 7). This differential effect could also be

explained by the increased expression of Pgp in HepG2 microtissues or the mediation of JNK signaling which was shown to promote resistance to paclitaxel treatment in HepG2 cells and other drug-resistant strains of hepatocellular carcinoma.[37,38]

2.5 Conclusion

The overall goal of this aim was to identify the ideal dose ranges for all seven treatment conditions using "best fit" assays. This was critical since we required a reliable and reproducible approach to induce cell death across multiple assay-treatment-culture combinations. As a result, the LC values calculated from the dose-response curves in this study were utilized for all further experiments. Furthermore, these dose-response curves provided invaluable information regarding the cytotoxic characteristics of various treatments. The comparison of LC_{50} values for treatments within the same assay was a relatively quick approach to evaluate the potency of a drug. Similar comparisons across different assays are difficult to interpret, thereby limiting the comprehensive analysis of cell viability across multiple assays. This highlights the need for better approaches to analyze and interpret multi-assay data in a manner that better reflects the complexity and interconnected nature of cell viability.

2.6 References

1. Riss, T. L. *et al.* Cell Viability Assays. in *Assay Guidance Manual* (eds. Markossian, S. et al.) (Eli Lilly & Company and the National Center for Advancing Translational Sciences, Bethesda (MD), 2004).

2. Hafeez, R., Nadeem, Z. & Iftikhar, S. Chapter 1 - Environmental toxicology: Fundamental and forensic. in *Trends of Environmental Forensics in Pakistan* (ed. Iftikhar, S.) 1–21 (Academic Press, 2019). doi:10.1016/B978-0-12-819436-2.00001-7.

3. Hughes, W. *Essentials Of Environmental Toxicology*. (CRC Press, London, 2019). doi:10.1201/9781315272771.

4. Pajak, B. *et al.* 2-Deoxy-d-Glucose and Its Analogs: From Diagnostic to Therapeutic Agents. *Int. J. Mol. Sci.* **21**, 234 (2019).

5. Aft, R. L., Zhang, F. W. & Gius, D. Evaluation of 2-deoxy-D-glucose as a chemotherapeutic agent: mechanism of cell death. *Br. J. Cancer* **87**, 805–812 (2002).

6. Warburg, O. & Minami, S. Versuche an Überlebendem Carcinom-gewebe. *Klin. Wochenschr.* **2**, 776–777 (1923).

7. Vander Heiden, M. G., Cantley, L. C. & Thompson, C. B. Understanding the Warburg Effect: The Metabolic Requirements of Cell Proliferation. *Science* **324**, 1029–1033 (2009).

8. Younes, M., Brown, R. W., Mody, D. R., Fernandez, L. & Laucirica, R. GLUT1 expression in human breast carcinoma: correlation with known prognostic markers. *Anticancer Res.* **15**, 2895–2898 (1995).

9. Amann, T. *et al.* GLUT1 Expression Is Increased in Hepatocellular Carcinoma and Promotes Tumorigenesis. *Am. J. Pathol.* **174**, 1544–1552 (2009).

10. Lardy, H. A., Johnson, D. & McMurray, W. C. Antibiotics as tools for metabolic studies. I. A survey of toxic antibiotics in respiratory, phosphorylative and glycolytic systems. *Arch. Biochem. Biophys.* **78**, 587–597 (1958).

11. Symersky, J., Osowski, D., Walters, D. E. & Mueller, D. M. Oligomycin frames a common drug-binding site in the ATP synthase. *Proc. Natl. Acad. Sci. U. S. A.* **109**, 13961–13965 (2012).

12. Hall, C. N., Klein-Flügge, M. C., Howarth, C. & Attwell, D. Oxidative Phosphorylation, Not Glycolysis, Powers Presynaptic and Postsynaptic Mechanisms Underlying Brain Information Processing. *J. Neurosci.* **32**, 8940–8951 (2012).

13. Doczi, J. *et al.* Viability of HepG2 and MCF-7 cells is not correlated with mitochondrial bioenergetics. *Sci. Rep.* **13**, 10822 (2023).

14. Higgins, C. F. & Gottesman, M. M. Is the multidrug transporter a flippase? *Trends Biochem. Sci.* **17**, 18–21 (1992).

15. Seelig, A. P-Glycoprotein: One Mechanism, Many Tasks and the Consequences for Pharmacotherapy of Cancers. *Front. Oncol.* **10**, (2020).

16. Leveille-Webster, C. R. & Arias, I. M. The biology of the P-glycoproteins. *J. Membr. Biol.* **143**, 89–102 (1995).

17. Bosch, I. & Croop, J. P-glycoprotein multidrug resistance and cancer. *Biochim. Biophys. Acta BBA - Rev. Cancer* **1288**, F37–F54 (1996).

18. Akimoto, M. *et al.* Relationship between therapeutic efficacy of arterial infusion chemotherapy and expression of P-glycoprotein and p53 protein in advanced hepatocellular carcinoma. *World J. Gastroenterol. WJG* **12**, 868–873 (2006).

19. Rogalska, A., Szwed, M. & Rychlik, B. The Connection between the Toxicity of Anthracyclines and Their Ability to Modulate the P-Glycoprotein-Mediated Transport in A549, HepG2, and MCF-7 Cells. *Sci. World J.* **2014**, 819548 (2014).

20. Mattei, B., Lira, R. B., Perez, K. R. & Riske, K. A. Membrane permeabilization induced by Triton X-100: The role of membrane phase state and edge tension. *Chem. Phys. Lipids* **202**, 28–37 (2017).

21. van den Bogaart, G., Guzmán, J. V., Mika, J. T. & Poolman, B. On the Mechanism of Pore Formation by Melittin. *J. Biol. Chem.* **283**, 33854–33857 (2008).

22. Lee, M.-T., Sun, T.-L., Hung, W.-C. & Huang, H. W. Process of inducing pores in membranes by melittin. *Proc. Natl. Acad. Sci. U. S. A.* **110**, 14243–14248 (2013).

23. Lauritzen, S. P., Boye, T. L. & Nylandsted, J. Annexins are instrumental for efficient plasma membrane repair in cancer cells. *Semin. Cell Dev. Biol.* **45**, 32–38 (2015).

24. Brito, C., Cabanes, D., Sarmento Mesquita, F. & Sousa, S. Mechanisms protecting host cells against bacterial pore-forming toxins. *Cell. Mol. Life Sci.* **76**, 1319–1339 (2019).

25. Fuertes, M. A., Alonso, C. & Pérez, José. M. Biochemical Modulation of Cisplatin Mechanisms of Action: Enhancement of Antitumor Activity and Circumvention of Drug Resistance. *Chem. Rev.* **103**, 645–662 (2003).

26. Falco, P. *et al.* Melphalan and its role in the management of patients with multiple myeloma. *Expert Rev. Anticancer Ther.* **7**, 945–957 (2007).

27. Osborne, M. R. & Lawley, P. D. Alkylation of DNA by melphalan with special reference to adenine derivatives and adenine-guanine cross-linking. *Chem. Biol. Interact.* **89**, 49–60 (1993).

28. Siddik, Z. H. Cisplatin: mode of cytotoxic action and molecular basis of resistance. *Oncogene* **22**, 7265–7279 (2003).

29. Tanida, S. *et al.* Mechanisms of Cisplatin-Induced Apoptosis and of Cisplatin Sensitivity: Potential of BIN1 to Act as a Potent Predictor of Cisplatin Sensitivity in Gastric Cancer Treatment. *Int. J. Surg. Oncol.* **2012**, 862879 (2012).

30. Dasari, S. & Tchounwou, P. B. Cisplatin in cancer therapy: molecular mechanisms of action. *Eur. J. Pharmacol.* **740**, 364–378 (2014).

31. Blanc, C. *et al.* Caspase-3 is essential for procaspase-9 processing and cisplatin-induced apoptosis of MCF-7 breast cancer cells. *Cancer Res.* **60**, 4386–4390 (2000).

32. Riss, T. L. & Moravec, R. A. Use of Multiple Assay Endpoints to Investigate the Effects of Incubation Time, Dose of Toxin, and Plating Density in Cell-Based Cytotoxicity Assays. *ASSAY Drug Dev. Technol.* **2**, 51–62 (2004).

33. Rogers, C. *et al.* Cleavage of DFNA5 by caspase-3 during apoptosis mediates progression to secondary necrotic/pyroptotic cell death. *Nat. Commun.* **8**, 14128 (2017).

34. Awosika, A. O., Farrar, M. C. & Jacobs, T. F. Paclitaxel. in *StatPearls* (StatPearls Publishing, Treasure Island (FL), 2025).

35. Sudo, T., Nitta, M., Saya, H. & Ueno, N. T. Dependence of Paclitaxel Sensitivity on a Functional Spindle Assembly Checkpoint. *Cancer Res.* **64**, 2502–2508 (2004).

36. Dingle, Y.-T. L. *et al.* Three-Dimensional Neural Spheroid Culture: An In Vitro Model for Cortical Studies. *Tissue Eng. Part C Methods* **21**, 1274–1283 (2015).

37. Chae, S., Kim, Y. B., Lee, J.-S. & Cho, H. Resistance to paclitaxel in hepatoma cells is related to static JNK activation and prohibition into entry of mitosis. *Am. J. Physiol.-Gastrointest. Liver Physiol.* **302**, G1016–G1024 (2012).

38. Takano, M. *et al.* Paclitaxel-resistance Conferred by Altered Expression of Efflux and Influx Transporters for Paclitaxel in the Human Hepatoma Cell Line, HepG2. *Drug Metab. Pharmacokinet.* **24**, 418–427 (2009).

CHAPTER 3: MULTIVARIATE ASSESSMENT OF VIABILITY

Zein-Sabatto, A., St. Angelo, K., Madnick S.J., Hoffman-Kim, D., Morgan J.R., & Lee, J. Multi-assay assessment of cytotoxicity reveals multiple mechanisms of action in 3D microtissues. *Sci. Rep.* **15**, 3090 (2025).

Data from Chapters 2 and 3 were published in the same manuscript. They were presented as separate chapters herein to highlight their distinct contributions to study aims and improve comprehensibility.

3.1 Introduction

Cell death is a complex process that involves a multitude of independent, concurrent, and mediatory pathways that occur within an injured cell. Clinically, cell death does not occur as a monolithic process. In fact, multiple cell death pathways have been simultaneously observed in heart disease, cancer, and Alzheimer's disease.[1–5] Cells experiencing the same perturbation may initiate a variety of cellular responses. For instance, activation of the tumor suppressor gene *p53* through cellular stress can set forth cascades utilized by both autophagy and apoptosis.[6] Another significant source of overlap between cell death pathways involves mitochondrial disruption. The activation of proapoptotic proteins through extrinsic signaling or internal stressors can induce mitochondrial outer membrane permeabilization.[7] This leads to the release of cytochrome c which continues the apoptotic signaling cascade through caspase-3/7 activation.[7]

Alternatively, the formation of the mitochondrial permeability transition pore (MPTP) leads to the depolarization of the inner membrane resulting in organelle swelling, calcium deregulation, and the loss of ATP production.[8] The rapid depletion of ATP is a hallmark feature of necrosis which effectively inhibits the ATP-dependent apoptotic pathway.[9] In addition, the deleterious effects of mitochondrial injury involve the accumulation of cytosolic calcium levels which mediates necroptosis through activation of RIP3 and calcium-calmodulin kinase II.[10–12] Cell death pathways may also converge through multifunctional proteins like caspase-8 which has been implicated in apoptosis, autophagy, pyroptosis, and necroptosis.[13,14] More specifically, the inhibition of caspase-8 has been linked with increased autophagy through *ATG7* and *beclin 1* gene activation.[15] Meanwhile, activation of caspase-8 activity was linked to the inhibition of pro-necroptotic and proinflammatory proteins including RIPK1, RIPK3, and CYLD.[16–19]

The interactions between multiple mechanisms of cell death are also present in cancer treatment. Traditionally, apoptosis was viewed as the primary mechanism of cell death induced by anticancer drugs; however, many studies have challenged this claim.[20,21] The type of cell death experienced by cells is contextual and depends on multiple factors including cell type, genotype, concentration of treatment, and metabolic activity.[21–23] Therefore, differences in cell fate from within the same tumor are expected to arise from genetic heterogeneity, nutrient gradients, and bioavailability of treatments. Anticancer therapies have also been shown to elicit multiple pathways within tumors. Sorafenib, a tyrosine kinase inhibitor, induced both apoptosis and autophagy in prostate cancer cells.[24] Meanwhile, a study that investigated the effects of paclitaxel on gastric cancer cells revealed the presence of mitotic catastrophe, cellular senescence, autophagy, and

apoptosis.[25] Similarly, doxorubicin, a commonly used chemotherapy for solid tumors, exhibited dose-dependent induction of mitotic catastrophe with low doses and a transition to apoptotic cell death at higher doses.[26] Collectively, these results highlight the need for multi-assay assessments of cell viability to better understand the complex and intricate nature of cell death.

The presence of crosstalk and interactions between cell death pathways is a topic of active discussion, and the examples given provide a small glimpse into a growing field of study. The exact biological mechanisms responsible for overlap in cell death pathways is beyond the scope of this thesis; however, this study implemented an empirical approach to measure the cytotoxic contribution of multiple cell death pathways following distinct cellular perturbations. This was accomplished by collecting data from four distinct assays for each treatment type; nevertheless, the holistic interpretation of multi-assay data is challenging. Common statistical tests, including t-tests and ANOVA, must be conducted independently for each assay. The direct comparison of analytical and statistical outputs across the different assays is logically tenuous. Furthermore, fulfilling all the prerequisites for a single statistical analysis across all groups of a HTS study is challenging considering normality, homoscedasticity, and sample sizes requirements are difficult to satisfy in real-world biological data.[27–29] In this aim, we demonstrated the analysis of multi-assay data through multivariate approaches to help address the aforementioned limitations. This included the implementation of linear mixed effects (LME) models and principal component analysis (PCA) to provide a more robust framework to analyze multimodal datasets.

3.1.1 Multivariate Approaches to Analyze Cell Viability Data

In this study, LME and PCA multivariate approaches were implemented to analyze multimodal data collected from four assays, seven treatments, and three microtissue cultures. Both approaches provided insightful analytical perspectives regarding the interpretability of the cell viability data. LME models are versatile and widely used approaches that are more powerful implementations of linear regressions. These models are particularly well-suited to model grouped data formats including longitudinal, repeated measures, and multilevel data.[30] LME models incorporate fixed effects, which are the experimentally captured variables, and random effects, which involve the inherent variation caused by randomly selecting samples from a population.[30] In addition to random effects, within-group residual errors are calculated to provide more accurate modeling of the dataset.[31] The basic model can be described by Equation 5

$$\text{Equation 5} \qquad y = \boldsymbol{X}\beta + \boldsymbol{Z}b + \epsilon$$

where y is the column vector of the output responses, X is the design matrix of predictor variables, β is the column vector containing fixed effects regression coefficients, Z is the design matrix of random effects and groups, b is the column vector of random effects for each group, and ε is the residual error. The model equation allows for the coupling of corresponding fixed and random effects.[31] Parameter estimates for the equation can be calculated using different methods; however, restricted maximum likelihood estimation was used in this study to maximize the log-profile-restricted-likelihood.[31] In this study, LME regression fits and their extracted slopes were utilized to capture the assay response for each treatment combination.

PCA is an interdisciplinary statistical technique used for the reduction of dimensionality in larger datasets.[32] It enables the extraction of features that best capture the variance in data while minimizing data loss. PCA accomplishes this by identifying new, arbitrary variables (also known as principal components) that are linear combinations of variables from the original dataset. The data is generally centered and standardized, then the multidimensional data is fitted to minimize the sum of the squared distances from each datapoint to a fitted line.[33] This line of best fit is called the first component (PC1); subsequently, the second component (PC2) is derived by taking a line perpendicular to the first that minimizes the sum of the squared distances.[33] This process can be repeated to extract all principal components. The vector components of PC1 are reported as the eigenvectors which capture the direction of the principal component. Eigenvalues represent the magnitude of importance or spread of each eigenvector. Eigenvectors with the smallest eigenvalues are dropped to reduce the complexity of the dataset whilst maintaining the most relevant information. PCA can be reliably performed on datasets with linear relationships, highly correlated independent variables, and large sample sizes. They are also robust against deviations in normality assumptions.[32] Ultimately, PCA generates a series of linear equations for each principal component in the form of Equation 6

$$\text{Equation 6} \qquad PC_i = w_{i,1}X_1 + w_{i,2}X_2 \cdots + w_{i,n}X_n$$

where the *i*th principal component is calculated by the linear combination of variable X multiplied by its respective weight, or eigenvector, w. In this study, PCA was used to compare inter-assay response through PCA loadings and a newly derived metric termed multi-mechanisms LC_{50} ($MMLC_{50}$). The implementation of both LME and PCA provided

a unique opportunity to analyze multivariate assay data. Unlike traditional parametric and nonparametric approaches, the multivariate approaches utilized herein provided a more direct interpretation of cell viability.

3.2 Methods

3.2.1 Cell Culture and Three-Dimensional Microtissue Formation

Detailed methods and protocols used to culture, passage, and maintain the HepG2 and MCF7 tumor microtissues were provided in *Section 2.2.1: Cell Culture*. The protocol for primary neonatal cortical rat cell isolation was previously provided in *Section 2.2.1: Cell Culture: Primary Neonatal Rat Cortical Cell Isolation*. Methods describing the generation of the agarose 96-microwell arrays and the seeding of the three-dimensional microtissues were provided in *Section 2.2.2: Three-Dimensional Microtissue Culture.*

3.2.2 Multi-Assay Compound Treatment

Treatment stock and working solutions were generated using similar methods described in detail in *Section 2.2.3: Compound Treatment*; however, serial dilutions were not implemented to induce cellular perturbations for this study aim. Instead, the precalculated lethal concentrations (LCs) that elicited 25, 50, and 75 percent cell death from the "best fit" assay-treatment pairs were utilized across all assays. In some instances, LC values could not be achieved using predetermined solubility and media displacement guidelines described in the previous chapter. Treatment LCs that were unachievable were

excluded from the study. A summary table of all LCs used in this aim can be referenced in the *Appendix* (App. A1). All treatments involved 24-hour exposure periods.

3.2.3 Luminescence and Fluorescence Assay Protocols

The methods used to collect data from the CellTiter-Glo 3D, Live/Dead cytotoxicity, Caspase-Glo 3/7 3D, and Click-iT EdU Proliferation assays were identical to the ones used in *Sections 2.2.4* through *2.2.7*.

3.2.4 Image Processing

The image processing pipelines for fluorescence images acquired using the Live/Dead and EdU proliferation assays were identical to those used in *Section 2.2.8*.

3.2.5 Statistical Analysis

For this study aim, changes in cell viability were analyzed using all combinations of assays, treatments, and microtissue culture types using previously determined LCs and 24-hour exposure periods. Data collection from the CellTiter-Glo 3D and Caspase-Glo 3/7 3D assays for HepG2 and cortical microtissues included eight microtissues per treatment concentration and two independent experiment replicates. Data outputs from MCF7 microtissues involved three gels per treatment concentration and two independent experiments. Live/Dead and EdU proliferation assays extracted a total of 20 microtissues per treatment condition and two independent experiment replicates for all microtissue types, except for HepG2 cultures which included three independent experiments. A total of 8,758 datapoints were collected instead of the anticipated 9,408 since not all treatments

elicited the full range of LCs without exceeding solubility and media displacement guidelines. Data normalization was conducted in a manner similar to that of the previous chapter. In brief, CellTiter-Glo 3D and Caspase-Glo 3/7 3D luminescent output was normalized by the cross-sectional pixel area from each microtissue for HepG2 and cortical microtissues. All assay data were normalized by the means from their respective vehicle controls.

Linear Mixed Effects Models

After data preprocessing, assay outputs were fitted to a linear regression using a LME model with 95% confidence intervals using a custom MATLAB (MathWorks) code. A regression fit was deemed significant if it had a $p<0.05$ and a slope magnitude greater than 0.1. The slope threshold of 0.1 ensured that assay output changed by at least 10% of the expected outcome which was used to identify any nonresponding assays. Additional exclusion criteria were implemented to ensure the linearity of all LME regression fits. This was of particular importance since some assay outputs plateaued at higher treatment concentrations. To determine whether the LC_{75} treatment condition was to be excluded from the model fit, a single-tailed t-test between the LC_{75} and LC_{50} treatment groups was conducted when both passed normality and equal variance assumptions. If either subset of data failed the test, the statistical test was conducted on the bootstrapped data. The LC_{75} dataset was excluded from the fit when its group mean was not statistically different from the LC_{50} group mean (i.e., $p > 0.05$ and therefore we accept the null hypothesis). If the LC_{75} was excluded, the same exclusion criteria were applied between the LC_{50} and LC_{25}. The slopes from the LME fit regressions were extracted and plotted. Slope values were expected to be negative since an increase in treatment concentration led to a decrease in

assay output. The Caspase-Glo 3/7 3D assay was the only exception since increased cell death through apoptosis was measured by an increased signal output. This would result in a positive slope. For an integrative slope comparison across all assays, caspase assay slope fits were normalized by the mean of the slopes from the standard-pair treatment (i.e., cisplatin and melphalan) and then multiplied by -1.0, such that the average slope from the cisplatin and melphalan treated microtissues became -1.0.

Principal Component Analysis

PCA and its subsequent statistical tests were conducted in JMP Pro 16 (JMP Statistical Discovery LLC.) using the same dataset from the LME model regression fits. Prior to PCA, data preprocessing was implemented. Live/Dead and EdU assay datasets were truncated to match the sample sizes of the CellTiter-Glo 3D and Caspase-Glo 3/7 3D assays. This was necessary since PCA cannot be conducted on datasets with mismatched sample sizes. To achieve this, eight out of 20 microtissues per treatment concentration per experimental replicate were randomly selected for HepG2 and cortical microtissues analyzed by the Live/Dead and EdU assays. Similarly, MCF7 datasets analyzed by Live/Dead and EdU assays were truncated by randomly selecting three out of 20 datapoints per treatment concentration per experimental replicate.

Next, all data was normalized to its vehicle control except for Caspase-Glo 3/7 3D assay data which was normalized by Equation 7

$$\text{Equation 7} \qquad x = 1 - \frac{x_i}{\bar{x}_{LC75}}$$

where x is the normalized datapoint, x_i is the raw datapoint, and $\bar{x}$ is the mean from the LC_{75} treatment group. PCA was conducted on the covariances and the eigenvalues, eigenvectors, variances, and Bartlett's test of sphericity ($\chi^2 < 0.05$ considered significant) for PC1 were determined. The eigenvector and eigenvalues were calculated by Equation 8

Equation 8 $$Covariance\ Matrix \cdot Eigenvector = Eigenvalue \cdot Eigenvector$$

where the covariance matrix is an n x n matrix that captures variable variance along the diagonal and the covariance between paired variables along the off-diagonal elements. PCA loadings combine the magnitude and direction of each variable relative to a principal component. Loadings were calculated using Equation 9.

Equation 9 $$Loadings = \frac{Eigenvector * \sqrt{Eigenvalue}}{Standard\ Deviation}$$

Extracting $MMLC_{50}$

PC1 and PC2 data transformations for all outputs were derived using Equation 6. Scatterplots for each treatment-culture combination were used to visualize the data using SigmaPlot 15.0 (Systat Software Inc.). Next, PC1 transformed data was plotted against the LC of any given treatment and fitted to a second-order polynomial in SigmaPlot 15.0. The new $MMLC_{50}$ was derived by taking two-thirds of the data range and subtracting it from the mean value of PC1 at the control (i.e., the mean y-value for the control group). The point on the line that corresponded to the calculated difference was projected onto the x-axis and represented the new $MMLC_{50}$. The $MMLC_{50}$ was converted to its representative molar concentration by solving the equation of the line extracted from the nonlinear mixed effects model from the previous chapter.

3.3 Results

Previously, treatments were analyzed using a “best fit” assay that was anticipated to be the most sensitive to changes in viability relative to the treatment’s mechanism of action. This conventional approach does not investigate the unanticipated or off-target effects a treatment may have on other biomarkers associated with cell death. For instance, the disruption to the membrane caused by the pore-forming agents melittin and Triton X-100 were measured using the Live/Dead assay. This assay quantified the pervasiveness of membrane injury through increased signal from ethidium homodimer staining which is a cell impermeant dye. Nevertheless, membrane disrupting agents may also affect metabolic health, induce apoptosis, or curtail proliferation. To investigate the multimodal interactions between cell death pathways and assay sensitivity, we tested all combinations of treatments and assays using previously calculated LC values (App. A1).

3.3.1 Linear Mixed Effects Models

Assay outputs from each testing condition were plotted using a LME model, and a simple regression was fitted to the data. From these linear regressions, we expected the slopes of the line to be -1.0 if the change in viability captured by the assay decreased proportionally to the increase in LC. In other words, a 25% increase in concentration would lead to an additional 25% loss in cell viability. For the CellTiter-Glo 3D assay, this expectation was observed except for HepG2 microtissues treated with oligomycin A which produced a steeper slope (Fig. 8). Assay outputs plateaued at the highest tested LCs for all

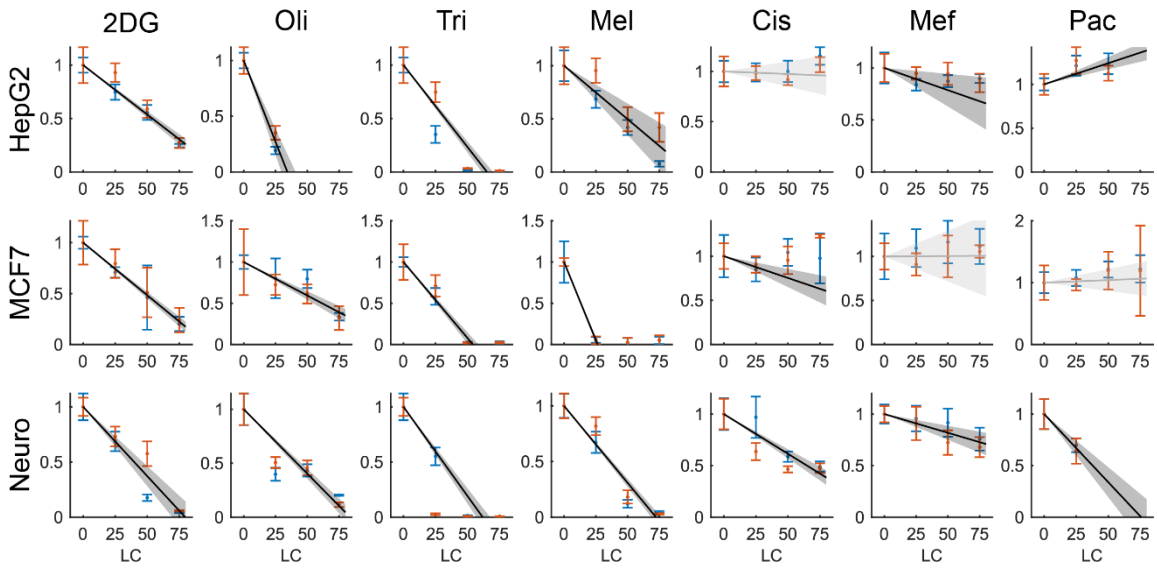

Figure 8. Linear regressions from the CellTiter-Glo 3D assay. CellTiter-Glo 3D data was collected from various compounds (columns) in various microtissues (rows) using previously derived lethal concentrations. Data from neurospheroids and HepG2 microtissues were initially normalized by their cross-sectional area, and all data was normalized to their controls. A regression was fitted to each treatment group using a linear mixed effects model (LME, black lines). Error bars and shaded gray regions signify the 95% confidence intervals. A dose-response was considered substantial when the p-value of the LME fit was $p<0.05$ and the absolute value of the slope was greater than 0.1 (dark gray). HepG2 and neurospheroid graphs contained eight microtissues per datapoint and two independent experiments (blue and orange). MCF7 graphs contained three gels per datapoint and two independent experiments (blue and orange). 2DG: 2-Deoxy-D-glucose, Oli: oligomycin A, Tri: Triton X-100, Mel: melittin, Cis: cisplatin, Mef: melphalan, Pac: paclitaxel, Neuro: neurospheroid. See methods for data fit exclusion criterion. Published in Zein-Sabatto A., et al., 2025.

microtissues treated with Triton X-100 and MCF7 treated with melittin. Treatments that produced negligible changes to the CellTiter-Glo 3D assay output included HepG2 treated with cisplatin as well as MCF7 treated with melphalan and paclitaxel (light gray lines, Fig. 8). Interestingly, ATP content increased significantly in HepG2 microtissues treated with paclitaxel.

Similar analysis was conducted for the Live/Dead assay (Fig. 9). Slopes of -1.0 were observed in “best fit” treatment-assay combinations for all microtissues (i.e., columns pertaining to Triton X-100 and melittin). Live/Dead assay output did not plateau at higher LC concentrations or produce positive slopes for any testing combination.

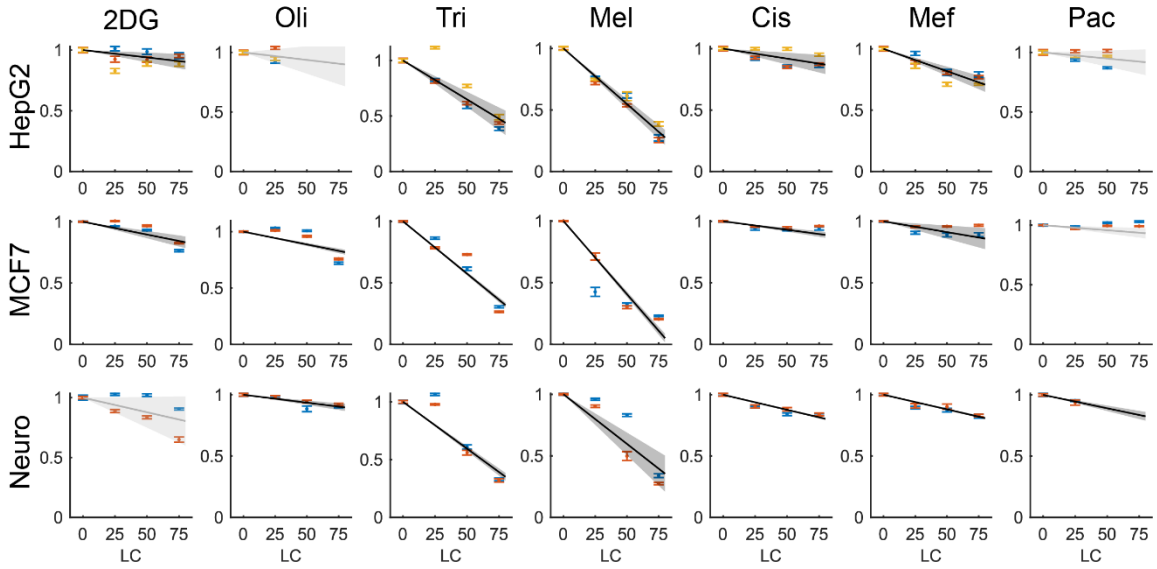

Figure 9. Linear regressions from the Live/Dead assay. Live/Dead Viability/Cytotoxicity assay data was collected from various compounds (columns) in various microtissues (rows) using previously derived lethal concentrations. Data from all microtissues was normalized to their controls. A regression was fitted to each treatment group using a linear mixed effects model (LME, black lines). Error bars and shaded gray regions signify the 95% confidence intervals. A dose-response was considered substantial when the p-value of the LME fit was $p<0.05$ and the absolute value of the slope was greater than 0.1 (dark gray). All datapoints contained 20 microtissues per condition and two (neurospheroid and MCF7) or three (HepG2) independent experiments (blue, orange, and yellow, respectively). 2DG: 2-Deoxy-D-glucose, Oli: oligomycin A, Tri: Triton X-100, Mel: melittin, Cis: cisplatin, Mef: melphalan, Pac: paclitaxel, Neuro: neurospheroid. See methods for data fit exclusion criterion. Published in Zein-Sabatto A., et al., 2025.

Negligible assay outputs were reported for HepG2 microtissues treated with oligomycin and paclitaxel, MCF7 treated with paclitaxel, and cortical microtissues treated with 2DG (light gray lines, Fig. 9).

Data from the Caspase-Glo 3/7 3D assay produced a variety of regression fits (Fig. 10). Treatments that elicited a proportional change in viability with regards to assay output were expected to have a slope of 1.0; however, the data normalization for the caspase assay prevented this expected outcome. Data normalization to vehicle controls resulted in the reporting of apoptotic activity relative to baseline levels rather than providing a percent decrease in cell viability. Nevertheless, differences in caspase 3/7 activity across treatments

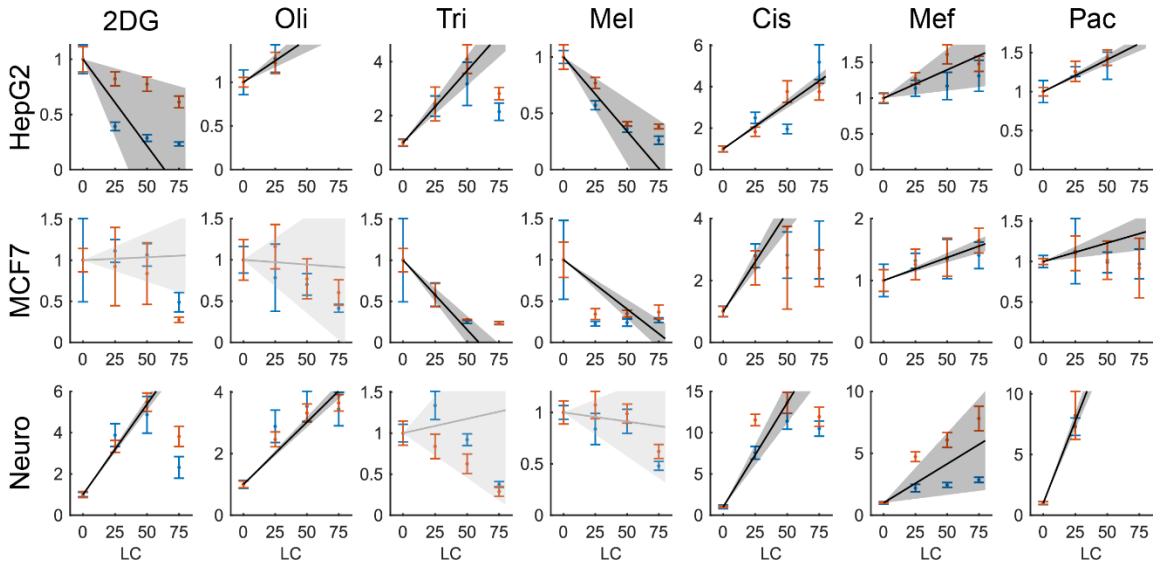

Figure 10. Linear regressions from the Caspase-Glo 3/7 3D assay. Caspase-Glo 3/7 3D apoptotic data was collected from various compounds (columns) in various microtissues (rows) using previously derived lethal concentrations. Data from neurospheroids and HepG2 microtissues were initially normalized by their cross-sectional area, and all data was normalized to their controls. A regression was fitted to each treatment group using a linear mixed effects model (LME, black lines). Error bars and shaded gray regions signify the 95% confidence intervals. A dose-response was considered substantial when the p-value of the LME fit was $p<0.05$ and the absolute value of the slope was greater than 0.1 (dark gray). HepG2 and neurospheroid graphs contained eight microtissues per datapoint and two independent experiments (blue and orange). MCF7 graphs contained three gels per datapoint and two independent experiments (blue and orange). 2DG: 2-Deoxy-D-glucose, Oli: oligomycin A, Tri: Triton X-100, Mel: melittin, Cis: cisplatin, Mef: melphalan, Pac: paclitaxel, Neuro: neurospheroid. See methods for data fit exclusion criterion. Published in Zein-Sabatto A., et al., 2025.

were observed. Caspase activity increased for most treatments but significantly dropped in HepG2 microtissues treated with 2DG and melittin as well as MCF7 microtissues treated with Triton X-100 and melittin. Negligible changes to caspase 3/7 activity were observed in MCF7 microtissues treated with 2DG and oligomycin A as well as cortical microtissues treated with Triton X-100 and melittin (light gray lines, Fig. 10).

Finally, LME regression fits were reported for the Click-iT EdU proliferation assay (Fig. 11). Paclitaxel treatment in MCF7 and cortical microtissues were unable to produce slopes of -1.0 while it produced a steeper slope in HepG2 cultures. Assay plateaus were observed across many testing conditions including HepG2 microtissues treated with Triton

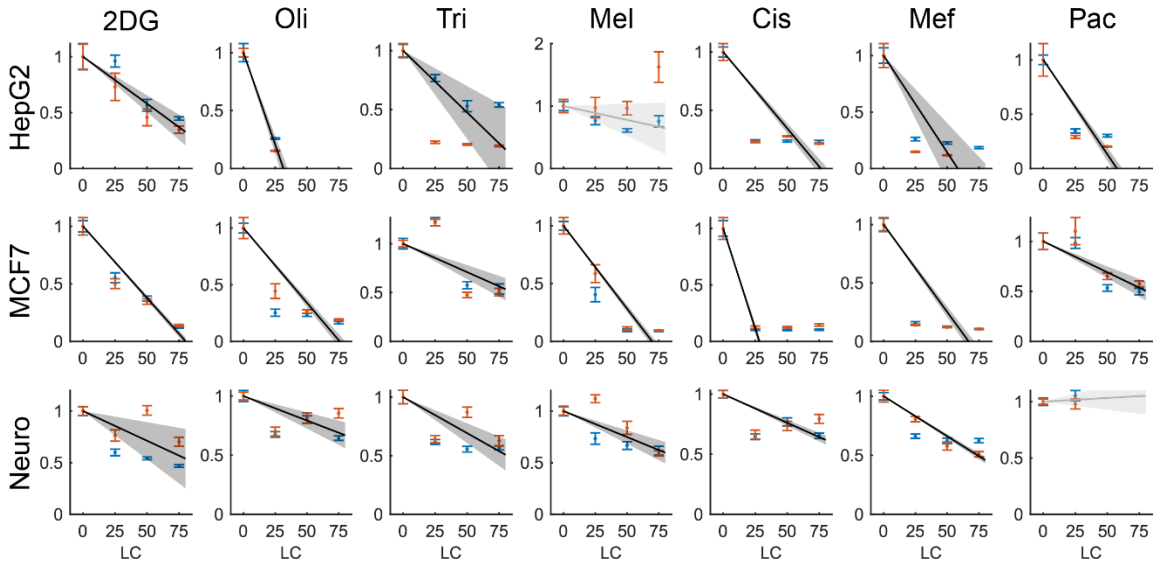

Figure 11. Linear regressions from the Click-iT EdU proliferation assay. EdU proliferation assay data was collected from various compounds (columns) in various microtissues (rows) using previously derived lethal concentrations. Data from all microtissues was normalized to their controls. A regression was fitted to each treatment group using a linear mixed effects model (LME, black lines). Error bars and shaded gray regions signify the 95% confidence intervals. A dose-response was considered substantial when the p-value of the LME fit was $p<0.05$ and the absolute value of the slope was greater than 0.1 (dark gray). All datapoints contained 20 microtissues per condition and two independent experiments (blue and orange). 2DG: 2-Deoxy-D-glucose, Oli: oligomycin A, Tri: Triton X-100, Mel: melittin, Cis: cisplatin, Mef: melphalan, Pac: paclitaxel, Neuro: neurospheroid. See methods for data fit exclusion criterion. Published in Zein-Sabatto A., et al., 2025.

X-100, cisplatin, and melphalan as well as MCF7 microtissues treated with oligomycin A, melittin, cisplatin, and melphalan. Negligible changes to proliferation were observed in HepG2 cultures treated with melittin and neurospheroids treated with paclitaxel (light gray lines, Fig. 11).

Slopes from all LME regression analyses were reported in Figure 12. As previously mentioned in *Section 3.2.5:Statistical Analysis: Linear Mixed Effects Models*, the slopes for all Caspase-Glo 3/7 3D assay data were normalized by the average slope from both "best fit" treatment pairs (i.e., cisplatin and melphalan) for each culture type and multiplied

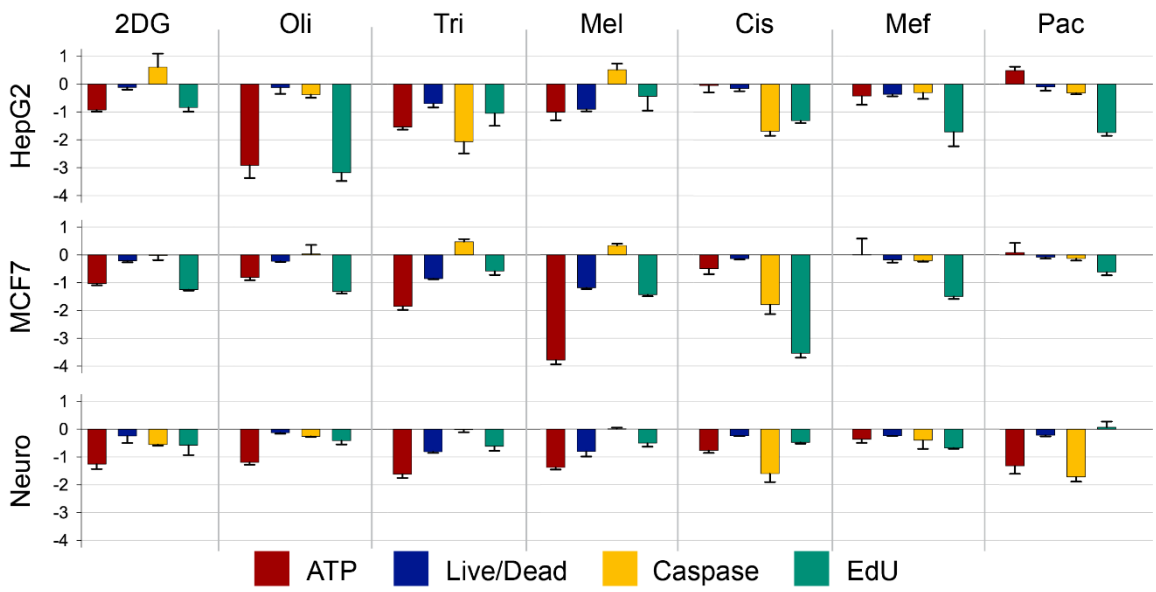

Figure 12. Slopes derived from linear mixed effects models fitted with linear regressions for all conditions. These slopes captured inter-assay response to various treatments (columns) in all tissue culture types (rows). Error bars represent 95% confidence intervals in the slopes. Different colors represent the different assays used (red: CellTiter-Glo 3D, blue: Live/Dead, yellow: Caspase-Glo 3/7 3D, cyan: Click-iT EdU proliferation assay). 2DG: 2-Deoxy-D-glucose, Oli: oligomycin A, Tri: Triton X-100, Mel: melittin, Cis: cisplatin, Mef: melphalan, Pac: paclitaxel, neuro: neurospheroid. Published in Zein-Sabatto A., et al., 2025.

by -1 for consistent visual comparison across testing conditions. This approach allowed for the direct assessment of assay responses across different treatments and culture types. Multiple assay outputs responded significantly to each treatment tested, and the "best fit" assay-treatment pairs were occasionally outperformed. For example, the caspase assay was outperformed by the EdU assay for cisplatin and melphalan treatments. Similarly, the ATP assay outperformed the Live/Dead assay in MCF7 microtissues treated with melittin (Fig. 12)

3.3.2 Principal Component Analysis

While the LME regression slopes provided comprehensive insight regarding the assay response to various treatments, its results remain convoluted. This approach did not

comprehensively assess the combinatory and concurrent effects from the different mechanisms of cytotoxicity. To address this, we proposed a novel method that derived a comprehensive LC value through PCA. Simulated data was used to establish the method's feasibility (Fig. 13). For simplicity, two simulated dose-response curves were used for the

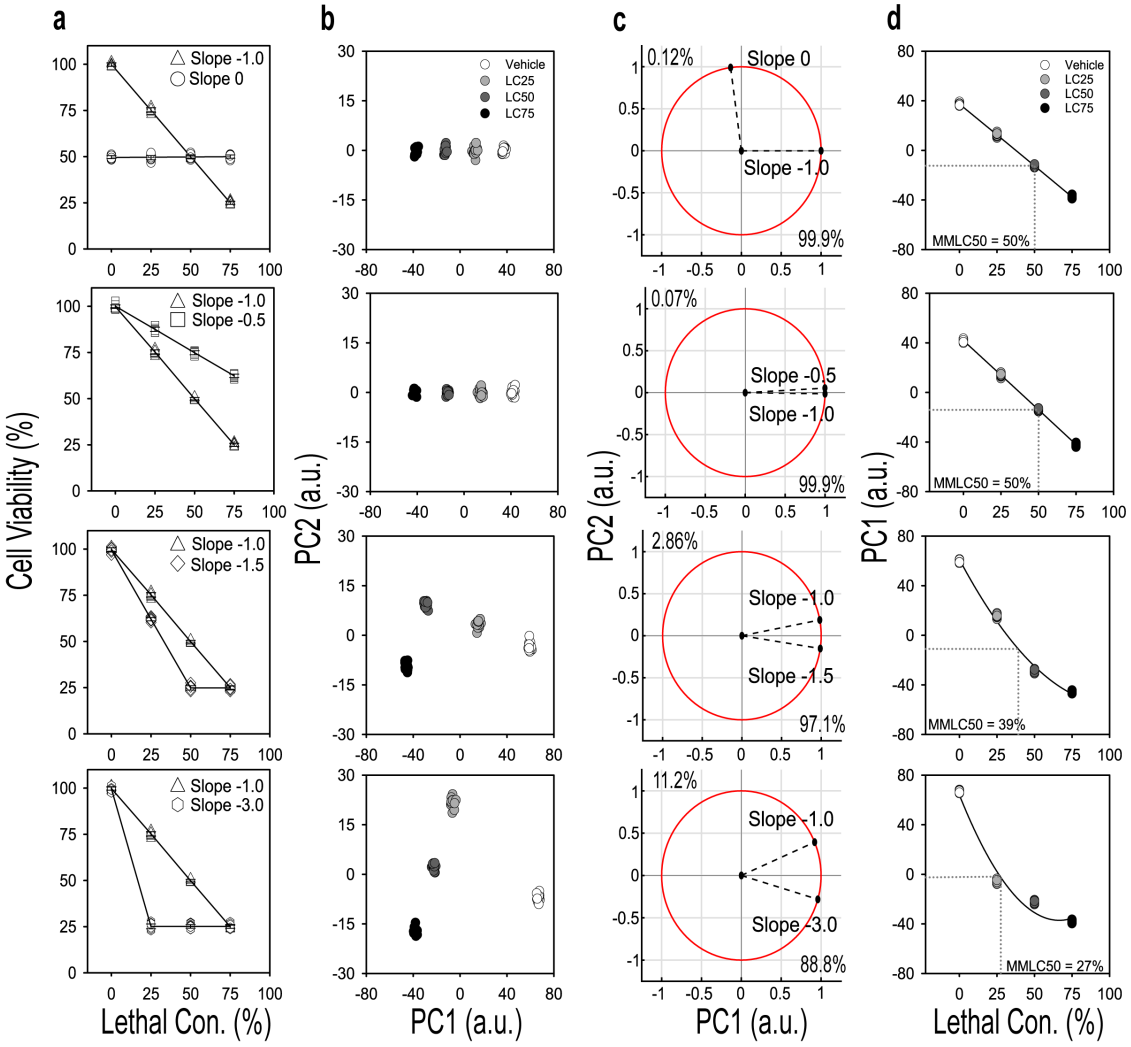

Figure 13. Dose-response simulation data validates the use of principal component analysis (PCA) to analyze multimodal datasets. (**a**) Input dose-response curves with slopes of increasing magnitude (top to bottom) were plotted against the ideal response which generates a slope of -1.0 (triangles). (**b**) The first two principal components (PC1 and PC2) from the PCA were plotted on a scatterplot. (**c**) PCA loadings for both components were plotted along a red unit circle. Loading plot vectors (dashed lines) display the magnitudes of both PC1 and PC2 loadings when projected onto their respective axis. The percentages displayed near the x and y axes represent the percent of data variation captured by PC1 and PC2, respectively. (**d**) PC1 from each simulation was plotted against its theoretical lethal concentration, and a second order polynomial was fitted to the data (black lines). Multi-mechanisms LC_{50} ($MMLC_{50}$) was calculated by taking two-thirds of the full data range and subtracting it from the vehicle control PC1 value, then projecting that value on the x axis (gray dotted lines). Published in Zein-Sabatto A., et al., 2025.

proof-of-concept example. One dose-response curve maintained the expected slope of -1.0 from "best fit" assays and the second dose-response curve had varying slopes of 0, -0.5, -1.5, and -3.0 (Fig. 13a). PCA scatterplots and loading plots provided visual information regarding the correlation between the two datasets (Fig. 13b, c). The $MMLC_{50}$, which was described in more detail in *Section 3.2.5:Statistical Analysis: Extracting $MMLC_{50}$*, was derived for each scenario (Fig. 13d). Simulation data revealed the leftward shift of the $MMLC_{50}$ as slopes surpassed the -1.0 dose-response curve. Furthermore, the $MMLC_{50}$ shifted by a larger magnitude when the dose-response curve was steeper.

Next, the multi-assay dataset was analyzed using this proposed approach. Prior to running the PCA, all data was normalized by its control group except for caspase assay data which was normalized using Equation 7. PCA scatterplots and second-order polynomial fits were reported for each treatment-culture combination (Figs. 14, 15, and 16). Furthermore, the percentage of variance captured by PC1 and PC2 relative to the dataset was reported. $MMLC_{50}$ derivations required a LC_{75}; consequently, testing conditions that did not contain a LC_{75} were excluded from the polynomial fit and $MMLC_{50}$ extraction. These included HepG2-oligomycin, HepG2-paclitaxel, and neurospheroid-paclitaxel treatment combinations. Interestingly, PCA isolated the different LC conditions into different clusters. In general, the $MMLC_{50}$ either approximated the LC_{50} or shifted leftward. The largest shift involved HepG2 microtissues treated with melphalan which had an $MMLC_{50}$ of 17.6% (Fig. 14f). This was closely followed by MCF7 microtissues treated with cisplatin which had a $MMLC_{50}$ of 17.9% (Fig. 15e). Notably, the $MMLC_{50}$ shifted rightward for MCF7 cultures treated with paclitaxel (Fig. 15g). A table summarizing all LC and $MMLC_{50}$ values was provided in the *Appendix* (App. A1).

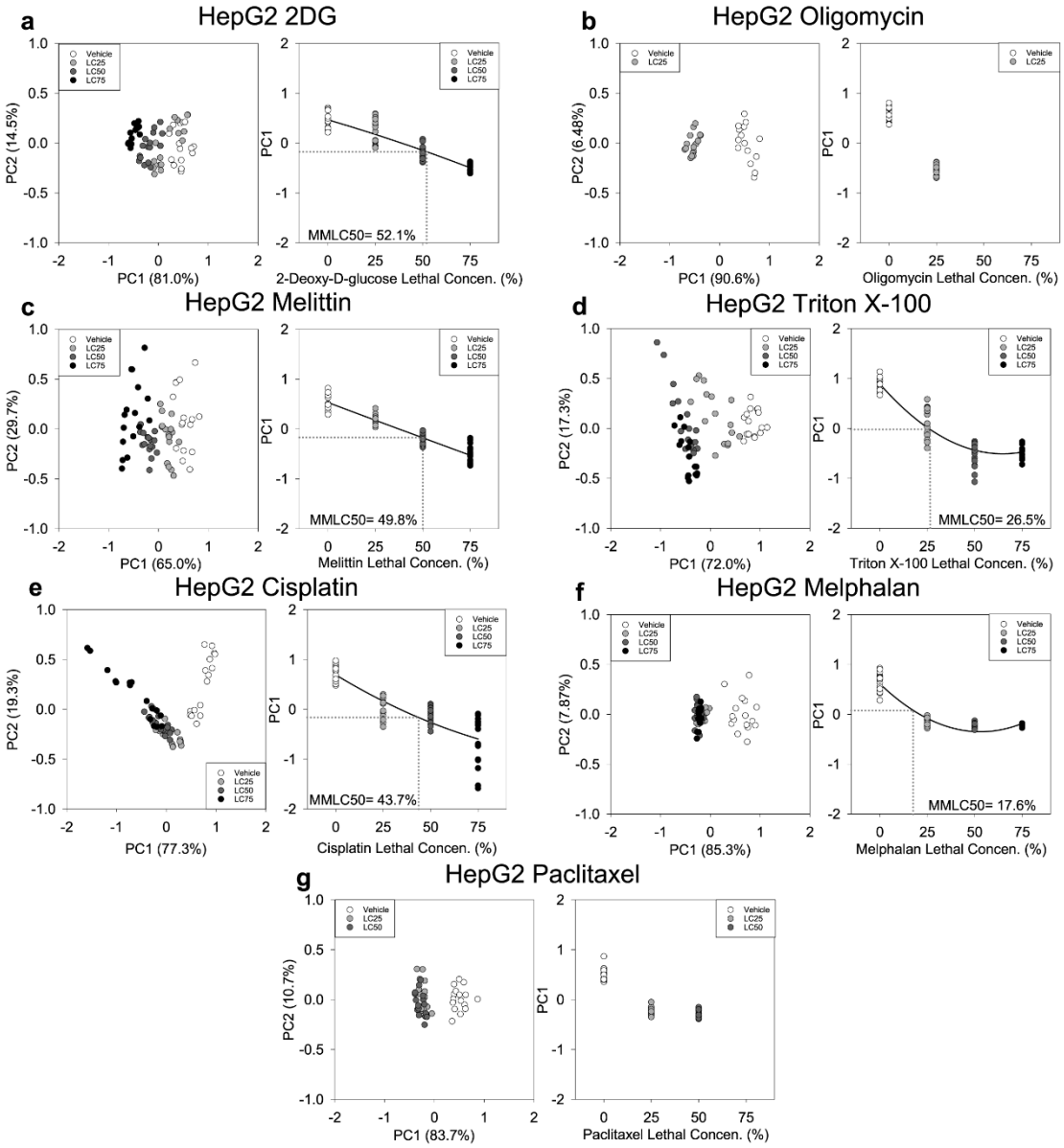

Figure 14. Principal component analysis (PCA) panel of HepG2 microtissues treated with various compounds. HepG2 multimodal data which contained results from four independent assays using previously determined lethal concentrations (LC) were transformed to two principal components (PC1 and PC2) using PCA. Scatterplots visualized the distribution of the data, and the percentage of variance captured by each component was reported. PC1 data was also plotted as a function of lethal concentration, and a second order polynomial was fitted to the data (black lines). Multi-mechanisms LC_{50} ($MMLC_{50}$) was calculated by taking two-thirds of the full data range and subtracting it from the vehicle control PC1 value, then projecting that value on the x axis (gray dotted lines). Each condition contained 16 microtissues (n=8 microtissues per condition and two independent experiments). Published in Zein-Sabatto A., et al., 2025.

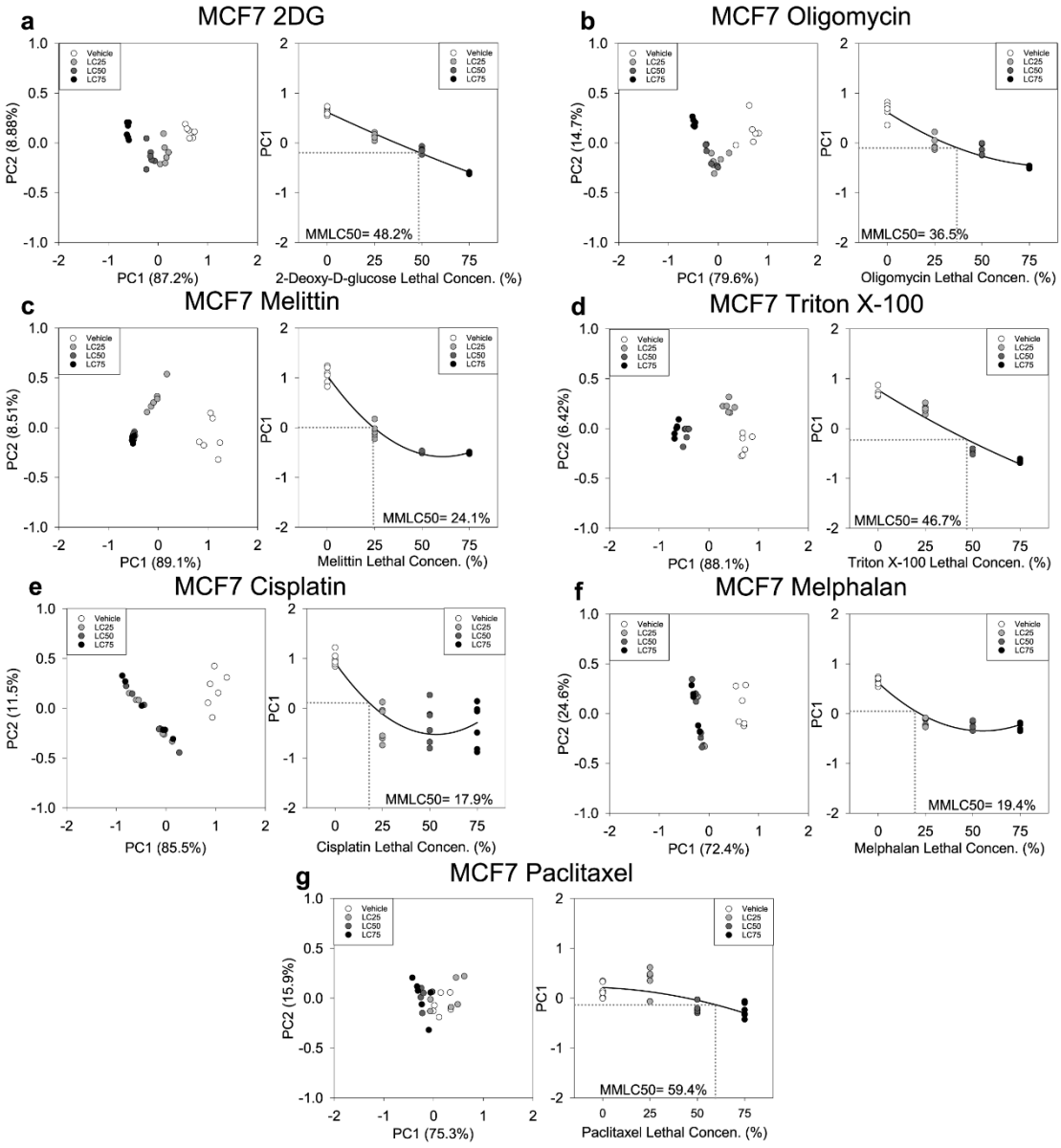

Figure 15. Principal component analysis (PCA) panel of MCF7 microtissues treated with various compounds. MCF7 multimodal data which contained results from four independent assays using previously determined lethal concentrations (LC) were transformed to two principal components (PC1 and PC2) using PCA. Scatterplots visualized the distribution of the data, and the percent of variance captured by each component was reported. PC1 data was also plotted as a function of lethal concentration, and a second order polynomial was fitted to the data (black lines). Multi-mechanisms LC_{50} (MMLC50) was calculated by taking two-thirds of the full data range and subtracting it from the vehicle control PC1 value, then projecting that value on the x axis (gray dotted lines). Each condition contained data from six replicates (n=3 datapoints per condition and two independent experiments). Published in Zein-Sabatto A., et al., 2025.

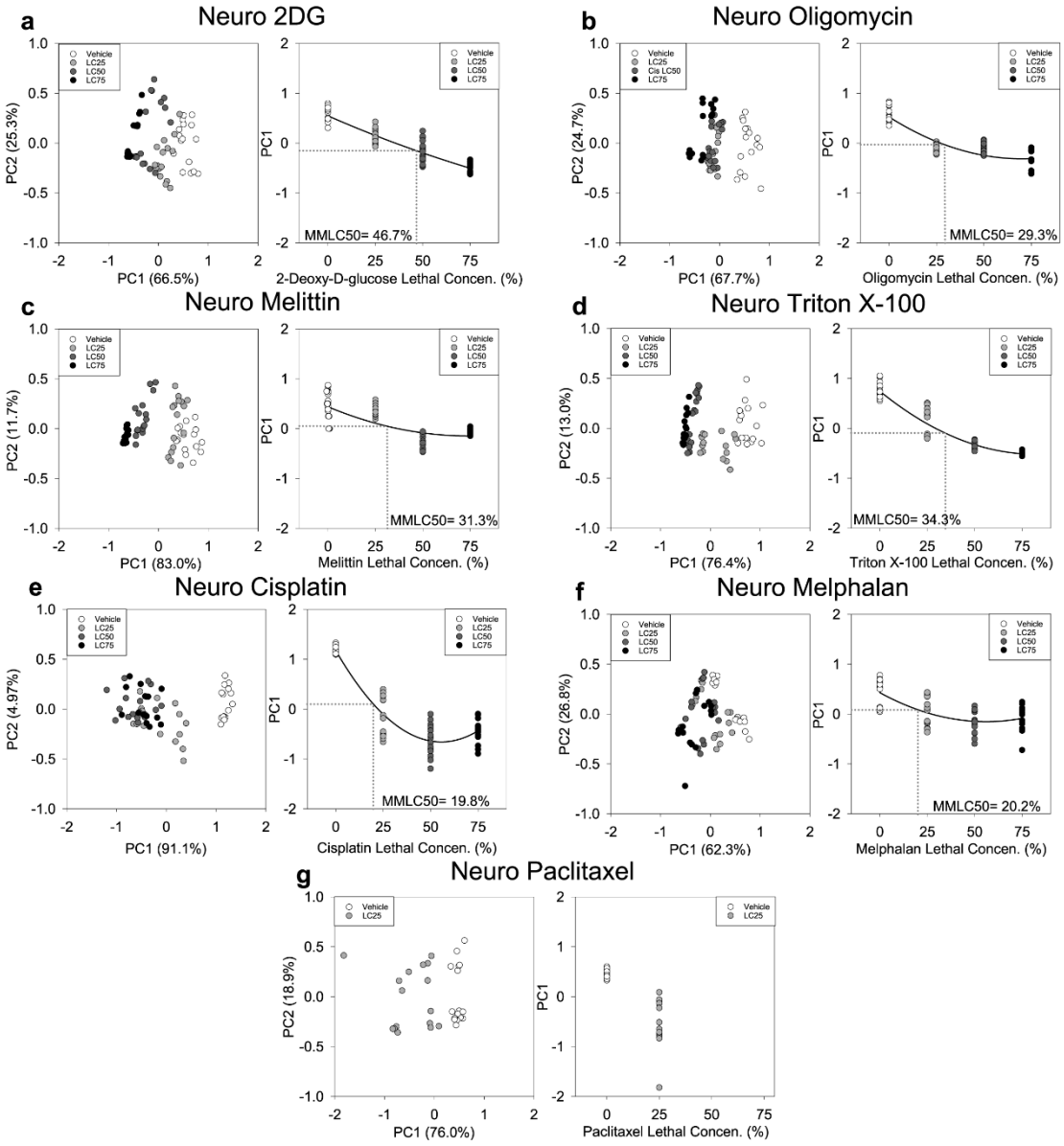

Figure 16. Principal component analysis (PCA) panel of neurospheroids treated with various compounds. Neurospheroid multimodal data which contained results from four independent assays using previously determined lethal concentrations (LC) were transformed to two principal components (PC1 and PC2) using PCA. Scatterplots visualized the distribution of the data, and the percent of variance captured by each component was reported. PC1 data was also plotted as a function of lethal concentration, and a second order polynomial was fitted to the data (black lines). Multi-mechanisms LC_{50} (MMLC50) was calculated by taking two-thirds of the full data range and subtracting it from the vehicle control PC1 value, then projecting that value on the x axis (gray dotted lines). Each condition contained 16 microtissues (n=8 microtissues per condition and two independent experiments). Published in Zein-Sabatto A., et al., 2025.

The eigenvalues, percent variance captured, and the results from the Bartlett's test of sphericity were also reported for PC1 from all PCA datasets (Table 2). PC1 successfully captured the majority of data variance across all datasets. The lowest and highest performances were from neurospheroid cultures treated with melphalan (62.3%) and cisplatin (91.1%), respectively (Table 2). Bartlett's test of sphericity revealed that all PCA dimension reductions were appropriate and statistically significant.

Table 2. Summary of eigenvalues, percentage of data variance captured, and chi-square results from the Bartlett's sphericity test for the first principal component were reported. Bartlett's test of sphericity confirms if principal component analysis dimension reduction was appropriate for any given dataset ($c^2 < 0.05$). Published in Zein-Sabatto A., et al., 2025.

Culture Type	Treatment	Eigenvalue	Percentage (%)	χ^2
HepG2	2DG	0.16	81.0	<0.0001
	Oligomycin A	0.31	90.6	<0.0001
	Triton X-100	0.36	72.0	<0.0001
	Melittin	0.18	65.0	<0.0001
	Cisplatin	0.33	77.3	<0.0001
	Melphalan	0.15	85.3	<0.0001
	Paclitaxel	0.14	83.7	<0.0001
MCF7	2DG	0.22	87.2	<0.0001
	Oligomycin A	0.19	79.6	<0.0001
	Triton X-100	0.34	88.1	<0.0001
	Melittin	0.43	89.1	<0.0001
	Cisplatin	0.45	85.5	<0.0001
	Melphalan	0.16	72.4	<0.0001
	Paclitaxel	0.09	75.3	<0.0001
Neurospheroid	2DG	0.18	66.5	<0.0001
	Oligomycin A	0.14	67.7	<0.0001
	Triton X-100	0.26	76.4	<0.0001
	Melittin	0.27	83.0	<0.0001
	Cisplatin	0.58	91.1	<0.0001
	Melphalan	0.14	62.3	<0.0001
	Paclitaxel	0.35	76.0	<0.0001

Finally, PCA loadings were calculated using Equation 9 and provided an alternative method to compare inter-assay responses and compound cytotoxicity (Fig. 17). Assays with loadings of greater magnitude are more correlated with PC1 while positive or negative values indicate whether the assay outputs were directly or inversely proportional to PC1, respectively. Overall, multiple assays contributed to PC1 across treatments and culture types with a few exceptions. Microtissue-treatment-assay combinations with loadings less than 0.25 included HepG2-melittin-EdU, MCF7-cisplatin-ATP, and Neurospheroid-paclitaxel-EdU (Fig. 17).

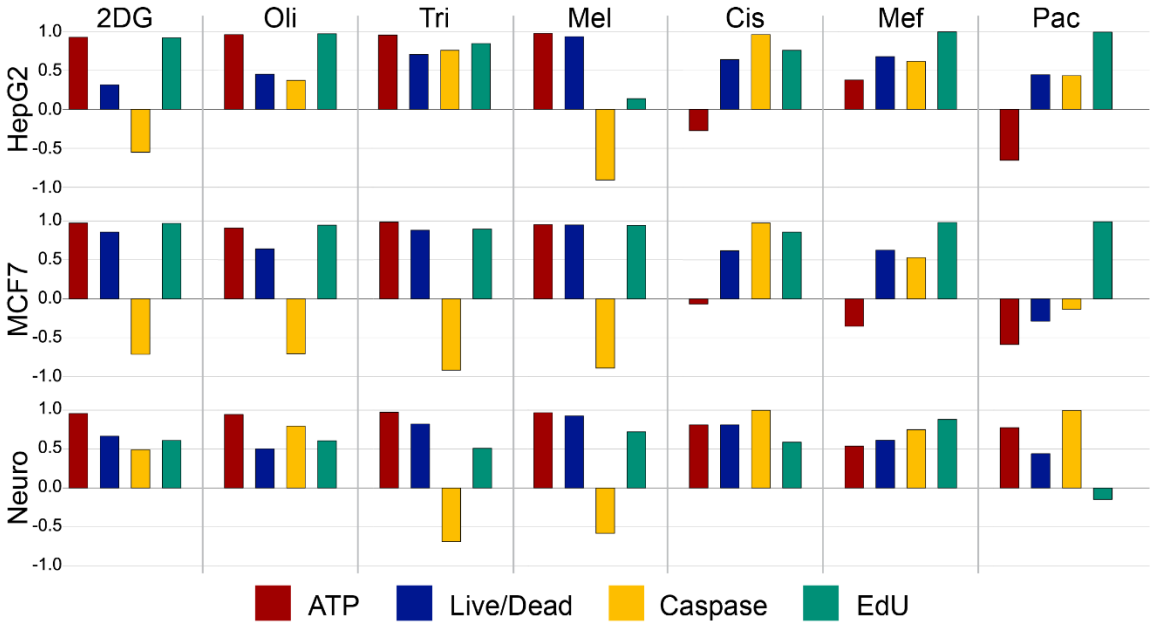

Figure 17. The loadings from the first principal component were reported for all conditions. Different colors represent the different assays used (red: CellTiter-Glo 3D, blue: Live/Dead, yellow: Caspase-Glo 3/7 3D, cyan: Click-iT EdU proliferation assay). 2DG: 2-Deoxy-D-glucose, Oli: oligomycin A, Tri: Triton X-100, Mel: melittin, Cis: cisplatin, Mef: melphalan, Pac: paclitaxel, Neuro: neurospheroid. Published in Zein-Sabatto A., et al., 2025.

3.4 Discussion

Traditional LC values provide limited information regarding the potency of a compound using a single biological perturbation. This vastly underestimates the overall viability since multiple pathways of cellular injury and death may occur simultaneously within a sample. Conducting muti-assay analysis is advantageous; however, direct statistical inferences cannot be made across different assays since conventional statistical tests evaluate each assay independently. To address this, we collected multimodal data from all combinations of seven treatments, four assays, and three tissue culture types. This provided an opportunity to observe the response of different assays to the same treatment conditions.

The steepness of the slopes derived from the LME model fits can be attributed to the response of each assay (Figs. 8-11). When summarized in Figure 12, we see that multiple assays responded significantly to the same treatment injury. This supported our hypothesis that single mechanisms of injury (e.g., inhibition of glycolysis) can manifest its negative effects on cell viability through multiple biomarkers. Both ATP and EdU assays responded to metabolic inhibition using 2DG and oligomycin A across all microtissues (red and cyan bars, Fig. 12). ATP and Live/Dead assays produced observable responses to membrane poration from Triton X-100 and melittin (red and blue bars, Fig. 12). Caspase and EdU assays responded to the alkylating agents cisplatin and melphalan (yellow and cyan bars, Fig. 12). Finally, EdU responded most significantly to microtubule disruption for HepG2 and MCF7 microtissues; meanwhile, ATP and caspase assays responded in the neurospheroids (red, yellow, and cyan bars, Fig. 12).

These findings were also reflected in the PCA loadings (Fig. 17). PCA is more robust against deviations in normality and homoscedasticity when sample sizes are sufficiently large.[34,35] The applicability of the PCA approach to analyzing multimodal data was also reflected by the simulation data, magnitudes of the loadings, and χ^2 values from the Bartlett's test (Figs. 13 and 17; Table 2). PCA loadings, unlike the discrete slopes extracted in Figure 12, correlated each assay to an arbitrary component that is dependent on input variables. In general, PC1 can be broadly associated with cell viability but should not be over interpreted. PCA loadings with smaller magnitudes indicated that a specific assay was not sensitive to the cytotoxic response elicited by a treatment for a given microtissue. For instance, HepG2 microtissues treated with cisplatin had a decreased ATP assay loading response compared to the other three assays which highlighted the lower sensitivity of the ATP assay (Fig. 17). This can be confirmed by cross-referencing the loadings with the slopes from the LME regressions (Figs. 8-12). The convergence of both statistical approaches to the same analytical outcomes was promising. The practical implementation of this approach may involve researchers using an exclusion threshold on the magnitudes of the slopes and PCA loadings to identify the mechanistic pathways of cell death within a sample. Assays that do not respond or capture the data variance suggest insignificant contribution to overall viability. This approach also identified the assays, and therefore the biological perturbations, that are driving the cytotoxic response. Using this approach, we were able to evaluate the robustness of our hypothetical "best fit" assay-treatment combinations. In some instances, the "best fit" assay-treatment combinations were outperformed by a secondary assay tested. This may suggest that the secondary assay output was more sensitive to the biological disruption, or the treatment elicited a greater

change to the secondary biomarker. These assumptions were difficult to decouple since the assay outputs were collected using different methods (i.e., luminescence plate reader and fluorescence microscopy). Furthermore, the caspase data was normalized using a different approach for both LME and PCA methods. Future implementations of this approach may benefit from utilizing identical data collection and processing methods to minimize inherent data bias.

Interestingly, HepG2 microtissues treated with oligomycin A produced a steep LME regression slope despite HepG2 resistance to oligomycin treatment (Fig. 8). One method to help prevent conflating the large assay response with treatment potency may involve plotting the LME regression as a function of actual molar concentration instead of percent LC. This would incorporate the effects of potency on the overall slope; however, it may impact the linearity and goodness of fit of the regression analysis.

Longitudinal data collected after 12, 24, and 48 hours of exposure to paclitaxel in MCF7 microtissues revealed highly "noisy" data from the ATP and caspase assays, low sensitivity from the Live/Dead assay, and increasing EdU assay sensitivity with exposure time (App. A2). These findings confirm the critical contribution exposure time has on dose-response curves and its impact on the multimodal data analysis. Future studies may consider optimizing temporal factors in their experimental design and should only interpret their results within the context of the time courses tested.

Thus far, we have shown that multi-assay approaches help capture different mechanisms of cellular injury, and their results can be intuitively analyzed using LME and PCA. The $MMLC_{50}$ is an additional method to analyze multi-assay data. Since the

$MMLC_{50}$ is derived from PCA, input assays that carry the most variance will drive the data's fit (Fig. 13). The presence of input data with large margins of error, as was observed in the ATP and caspase assay data from the longitudinal dataset, may cause significant deviations in $MMLC_{50}$ (App. A2). Similarly, if an input dose-response curve with a sufficient change in output plateaus at a smaller lethal concentration (i.e., assay output reaches its maximal effect at a lower dose than the "best fit" assay-treatment pair), then the PC1 fit is significantly impacted. This is observed by a leftward shift in $MMLC_{50}$ relative to the LC_{50} indicating that there may exist a more sensitive assay that detects changes to viability at a lower dose (Fig. 13). For example, Triton X-100 treatment in HepG2 microtissues not only changed Live/Dead output as expected (blue bar, Fig. 12) but also resulted in plateaus in ATP and EdU assays (Figs. 8 and 11). As a result, the plateauing effect from the ATP and EdU assays caused the leftward shift in $MMLC_{50}$ (Fig. 14). A $MMLC_{50}$ closer to the LC_{50} suggested that the compound caused disruption to at least one assay, and it potentially affected other assay outputs to a similar or lesser degree. Under such circumstances, PCA loadings can be used to identify whether multiple injury mechanisms occurred simultaneously. For example, HepG2 microtissues treated with melittin had a $MMLC_{50}$ of 49.8% which equated to 5.5 μM compared to the LC_{50} of 5.6 μM (Fig. 14, App. A1). Despite this, LME regression slopes and PCA loadings revealed that ATP, Live/Dead, and caspase outputs responded significantly (Figs. 12 and 17). Finally, if an input dose-response curve with a sufficient change in output maintains a plateau at lower doses followed by a sudden steep change (i.e., assay output only begins to change at a higher dose than the initial "best fit" assay-treatment pair), then the $MMLC_{50}$ is also affected. This is observed by a rightward shift in $MMLC_{50}$ relative to the LC_{50} which may

suggest the presence of a more sensitive assay; however, the cellular injury captured by this assay requires a higher treatment dose to manifest. As previously mentioned, outputs from assays that have large variances but do not respond significantly to dose can be incorrectly analyzed by PCA $MMLC_{50}$ as a change in viability. One potential occurrence of this scenario involves MCF7 microtissues treated with paclitaxel which observed a rightward shift in $MMLC_{50}$ (Fig. 15). Despite this shift, LME regression fits and PCA loadings confirm that the EdU proliferation assay was the most sensitive assay (Figs. 8-12 and 17).

Finally, this study aimed to incorporate a multimodal approach using experimental designs that are applicable to HTS studies. Technological advances in automation, culturing techniques, and analytical tools are improving the accessibility of HTS studies and their implementation in various fields. The platform used in this study utilized self-aggregating microtissues that reliably created 3D spheroids in 96-microwell arrays using cells from diverse origins. Other low-adhesion, multi-well plate formats have also become commercially available. Regardless of the selected platform, 3D cultures form reproducible samples that more closely recapitulate the *in vivo* microenvironment and maintain the clinical relevance of the model. These samples are often used in conjunction with simple, "add-mix-measure" assays for cost-effective outputs that are easily scalable for HTS studies. The analytical approaches demonstrated in this study, based on LME and PCA, can be readily applied to larger studies; furthermore, their outputs enable the quantifiable assessment of multi-assay responses in an intuitive and comprehensive manner. This will allow researchers to reveal complex, multifaceted pathways of cytotoxicity that may be overlooked by single assay analysis. For example, the multimodal approach may reveal

unanticipated mechanistic effects of drugs leading to more accurate pharmacological and toxicological profiling. This can enhance the clinical translatability of a study and reduce late-stage failures during novel drug development. Similarly, shifts in $MMLC_{50}$ could be leveraged to identify which assays, and therefore which cellular perturbations, could be optimized in a study. $MMLC_{50}$ metrics could also serve as more representative measures of lethality for pharmacological agents *in vitro*. LCs from *in vivo* studies measure potency of a drug by determining the probability that a treatment will induce death in an organism, whereas, researchers and industry may require more detailed information regarding the type of death a cell experiences after treatment. This information can be provided by multimodal approaches like the $MMLC_{50}$. The proposed analytical framework could also be implemented in a FPM-HTS study using patient-derived tumor cultures to help select patient-specific therapies. Both LME and PCA outputs are capable of distinguishing between compound treatment effectiveness; therefore, they can effectively eliminate nonresponsive treatments from a larger screen.

3.5 Conclusion

The overall goal of this aim was to collect and analyze multi-assay data. Every combination of microtissue culture, treatment, and assay was tested using previously determined LCs to produce the multimodal dataset. We proposed the implementation of two multivariate statistical approaches including LME regression fits and PCA to extract relevant information regarding multiple mechanisms of cellular injury. Both approaches provided quantifiable assessments of inter- and intra-assay responses to various treatments through LME regressions slopes, PCA loadings, and the newly developed $MMLC_{50}$ metric.

Ultimately, the proposed approach will allow researchers to answer hypothesis driven questions stemming from multimodal cytotoxicity data that could not be previously accomplished using standard approaches. Furthermore, the multi-assay data collected here was crucial for the next aim which required the correlation of OCT data to “gold standard” assays.

3.5 References

1. Xu, H. *et al.* Crosstalk of cell death pathways unveils an autophagy-related gene AOC3 as a critical prognostic marker in colorectal cancer. *Commun. Biol.* **7**, 1–12 (2024).

2. Lee, P. *et al.* Fas pathway is a critical mediator of cardiac myocyte death and MI during ischemia-reperfusion in vivo. *Am. J. Physiol.-Heart Circ. Physiol.* **284**, H456–H463 (2003).

3. Whelan, R. S. *et al.* Bax regulates primary necrosis through mitochondrial dynamics. *Proc. Natl. Acad. Sci.* **109**, 6566–6571 (2012).

4. Hamacher-Brady, A., Brady, N. R. & Gottlieb, R. A. Enhancing Macroautophagy Protects against Ischemia/Reperfusion Injury in Cardiac Myocytes *. *J. Biol. Chem.* **281**, 29776–29787 (2006).

5. Brokaw, D. L. *et al.* Cell Death and Survival Pathways in Alzheimer's Disease: An Integrative Hypothesis Testing Approach Utilizing -Omic Datasets. *Neurobiol. Aging* **95**, 15–25 (2020).

6. Crighton, D. *et al.* DRAM, a p53-Induced Modulator of Autophagy, Is Critical for Apoptosis. *Cell* **126**, 121–134 (2006).

7. Bock, F. J. & Tait, S. W. G. Mitochondria as multifaceted regulators of cell death. *Nat. Rev. Mol. Cell Biol.* **21**, 85–100 (2020).

8. Bonora, M., Giorgi, C. & Pinton, P. Molecular mechanisms and consequences of mitochondrial permeability transition. *Nat. Rev. Mol. Cell Biol.* **23**, 266–285 (2022).

9. Eguchi, Y., Shimizu, S. & Tsujimoto, Y. Intracellular ATP Levels Determine Cell Death Fate by Apoptosis or Necrosis1. *Cancer Res.* **57**, 1835–1840 (1997).

10. Nomura, M., Ueno, A., Saga, K., Fukuzawa, M. & Kaneda, Y. Accumulation of Cytosolic Calcium Induces Necroptotic Cell Death in Human Neuroblastoma. *Cancer Res.* **74**, 1056–1066 (2014).

11. Sun, W. *et al.* Cytosolic calcium mediates RIP1/RIP3 complex-dependent necroptosis through JNK activation and mitochondrial ROS production in human colon cancer cells. *Free Radic. Biol. Med.* **108**, 433–444 (2017).

12. Zhang, T. *et al.* CaMKII is a RIP3 substrate mediating ischemia- and oxidative stress–induced myocardial necroptosis. *Nat. Med.* **22**, 175–182 (2016).

13. He, R. *et al.* Mechanisms and cross-talk of regulated cell death and their epigenetic modifications in tumor progression. *Mol. Cancer* **23**, 267 (2024).

14. Li, X. *et al.* Caspase-8 auto-cleavage regulates programmed cell death and collaborates with RIPK3/MLKL to prevent lymphopenia. *Cell Death Differ.* **29**, 1500–1512 (2022).

15. Yu, L. *et al.* Regulation of an ATG7-beclin 1 Program of Autophagic Cell Death by Caspase-8. *Science* **304**, 1500–1502 (2004).

16. Lin, Y., Devin, A., Rodriguez, Y. & Liu, Z. Cleavage of the death domain kinase RIP by Caspase-8 prompts TNF-induced apoptosis. *Genes Dev.* **13**, 2514–2526 (1999).

17. O'Donnell, M. A. *et al.* Caspase 8 inhibits programmed necrosis by processing CYLD. *Nat. Cell Biol.* **13**, 1437–1442 (2011).

18. Feng, S. *et al.* Cleavage of RIP3 inactivates its caspase-independent apoptosis pathway by removal of kinase domain. *Cell. Signal.* **19**, 2056–2067 (2007).

19. Han, J.-H., Park, J., Kang, T.-B. & Lee, K.-H. Regulation of Caspase-8 Activity at the Crossroads of Pro-Inflammation and Anti-Inflammation. *Int. J. Mol. Sci.* **22**, 3318 (2021).

20. Brown, J. M. & Attardi, L. D. The role of apoptosis in cancer development and treatment response. *Nat. Rev. Cancer* **5**, 231–237 (2005).

21. Abend, M. Reasons to reconsider the significance of apoptosis for cancer therapy. *Int. J. Radiat. Biol.* **79**, 927–941 (2003).

22. Yang, S. *et al.* Crosstalk between metabolism and cell death in tumorigenesis. *Mol. Cancer* **23**, 71 (2024).

23. Sancho-Martínez, S. M., Piedrafita, F. J., Cannata-Andía, J. B., López-Novoa, J. M. & López-Hernández, F. J. Necrotic Concentrations of Cisplatin Activate the Apoptotic Machinery but Inhibit Effector Caspases and Interfere with the Execution of Apoptosis. *Toxicol. Sci.* **122**, 73–85 (2011).

24. Ullén, A. *et al.* Sorafenib induces apoptosis and autophagy in prostate cancer cells in vitro. *Int. J. Oncol.* **37**, 15–20 (2010).

25. Khing, T. M. *et al.* The effect of paclitaxel on apoptosis, autophagy and mitotic catastrophe in AGS cells. *Sci. Rep.* **11**, 23490 (2021).

26. Eom, Y.-W. *et al.* Two distinct modes of cell death induced by doxorubicin: apoptosis and cell death through mitotic catastrophe accompanied by senescence-like phenotype. *Oncogene* **24**, 4765–4777 (2005).

27. Malo, N., Hanley, J. A., Cerquozzi, S., Pelletier, J. & Nadon, R. Statistical practice in high-throughput screening data analysis. *Nat. Biotechnol.* **24**, 167–175 (2006).

28. Bradley, J. V. The complexity of nonrobustness effects. *Bull. Psychon. Soc.* **22**, 250–253 (1984).

29. Lix, L. M., Keselman, J. C. & Keselman, H. J. Consequences of Assumption Violations Revisited: A Quantitative Review of Alternatives to the One-Way Analysis of Variance F Test. *Rev. Educ. Res.* **66**, 579–619 (1996).

30. Linear Mixed-Effects Models: Basic Concepts and Examples. in *Mixed-Effects Models in Sand S-PLUS* (eds. Pinheiro, J. C. & Bates, D. M.) 3–56 (Springer, New York, NY, 2000). doi:10.1007/978-1-4419-0318-1_1.

31. Gałecki, A. & Burzykowski, T. Linear Mixed-Effects Model. in *Linear Mixed-Effects Models Using R: A Step-by-Step Approach* (eds. Gałecki, A. & Burzykowski, T.) 245–273 (Springer, New York, NY, 2013). doi:10.1007/978-1-4614-3900-4_13.

32. Jolliffe, I. T. & Cadima, J. Principal component analysis: a review and recent developments. *Philos. Transact. A Math. Phys. Eng. Sci.* **374**, 20150202 (2016).

33. Abdi, H. & Williams, L. J. Principal component analysis. *WIREs Comput. Stat.* **2**, 433–459 (2010).

34. Hong, D., Balzano, L. & Fessler, J. A. Asymptotic performance of PCA for high-dimensional heteroscedastic data. *J. Multivar. Anal.* **167**, 435–452 (2018).

35. Bispo, R. & Marques, F. Stability of principal components under normal and non-normal parent populations and different covariance structures scenarios. *J. Stat. Comput. Simul.* **93**, 1060–1076 (2023).

CHAPTER 4: OPTICAL COHERENCE TOMOGRAPHY VIABILITY IMAGING & MODELING

4.1 Introduction

4.1.1 Optical Coherence Tomography

Optical coherence tomography (OCT) is a noninvasive and label-free imaging modality that utilizes low-coherence interferometry to generate cross-sectional images of a sample.[1] The OCT signal originates from a low coherence light source, such as a superluminescent diode, which is split into the sample and reference arms. Light traveling through the reference arm is reflected off a mirror and redirected to a detector. The light traveling through the sample arm interacts with a specimen, and the backscattered light travels back to the same detector. The light from both arms interacts at the detector to create an interference pattern which creates the OCT signal. Due to the low coherence properties of the source light, the OCT signal rapidly deteriorates when the light between the two arms are mismatched.[1] This feature of OCT provides optical sectioning capabilities, similar to a pinhole found in confocal microscopes, and is influenced by the coherence length of the light source.[1] OCT's axial resolution is determined by the coherence length of light,

while the lateral resolution is determined by the objective lens. Traditional OCT systems relied on scanning the reference mirror position and simultaneously recording the amplitude of the interferometric signal to produce 3D images; however, spectral domain OCT (SD-OCT) synchronously obtains a depth-resolved signal without the need for depth scanning.[2] As a result, SD-OCT utilizes a fixed reference arm that is positioned at the appropriate distance relative to the image's focal plane, and multiple line scans (i.e., B-scan) collect spectral interference data from the sample.[2,3] A Fourier transform is then used to reconstruct the depth-encoded spectral OCT signal collected by the spectrometer for every x-y position (i.e., A-scan).[2,3] Figure 18 describes a typical SD-OCT system setup and data extraction.[3] Overall, this improves SD-OCT image acquisition time by a factor of 50 or more without losing sensitivity.[2] OCT has been used for a variety of clinical applications including ophthalmology, dermatology, and oncology.[4–6]

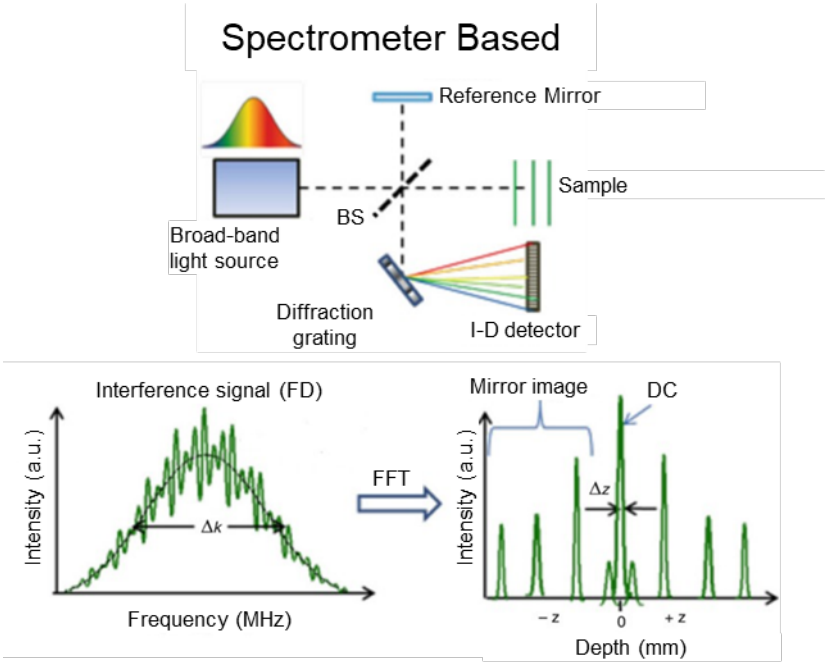

Figure 18. The optical setup of the spectral domain OCT system can be seen in the top panel. Light from a broad-band light source is split into a reference and sample arm. The light's spectral properties are then measured using a diffractive element and spectrometer. The spectral interference signal is then reconstructed into an A-scan using a Fourier transform. Adapted from Aumann S., et al., 2019.

4.1.2 OCT Viability Imaging for FPM

OCT imaging provides a promising approach for measuring cell viability in high-throughput applications like functional precision medicine (FPM). Unlike traditional assays, OCT does not require the addition of exogenous reagents or dyes to produce a signal. This allows OCT to overcome many challenges associated with current "gold standard" assays including reagent cytotoxicity, diffusion/penetration limitations, and photobleaching. As a result, OCT can provide truly longitudinal measurements from the same sample. This is particularly advantageous for FPM since patient biopsy sizes can be limited.[7,8] Longitudinal assessments of viability from the same samples may also reveal important temporal dynamics including the gradual development of chemoresistance in patient tumors. If a patient begins to experience chemoresistance, a doctor could utilize the FPM-OCT screen to empirically test the efficacy of multiple second-line therapies in parallel and determine which therapeutic intervention should be administered to the patient. Another advantage of OCT imaging involves its millimeter penetration depth.[9] This enables the OCT imaging system to provide assessments of viability throughout the 3D culture; moreover, it provides spatially relevant information regarding the effects of nutrient gradients and metabolic zones on treatment efficacy. Extracting viability information from the entire 3D culture provides additional safeguards against sampling bias and collecting information from surface regions alone. Finally, many metrics can be extracted from OCT viability imaging. Previous studies have investigated the effects of cell death on multiple OCT metrics; however, more experiments are needed to validate the biological mechanisms associated with the changes in OCT metrics. If successful, the

multimodal outputs from OCT imaging may predict various biological pathways of cell death.

Current state-of-the-art, high-content screening systems involve widefield fluorescence or confocal imaging. We compared a study conducted by Sirenko et al. which utilized multiparametric assessments of viability to our proposed OCT HTS experimental design. The study analyzed the cytotoxic effects of 54 compounds using confocal imaging and standard assays using ethidium homodimer and calcein AM staining (similar to the Live/Dead assay), CellEvent Caspase 3/7 assay (similar to the Caspase-Glo 3/7 3D), and a mitochondrial toxicity assay MitoTracker Orange.[10] For fluorescence imaging, the confocal microscope was used to capture the bottom 100-120 μm region of the spheroids, and images were converted to 2D projections. OCT viability imaging, if successfully implemented, would provide substantial improvements to data collection and throughput to the study design. First, the study conducted each assay independently which substantially increased the sample size and resources required for completion. OCT multi-metric outputs would potentially extract all relevant cytotoxicity data from multiple cell death pathways using the same sample. OCT would also circumvent the need to purchase, incubate, and store multiple assay reagents. This has nontrivial impacts when scalability is required, and resource demands become more critical. Second, the Sirenko et al. study acquired Z-stack images from 100-120 μm depths which would have excluded relevant data from the spheroids' deeper regions, whereas OCT imaging would be able to completely resolve the 3D tissue. The data from 3D images was further processed into 2D projections which eliminated any spatially relevant information. Meanwhile, analysis on 3D OCT images may provide an opportunity to study region-specific changes to all metrics.

Overall, OCT-based HTS approaches overcome many technological and logistical challenges that affect conventional fluorescence imaging systems.

4.1.3 OCT Metrics

For this aim, we developed and validated the response from 77 OCT metrics and their derivates. The goal was to correlate the change in relevant OCT metrics to four "gold standard" assays. This would allow us to generate a prediction model from the OCT metrics that could then be used to quantify changes to cellular viability. The proposed framework provided a proof-of-concept example, but it will require future iterations and refinements to improve its accuracy and feasibility. A detailed list of OCT metrics used in the study can be referenced in the *Appendix* (App. A3).

Spheroid Geometry

The effect of cell viability on culture geometry has been reported from multiple studies that revealed dose-dependent changes to spheroid sphericity and bulk morphology with increased cell death.[11,12] Measurements pertaining to spheroid geometry can be derived from the 3D binarized images extracted from OCT. Volume, surface area, the ratio between surface area and volume, and the sphericity of spheroids were extrapolated from binarized 3D OCT images. It was hypothesized that spheroid geometry would be most sensitive to changes in cell morphology. Cellular swelling due to necrotic or necroptotic cell death and cytoplasmic condensation due to apoptosis have the potential to make the overall spheroid size increase or decrease, respectively. Unhealthy cells may also lose their ability to maintain cell-cell adhesions which could result in the disaggregation of a spheroid and increase its perceived volume.

Intensity and Decorrelation

Backscattered light intensity is the fundamental output from OCT imaging which provides information regarding the reflectivity of the sample. Previous studies have identified that intracellular organelles including the mitochondria and nuclei contribute significantly to the optical scattering properties of cells.[13–16] The involvement of mitochondrial disruption to multiple cell death pathways through outer membrane permeabilization and transition pore formation may highlight its ability to change the overall scattering profile of cells following injury. Similarly, apoptotic condensation of DNA could produce changes in scattering profiles. Intensity amplitude and area under the curve was shown to significantly change in myeloid leukemia cell pellets treated with cisplatin, colchicine, and growth factor withdrawal.[17] Intensity metrics can be further analyzed by measuring time-dependent changes in signal fluctuations. These metrics include speckle variation, signal decorrelation, and standard deviation of the intensity signal. Multiple studies have reported dose-dependent changes to intensity fluctuations across multiple tissue culture types and treatments.[18–21]

Optical Scattering Attenuation

It is well established that 3D cultures generate nutrient gradients along their depths; therefore, spatial differences in viability may exist in larger tissues.[22,23] The optical attenuation coefficient is a metric that measures depth-dependent changes to the light scattering properties of the tissue. Changes in cellular morphology, organelle light scattering, and cell density may be detected through changes to the scattering coefficient. Notably, a previous study found that the scattering attenuation increased in the presence of

the necrotic core.[24] However, another study found that necrotic cell death induced by ethanol treatment resulted in a decrease in average attenuation, while apoptosis induced by colchicine treatment resulted in an initial increase then decrease in attenuation as secondary necrosis began to manifest.[25] Furthermore, previous work in our lab has led to the development of improved attenuation coefficient metrics that increase overall accuracy to 99% from 65% compared to traditional calculation methods.[26] Both traditional and depth-resolved attenuation coefficient metrics were included in this study.

Dynamic Light Scattering Metrics

Many OCT metrics, including the ones described above, may vary in their reproducibility due to inherent differences across OCT systems and fluctuations in signal strength.[27–29] The diffusion coefficient has been introduced as a robust metric for the measurement of intracellular motility. Dynamic light scattering OCT (DLS-OCT) image processing involves applying the autocorrelation function to the OCT signal to quantify the translational and diffusive motions of particles within a voxel. This approach enables the creation of 3D maps which provides visual information regarding the motion of particles in standard units of $\mu m^2/s$.[30] DLS-OCT extracts other informative metrics including the ratio of static, entering, and exiting particles. The ability to model different particle dynamics simultaneously ensures that the diffusion coefficient can be measured reliably in a voxel with mixed dynamics. DLS-OCT does not require normalization and metrics that are calculated in standard units of $\mu m^2/s$ can be compared directly across imaging systems.

4.1.4 OCT Viability Prediction Models

The goal of the third aim was to characterize the OCT metrics and correlate them to "gold standard" viability assays. OCT metrics that were highly correlated with assay outputs were expected to share sensitivity to the same cellular injury. For example, OCT metrics that were highly correlated with the CellTiter-Glo 3D assay output were expected to predict changes to the metabolic health of cells. Similarly, OCT metrics that were correlated with the Live/Dead, Caspase-Glo 3/7 3D, and Click-iT EdU assays were expected to predict changes to membrane integrity, apoptosis, and proliferation, respectively. As a proof-of-concept, a subset of OCT and assay data was analyzed to create a prediction model. The analytical framework proposed here can be readily scaled to all datasets for in-depth data interpretation. In brief, pairwise correlations between OCT metrics and assay outputs were assessed using simple linear regressions. Linear regressions provided a relatively easy and interpretable approach to identify which OCT metrics were best suited for predicting assay outcomes. OCT metrics with statistically significant regressions were passed to the next analytical step which involved structural equation modeling (SEM).

SEM is a multivariate approach that combines features from factor analysis and multiple regressions into a single framework that is visually interpretable.[31] SEM tests *a priori* assumptions regarding the relationship between manifest and latent variables. Manifest variables as experimentally observed datasets (i.e., assay and OCT metrics) while latent variables correspond to hypothetical constructs or explanatory factors that cannot be directly measured.[32] A key assumption for the implementation of SEM involved defining

cell viability as a complex construct with no single, definitive measurement. SEM was then implemented to generate a model by fitting and subsequently trimming nonsignificant pathways. The ultimate goal was to generate a final model that is theoretically sound, reasonably parsimonious, and fits the corresponding data.[32] A path diagram representing a SEM measurement model can be seen in Figure 19. SEM models that follow this structure can be modeled mathematically using Equation 10

$$\text{Equation 10} \quad \boldsymbol{x} = \tau_{\boldsymbol{x}} + \boldsymbol{\Lambda}_{\boldsymbol{x}}\xi + \delta$$

where **x** is the vector of x variables (x_1, x_2, x_3), $\tau_{\mathbf{x}}$ is the vector of intercepts for each x variable, $\boldsymbol{\Lambda}_{\mathbf{x}}$ is the matrix of loadings corresponding to the latent variable (λ_1, λ_2, λ_3), ξ is the latent variable, δ is the vector of residual errors (δ_1 δ_2 δ_3). In Figure 10, the variances are shown as θ_i for the x variables and ϕ_i for the latent variable.

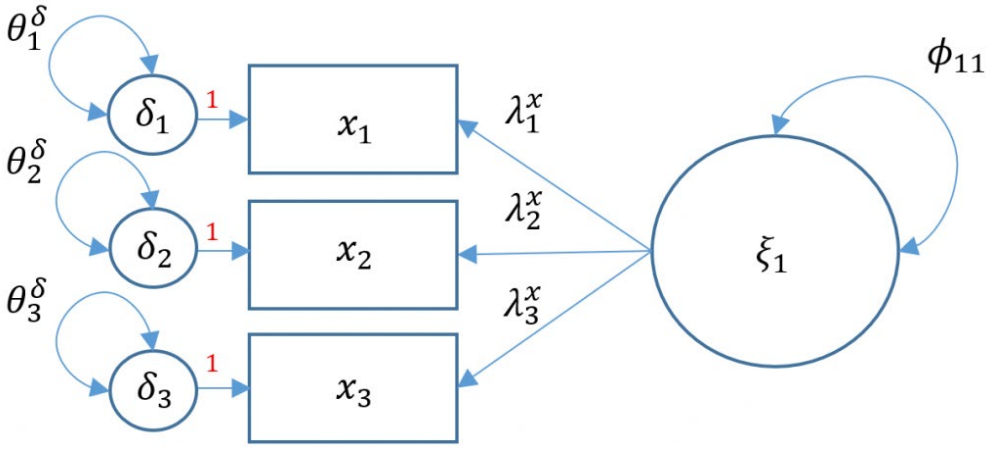

Figure 19. An example structural equation model path diagram with mixed manifest variables (shown in rectangles) and latent variable (shown in circles). Unidirectional arrows signify a causal path while bidirectional arrows represent variance. The ξ represents the exogenous latent variable that affects the manifest variables (x_1, x_2, x_3). The δ terms represent the residual error of the manifest variables. The θ and ϕ terms represent the variance of each manifest and latent variable, respectively. Adapted from UCLA: Statistical Consulting Group.

4.2 Methods

4.2.1 Cell Culture and Three-Dimensional Microtissue Formation

For the purposes of this study, only HepG2 microtissues were analyzed. Detailed methods and protocols used to culture, passage, and maintain the HepG2 microtissues were provided in *Section 2.2.1: Cell Culture*. Methods describing the generation of the agarose 96-microwell arrays and the seeding of the three-dimensional microtissues were provided in *Section 2.2.2: Three-Dimensional Microtissue Culture.*

4.2.2 Compound Treatment

Treatment stock and working solutions were generated using similar methods described in detail in *Section 2.2.3: Compound Treatment*; however, serial dilutions were not implemented to induce cellular perturbations for this study aim. Instead, the precalculated lethal concentrations (LCs) that elicited 25, 50, and 75 percent cell death from the "best fit" assay-treatment pairs were utilized for OCT imaging. In some instances, LC values could not be achieved using predetermined solubility and media displacement guidelines described in a previous chapter. Treatment LCs that were unachievable were excluded from the study. A summary table of all LCs used in this aim can be referenced in the *Appendix* (App. A1). All treatments involved 24 hours of exposure prior to OCT imaging.

4.2.3 "Gold Standard" Assay Data

All multi-assay data used in this aim were generated from experiments described in the previous chapter. Detailed methods explaining the assay protocols and image analysis used to extract all assay outputs were provided in *Sections 2.2.4* through *2.2.8*.

4.2.4 Optical Coherence Tomography Imaging

Optical Coherence Tomography System

All OCT imaging was acquired using a commercially available Telesto III SD-OCT system (Thorlabs). Custom LabVIEW software was used to control the OCT system. A near-infrared, noncoherent superluminescent diode with a center wavelength of 1310 nm and bandwidth of 170 nm was used as the light source. The coherence length of the light enabled a high axial resolution of 3.5 μm in air. The SD-OCT system was coupled with a widefield objective lens with a spot size of ~20 μm (LSM03, Thorlabs) and a 2048-pixel line-scan camera capable of 147,000 A-scans/s. Agarose microwell arrays containing the microtissues were placed in glass-bottom, 24-well plates (P24-1.5H-N, Cellvis) with 1 mL of media prior to imaging. To maintain homeostatic conditions while imaging, the well plate was placed inside a custom miniature incubator that maintained 37°C and 5% CO_2. The custom incubator was secured above the OCT probe, and the microtissues were imaged from the bottom-up through a window in the custom incubator.

Imaging Protocols

A total of three image acquisitions were collected for each condition. The first involved acquiring the DLS-OCT data metrics. DLS scanning protocols required fast

acquisition rates which were achieved by repetitive B-scans centered over the imaging field of view. A 128 x-pixel line scan was repetitively acquired 256 times with a speed of ~3.5 ms per scan. This scan was repeated for 256 y-positions with a pixel size of 10 μm. Due to the size constraints needed to maintain imaging speed, approximately 10 microtissues were captured per image. The second scan was acquired using a larger field of view which covered 512 x 512 x 512 pixels (x,y,z) with a lateral pixel size of 10 μm. A total of four B-scans were captured with a rate of 10 ms per scan. A total of four image volumes were acquired and later used for volume averaging. This scanning protocol captured 50-60 microtissues per image. A third and final scan was acquired using identical parameters from the second scan except that the focal plane was axially translated by 100 μm. This was necessary for the derivation of the confocal-corrected scattering attenuation coefficient described in Stefan et al., 2018.

Image Processing and Metric Extraction

OCT image reconstruction was accomplished using custom MATLAB (MathWorks) software. Image enhancements such as median filtering, motion correction, dispersion compensation, interpolation, and volume averaging were utilized to improve overall image quality and resolution. First, individual microtissues were segmented using a semi-automated processing pipeline. In brief, the reconstructed grayscale intensity maps were binarized and image artifacts were removed based on size and morphology. Individual microtissues were segmented and selected for further analysis. Geometric parameters were extracted from the binarized images. The volume of a microtissue could be determined by summing all voxels within the microtissue and multiplying by the volume of one voxel. Similarly, the surface area of a microtissue could be determined by extrapolating the edge

voxel count to total surface pixels and multiplying by the area of one pixel. Since microtissues assumed spherical structures, the AVR was calculated as the ratio between the surface area and volume of a sphere. The surface roughness (SR), or sphericity, is a better metric that adjusts for changes in spheroid size and was calculated by Equation 11

$$\text{Equation 11} \quad SR \equiv (SA/4\pi)^{1/2}/(3V/4\pi)^{1/3}$$

where SR is the surface roughness, SA is the surface area, and V is the volume of the microtissue. Values closer to 1.0 signify a perfectly smooth sphere, and larger values indicate a rougher surface. Intensity metrics were extracted from the interference spectrum from both sample and reference arms at the spectrometer. The time-dependent intensity component of the signal was isolated, and an inverse Fourier transform was used to determine the complex-valued field reflectivity. Finally, the absolute value of the squared field reflectivity was used to obtain the final intensity measurement for each voxel. The decorrelation was derived from the field reflectivity equation using two time points (e.g., 10 ms) in Equation 12

$$\text{Equation 12} \quad D \equiv \left|\tilde{R}(t_0 + \Delta t) - \tilde{R}(t_0)\right|^2$$

where D is the decorrelation, $\tilde{R}$ is the field reflectivity as a function of time (t). Decorrelation is a relative metric that is dependent on the intensity of the image; therefore, we decoupled the two by calculating the normalized decorrelation using Equation 13

$$\text{Equation 13} \quad D_{norm}^{p} \equiv \frac{D}{I^p}$$

where D_{norm} is the power-normalized decorrelation, D is the raw decorrelation, and I is the intensity raised to the power p (values of p ranged from 1-4). Additional metrics were

extracted from fitting the data to the autocorrelation function and included the decay, absolute value of the doppler-derived particle motion, complex shift, noise-adjusted decay, and noise-adjusted complex shift (App. A3). The optical attenuation coefficient (OAC) was extracted following methods described in another study.[33] Confocal-corrected OAC was derived using methods explained in Sabina et al.[26] Depth-resolved OAC measured the change in attenuation at each voxel using different methods developed by computer simulation (data not shown). Data from the DLS-OCT scanning protocols was processed using methods described in more detail in Lee et al.[30] In brief, the autocorrelation function can be modeled to extract the ratio of static, flowing, and exiting particles in a voxel. In addition, the diffusion coefficient can be extracted as a robust metric of particle motions within a voxel. A complete list of OCT metrics tested can be referenced in the *Appendix* (App. A3).

4.2.5 Pilot Study Experimental Design

Prior to collecting OCT data from the seven treatments, a preliminary OCT pilot study was conducted on HepG2, MCF7, and cortical microtissues. Oxidative phosphorylation was inhibited using oligomycin A in MCF7 and cortical microtissues (concentrations of 1, 5, and 10 μM) for 0, 12, and 24-hour exposure periods. Membrane disruption was induced in HepG2 and cortical microtissues using ethanol treatment (concentrations of 1.7 M, 3.4 M, and 5.1 M) for 1 hour in 15-minute intervals. Finally, microtubules were over stabilized in MCF7 microtissues using paclitaxel (0.03, 0.3, and 3 μM) for 0, 12, and 24-hour exposure periods. OCT metrics were then fitted to a linear regression to create dose-response curves (metrics can be referenced in the *Appendix* A3).

The dose-response curves were generated for each concentration separately with exposure time on the x-axis. The slope from each dose-response curve was extrapolated and plotted as a function of increasing concentration. This metric was defined as the responsivity with units of %/dose/time. Region-specific segmentation was calculated based on each voxel's shortest distance to the microtissue surface. This allowed us to define the core, body, and shell regions to have volume fractions of 1/8, 3/8, and 4/8, respectively. For the pilot study, we only compared OCT metrics for the core and body regions. Data collection and analysis for the pilot data was accomplished in collaboration with Adrian Bico Sc.M., Madison Woo Sc.M., and Ramisa Fariha Ph.D.

4.2.6 Linear Regressions and Structural Equation Modeling

Multi-metric OCT data as well as "gold standard" assay data from the CellTiter-Glo 3D, Live/Dead, Caspase-Glo 3/7 3D, and EdU proliferation assays were collected using the previously determined LC values (App. A1). Only HepG2 microtissue data at 24-hour exposure periods were used for further analysis. Sample sizes for each LC condition from OCT, DLS-OCT, and standard assay datasets ranged from n = 30, <10, and 16, respectively. All data was collected from a single experimental replicate for this proof-of-concept application. Data analysis was conducted using Python programming language and involved analyzing data from each compound treatment separately. Data preprocessing first involved a simple bootstrapping approach to impute missing data values to produce a single dataset with n = 30 entries per group for every metric and assay. Bootstrapping involved randomly sampling 2000 data points from the group (i.e., data belonging to the same LC and output) with repetition and averaging them to create a new single entry. This process

was repeated for each missing value. Assay outputs were then normalized to their vehicle controls except for caspase assay data which was normalized using Equation 7. In addition, all OCT metrics were standardized to extract their z-scores. Next, multicollinearity was addressed by calculating the variance inflation factor (VIF) for all OCT metrics. VIF estimation of multicollinearity is a robust and effective approach for regression analysis.[34] OCT metrics with a VIF greater than five were deemed to be highly correlated.[34] The code iteratively excluded one OCT metric with the highest VIF score until all metrics had scores less than five. The remaining OCT metrics were fit to each assay output using a simple linear regression. Regression slopes, R^2 values, mean squared error (MSE), and p-values were determined for each fit. Metrics with significant regression fits ($p < 0.05$) were then passed to the SEM builder in python (*semopy*). This step was crucial since SEM required prior knowledge of which OCT metrics could predict assay outcomes. Initial SEM structure involved one exogenous latent variable which was defined as "cell viability." Next, loading paths were made from "cell viability" to each assay. In *semopy* syntax, this could be written as the following:

$$Viability \ = \sim ATP + LiveDead + Caspase + EdU$$

Next, the code added relationships between each assay and the OCT metrics that passed the regression analysis using the following syntax:

$$SEM\ Model += OCT\ Metric \sim Assay$$

SEM then calculated the regression loadings, variances, covariances, and p-values for each path. SEM models were then transferred to JMP Pro 17 which allowed for the interactive

trimming of paths with insignificant p-values. This process was repeated for each treatment separately to generate a total of seven unique SEM path diagrams.

4.3 Results

4.3.1 Pilot Study Outcomes

A preliminary study was conducted to determine the feasibility of OCT-based viability imaging in HepG2, MCF7, and cortical microtissues using oligomycin A, ethanol, and paclitaxel treatment. The responsivity, which was defined by units of % change/concentration/time, was extracted for all OCT metrics. Only metrics with robust responsivities were reported in Table 3. The selection criteria for the most robust metrics included whether the data had no significant time-dependent changes in the control group ($p > 0.001$) and no significant differences between treatment and control groups at time zero ($p > 0.001$). Data that met these two criteria were considered "canonical" while data that did not meet these criteria were deemed "noncanonical" (NC). Among canonical data,

Table 3. The table summarizes the most robust OCT metrics for the three microtissue types after treatment with oligomycin A, ethanol, and paclitaxel. Metrics were reported in units of %/dose/time. Values to the left of a forward slash "/" are from the spheroid body and values after it are from the core. TBI: to be investigated, NS: not significant, NC: not canonical, C2C: cell-to-cell adhesion, OAC: optical attenuation coefficient, coeff: coefficient, CV: coefficient of variation, DLS: dynamic light scattering. * Surface roughness values are reported for the entire spheroid. Reprinted from the submitted NCI R01 application.

Hypothesized disruption to ▼	Known Disruption to: Treatment:	Metabolic viability Oligomycin		Membrane integrity Ethanol		Cytoskeleton Paclitaxel
	Cell type:	Neuro	MCF7	Neuro	HepG2	MCF7
	▼ Metrics	N=315	N=1073	N=2015	N=808	N=1983
Metabolic viability (TBI)	Diffusion coeff.	**-2.7 / NS**	NC	NC	NS	NC
	Intensity CV	**7.8 / 4.5**	NS	NC	NC	NS
	OAC CV	**6.5 / 5.3**	NS	NS	NC	NS
	DLS statics ratio CV	NS	**6.1 / 11**	NS	NS	NS
Membrane integrity (TBI)	Diffusion coeff. CV	NS	NS	**-13 / NS**	NS	NS
	Decorrel. CV	NS	NS	**-5.1 / -4.2**	NC	NS
	Normalized decorrel. CV	NS	NC	NC	**6.4 / 4.3**	NS
Cytoskeleton	OAC	NS	NS	NS	NS	**-41 / -36**
C2C adhesion	Surface roughness*	**0.7**	**1.4**	**0.6**	**3.7**	**0.8**
	Responsivity unit:	(%/μM/day)	(%/μM/day)	(%/M/hour)	(%/M/hour)	(%/μM/day)

metrics without a significant interaction term (i.e., $dose * time$) were categorized as "nonsignificant" (NS) ($p > 0.05$). The hypothesized biological perturbation responsible for the changes in each canonical OCT output was listed as well. This analysis was repeated for each microtissue's body and core regions, and a total of 6194 spheroids were analyzed.

Results from the pilot study revealed that different microtissues elicited robust responses from unique sets of OCT metrics despite receiving the same treatments. This can be confirmed since each metric elicited a robust response once for every row (in bold, Table 3). The exception for this was surface roughness which elicited a robust response across all treatments and microtissue types. Furthermore, the results showed that each cellular perturbation elicited at least one robust response (i.e., all columns have at least one entry). The diffusion coefficient and its coefficient of variation (CV) were the only metrics with a canonical response in the body but not the core (Table 3). Metric responsivities were generally higher in the body compared to the core regions as well, except for the DLS statics ratio CV which was higher in the core in oligomycin A treated MCF7 microtissues.

4.3.2 Linear Regression Analysis

Prior to linear regression analysis, OCT metrics with high multicollinearity were excluded to improve the reliability of the regression fit (i.e., VIF > 5). The resulting metrics and their final VIF scores were reported in the *Appendix* (App. A4). These metrics were then correlated to each assay using a simple linear regression (Table 4). Only regression fits with R^2 values greater than 0.25 and statistically significant p-values ($p < 0.05$) were reported. In addition, the regression analyses were grouped based on similar biological perturbations for easier comparison.

Table 4. Table summarizing the linear regression fits. Only statistically significant fits ($p < 0.05$) with R^2 values greater than 0.25 were reported. Treatments that elicited similar biological perturbations were grouped together.

2DG				
Assay	**Predictor**	**Slope**	**R^2**	**MSE**
ATP	Ms	-0.22	0.55	0.04
ATP	NormDecSD4	0.20	0.48	0.04
Caspase	NormDecSD4	-0.21	0.45	0.05
EdU	Ms	-0.19	0.48	0.04
EdU	NormDecSD4	0.15	0.32	0.05
Oligomycin A				
Assay	**Predictor**	**Slope**	**R^2**	**MSE**
ATP	DROAC4CV	-0.28	0.58	0.06
ATP	Ms	0.25	0.45	0.08
ATP	DopplerAbsSD	-0.22	0.34	0.09
ATP	OAC_CV	-0.21	0.32	0.09
Caspase	DROAC3SD	-0.14	0.25	0.06
EdU	DROAC4CV	-0.31	0.60	0.07
EdU	Ms	0.28	0.48	0.09
EdU	DopplerAbsSD	-0.23	0.33	0.11
EdU	OAC_CV	-0.21	0.28	0.12
LiveDead	DROAC4CV	-0.03	0.31	0.00

Cisplatin				
Assay	**Predictor**	**Slope**	**R^2**	**MSE**
Caspase	DopplerAbsCV	0.79	0.29	1.55
EdU	DopplerAbsCV	0.24	0.44	0.07
EdU	DROACcc1CV	-0.18	0.26	0.10
LiveDead	DopplerAbsCV	0.03	0.29	<0.01
Melphalan				
Assay	**Predictor**	**Slope**	**R^2**	**MSE**
Caspase	D_SD	0.11	0.32	0.03
Caspase	Ms	0.11	0.32	0.03
EdU	Ms	0.32	0.78	0.03
EdU	D_SD	0.23	0.40	0.08
EdU	DROACcc1SD	-0.22	0.34	0.09
LiveDead	Ms	0.08	0.44	0.01
LiveDead	D_SD	0.08	0.40	0.01

Triton X-100				
Assay	**Predictor**	**Slope**	**R^2**	**MSE**
ATP	DROACcc3CV	-0.30	0.51	0.09
ATP	SR	-0.30	0.50	0.09
ATP	DROAC4CV	-0.26	0.40	0.11
ATP	Shift2	-0.24	0.32	0.12
ATP	Decay2SD	-0.22	0.27	0.13
Caspase	DROACcc3CV	-0.72	0.39	0.83
Caspase	Shift2	-0.69	0.35	0.87
Caspase	SR	-0.65	0.31	0.92
EdU	Shift2	-0.16	0.31	0.06
EdU	SR	-0.16	0.31	0.06
EdU	DROACcc3CV	-0.16	0.30	0.06
EdU	DROAC4CV	-0.15	0.28	0.06
LiveDead	SR	-0.16	0.45	0.03
LiveDead	AVR	0.13	0.30	0.04
LiveDead	DROACcc3CV	-0.13	0.29	0.04
Melittin				
Assay	**Predictor**	**Slope**	**R^2**	**MSE**
ATP	DROACcc4SD	-0.21	0.45	0.06
ATP	DROACcc3CV	-0.21	0.42	0.06
ATP	Decorrelation	-0.20	0.38	0.06
ATP	DROAC4CV	-0.19	0.35	0.07
ATP	DopplerAbsSD	0.17	0.27	0.08
ATP	DROACcc3	-0.17	0.27	0.08
Caspase	Decorrelation	0.19	0.45	0.04
Caspase	DopplerAbsSD	-0.18	0.43	0.04
Caspase	DROACcc3	0.17	0.37	0.05
Caspase	DROACcc4SD	0.16	0.35	0.05
Caspase	DROACcc3CV	0.15	0.29	0.05
LiveDead	Decorrelation	-0.18	0.51	0.03
LiveDead	DROACcc4SD	-0.18	0.50	0.03
LiveDead	DROACcc3	-0.16	0.37	0.04
LiveDead	DROACcc3CV	-0.15	0.34	0.04
LiveDead	DROAC4CV	-0.14	0.30	0.05
LiveDead	DopplerAbsSD	0.14	0.28	0.05

Paclitaxel				
Assay	**Predictor**	**Slope**	**R^2**	**MSE**
ATP	Mf	-0.08	0.34	0.01
EdU	Mf	0.22	0.39	0.07
EdU	DROACcc3	-0.19	0.28	0.09
EdU	D	0.18	0.26	0.09
EdU	OAC_CV	-0.18	0.26	0.09
EdU	AVR	0.18	0.25	0.09

Visual inspection across the treatment groups revealed no clear overlap in the predictive ability of OCT metrics across assays. The metabolic inhibitors 2DG and oligomycin A did not elicit a strong assay-predictor response with the largest slope magnitude belonging to the EdU-DROAC4CV combination (slope = -0.31, R^2 = 0.60). Cisplatin produced the largest response among alkylating agents, which produced a slope of 0.79 and R^2 of 0.29 for the caspase-DopplerAbsCV combination. Among the membrane disrupting agents, the Triton X-100 treatment contained the largest response with a slope of -0.72 and R^2 of 0.39 for the caspase-DROACcc3CV combination. Finally, the largest response in the paclitaxel treatment group was reported from the EdU-Mf combination with a slope of 0.22 and R^2 of 0.39. All the OCT metrics reported in Table 4 had statistically significant fits and were utilized for the next analytical step involving SEM.

4.3.3 Structural Equation Modeling

Initial SEMs were constructed on OCT metrics listed in Table 4. Nonsignificant paths were trimmed, and the SEM was rerun. Final path diagrams for each treatment condition were graphed (App. A5). Ultimately, predictor and outcome effects were calculated for all variables with causal relationships (i.e., connected variables). These

results were reported as parameter estimates with an associated Wald test z-statistic which determined statistical significance ($z < 0.05$). Larger estimates imply larger effects, and positive or negative values indicate the directionality of the relationship. Notably, oligomycin A and cisplatin models did not produce significant paths between OCT metrics and the Live/Dead assay (App. A6). In addition, the paclitaxel model did not produce a significant path with the caspase assay (App. A6). Indirect effects between the latent variable "cell viability" and the OCT metrics were also estimated. Among all treatments, melphalan produced the indirect estimates with the greatest magnitudes including Ms, D_SD, DROACcc1SD, and Decay2SD with values of 17.0, 15.2, -11.28, and -9.0, respectively. The remainder of the SEM estimate magnitudes were under four. Both direct and indirect effects were summarized in tables found in the *Appendix* (App. A6). Assessments of model fit included the comparative fit index (CFI) and root mean square error of approximation (RMSEA), and they were determined for each SEM fit (Table 5).

Table 5. Comparative fit index (CFI) and root mean square error of approximation (RMSEA) for structural model equations built from data testing seven different treatments in HepG2 spheroids (columns). 2DG: 2-Deoxy-D-glucose, Oli: oligomycin A, Tri: Triton X-100, Mel: melittin, Cis: cisplatin, Mef: melphalan, Pac: paclitaxel.

	2DG	Oli	Tri	Mel	Cis	Mef	Pac
CFI	0.646	0.790	0.646	0.615	0.480	0.702	0.671
RMSEA	0.162	0.213	0.227	0.204	0.200	0.167	0.182

4.4 Discussion

In this study, an analytical framework was proposed to characterize and model OCT viability metrics with "gold standard" assays. Initial results from the pilot study suggested

that OCT metrics were both sensitive and specific to the type of biological perturbation induced. This was confirmed since every perturbation caused by either oligomycin A, ethanol, or paclitaxel treatment elicited a statistically significant response to at least one OCT metric for every microtissue type (Table 3). Furthermore, every OCT metric output was uniquely significant to a single perturbation, even when two different microtissue types were treated with the same compound, except for surface roughness (Table 3). This observation may be due to the presence of different cell death mechanism elicited by each microtissue; however, no cell viability assays were used to confirm cell death. It is therefore possible that the significant changes in OCT responsivity may be due to cellular reactions to the treatment that may not result in cell death. Further characterization of the OCT metrics using viability assays would be required prior to making biological interpretations. Nevertheless, both sensitivity and specificity are necessary requirements of a robust viability assay. An assay that is not sensitive would fail to capture changes to viability (false negative) while a nonspecific assay may inaccurately associate unrelated cellular events to cell death (false positive). The nonspecific nature of the surface roughness metric may be due to its overlapping contribution to a variety of cell death pathways or responses. Another finding from the preliminary experiment involved the differences in OCT metric responsivity between the core and body regions. The elevated metrics in the body region relative to the core coincided with our hypothesis that diffusion gradients could impact the pharmacological efficacy of a treatment.[22,23] This is due to a decrease in treatment bioavailability in deeper tissue regions. Other factors like pH, O_2 levels, and metabolic profiles could also exert some influence on treatment efficacy.[23] Overall, the pilot study findings supported our OCT-based viability imaging approach.

Many OCT metrics were calculated and derived from the three scanning protocols implemented in this study. Metrics that broadly relate to the same fundamental output (i.e., decorrelation, normalized decorrelation, and their CV) could introduce multicollinearity in our dataset. Inadequately addressed multicollinearity can lead to increased variance and standard error in the regression analyses.[35] VIF adjustments were implemented to redefine our OCT predictor variables for more accurate fitting. The table from Appendix 4 showed that most OCT metrics experienced some interdependence. The threshold selected for this study was based on literature recommendations;[34] however, its value could be reduced to generate a more conservative list of OCT predictors. One notable challenge associated with the VIF removal of OCT metrics involves the inconsistent selection of parameters across datasets from different treatments. Ultimately, it may be beneficial for the analytical framework to comprehensively assess the multicollinearity of metrics across experiments for improved reliability and repeatability.

After data preprocessing, simple linear regressions were used to generate lines of best fit for each OCT metrics and assay. We have previously stated that linear mixed effects (LME) models are more robust implementations of linear regressions; however, we were unable to implement it effectively due to the limited number of experimental replicates. Future implementations of this framework would greatly benefit from utilizing the LME model to account for random errors. LME models are also robust against violations to their statistical assumptions (e.g., normality, linearity, and absence of outliers) which would greatly improve the reliability of the regression significance testing.[36] This is particularly important since thresholding the p-value served as a method to identify the best predictors for the SEM model. Implementing LME models may also improve the slopes, R^2, and MSE

derived from each fit. The majority of R^2 values fell below the moderate benchmark of 0.5 which may suggest that most OCT metrics were not able to capture changes in cell viability assay data with high fidelity. Nevertheless, the exact slopes and R^2 from this step in the framework were not crucial for the formation of the prediction model; rather, they served as checkpoint markers to predetermine which assays and OCT metrics were of interest. For example, the Mf metric carried the highest slope and R^2 values for the paclitaxel treatment group (Table 4). Further down the analysis pipeline, we see that cell viability had the largest impact on Mf among the indirect effects (App A6). Similar trends can be observed by comparing OCT metric slopes in Table 4 and cell viability effects in Appendix 6.

The final step in the proposed framework culminated in the generation of SEM fits and path diagrams. Path diagrams provided a visual representation of the multivariate model with opportunities to identify the interrelations between OCT metrics and multiple assay outputs (App. A5). SEM loadings, which are also displayed on the path diagrams, provide additional information regarding the multivariate model. First, the sign of the loadings between "cell viability" and each assay indicates the directionality of the relationship. The directionality imposed by the SEM matched those in both LME regression models and PCA loadings for HepG2 microtissues (App. A5, A6, Figs 12 and 17). Second, the magnitude of a loading corresponds to the degree of association between a factor and indicator. PCA and SEM loadings were similar; however, they did not perfectly match. This is understandable since both approaches are unique in their theory and application. The SEM approach also enabled for the indirect correlation between holistic cell viability and OCT metric predictors (App A6). Indirect effects can be calculated by multiplying the loading along with path diagram. For instance, the loading between cell

viability and the ATP assay can be multiplied by the loading between the ATP assay and its OCT metric. Indirect loadings can then be summed if their relationship to cell viability exists among multiple paths. Indirect loadings can be interpreted in the same manner as direct loadings. Using this approach, we can generate a model of OCT metrics that correlate and predict cell viability via multiple cell death pathways.

The SEM fits presented in this study provide a general framework for the implementation of multivariate cell viability prediction models using both "gold standard" assays and OCT metrics. Biological interpretation of the models in their present state may be unreliable. One primary indication of the model fit involves assessing the CFI and RMSEA. As a general guideline, CFI should be greater than 0.9 and RMSEA should be less than 0.1. All SEM fits showed poor fitting and therefore should not be overinterpreted (Table 5). This can be largely due to the small sample size used to model our equations. SEM approaches require very large datasets for accurate modeling with $N \geq 500$, whereas the dataset used herein had a sample size $N \leq 120$.[37] As a result, improving the model fits will heavily rely on increasing the sample size.

4.5 Conclusion

Overall, the goal of this aim was to characterize OCT imaging metrics using "gold standard" cell viability assays. An analytical pipeline which involved linear regressions followed by SEM provided a feasible approach to model cell viability through OCT metrics. SEM is a powerful and flexible statistical tool that allows for the testing of causal relationships in data. Nevertheless, this approach requires large datasets and *a priori*

information regarding the structure of the data. Future experiments will involve modeling the entire multi-assay dataset from the previous chapter alongside the associated OCT data to validate the framework's reproducibility across microtissue type. Furthermore, SEM pathways can be modified to improve estimation outcomes and modeling fits; however, these adjustments need to be logically sound and theoretically palatable. Alternative path diagrams can be built and tested to iteratively define a more robust model in accordance with the data at hand. Finally, SEM may be used to inform future algorithms in the analysis pipeline which could benefit from neural networks or machine learning to improve the predictive value of OCT viability imaging.

4.6 References

1. Huang, D. *et al.* Optical Coherence Tomography. *Science* **254**, 1178–1181 (1991).

2. Leitgeb, R. A. *et al.* Ultrahigh resolution Fourier domain optical coherence tomography. *Opt. Express* **12**, 2156–2165 (2004).

3. Aumann, S., Donner, S., Fischer, J. & Müller, F. Optical Coherence Tomography (OCT): Principle and Technical Realization. in *High Resolution Imaging in Microscopy and Ophthalmology: New Frontiers in Biomedical Optics* (ed. Bille, J. F.) (Springer, Cham (CH), 2019).

4. Costa, R. A. *et al.* Retinal assessment using optical coherence tomography. *Prog. Retin. Eye Res.* **25**, 325–353 (2006).

5. Gambichler, T., Pljakic ,Azem & and Schmitz, L. Recent advances in clinical application of optical coherence tomography of human skin. *Clin. Cosmet. Investig. Dermatol.* **8**, 345–354 (2015).

6. Wang, J., Xu, Y. & Boppart, S. A. Review of optical coherence tomography in oncology. *J. Biomed. Opt.* **22**, 121711 (2017).

7. Halfter, K. *et al.* Prospective cohort study using the breast cancer spheroid model as a predictor for response to neoadjuvant therapy--the SpheroNEO study. *BMC Cancer* **15**, 519 (2015).

8. Mulholland, T. *et al.* Drug screening of biopsy-derived spheroids using a self-generated microfluidic concentration gradient. *Sci. Rep.* **8**, 14672 (2018).

9. Sharma, U., Chang, E. W. & Yun, S. H. Long-wavelength optical coherence tomography at 1.7 μm for enhanced imaging depth. *Opt. Express* **16**, 19712–19723 (2008).

10. Sirenko, O. *et al.* Phenotypic Characterization of Toxic Compound Effects on Liver Spheroids Derived from iPSC Using Confocal Imaging and Three-Dimensional Image Analysis. *ASSAY Drug Dev. Technol.* **14**, 381–394 (2016).

11. Jung, Y., Klein, O. J., Wang, H. & Evans, C. L. Longitudinal, label-free, quantitative tracking of cell death and viability in a 3D tumor model with OCT. *Sci. Rep.* **6**, 27017 (2016).

12. Roberge, C. L. *et al.* Non-Destructive Tumor Aggregate Morphology and Viability Quantification at Cellular Resolution, During Development and in Response to Drug. *Acta Biomater.* **117**, 322–334 (2020).

13. Mourant, J. R. *et al.* Mechanisms of light scattering from biological cells relevant to noninvasive optical-tissue diagnostics. *Appl. Opt.* **37**, 3586–3593 (1998).

14. Pasternack, R. M., Zheng, J.-Y. & Boustany, N. N. Optical scatter changes at the onset of apoptosis are spatially associated with mitochondria. *J. Biomed. Opt.* **15**, 040504 (2010).

15. Mourant, J. R. *et al.* Light scattering from cells: the contribution of the nucleus and the effects of proliferative status. *J. Biomed. Opt.* **5**, 131–137 (2000).

16. Wu, T. T., Qu, J. Y. & Xu, M. Unified Mie and fractal scattering by biological cells and subcellular structures. *Opt. Lett.* **32**, 2324–2326 (2007).

17. Farhat, G., Yang, V. X. D., Czarnota, G. J. & Kolios, M. C. Detecting cell death with optical coherence tomography and envelope statistics. *J. Biomed. Opt.* **16**, 026017 (2011).

18. Jeong, K., Turek, J. J. & Nolte, D. D. Volumetric motility-contrast imaging of tissue response to cytoskeletal anti-cancer drugs. *Opt. Express* **15**, 14057–14064 (2007).

19. El-Sadek, I. A. *et al.* Three-dimensional dynamics optical coherence tomography for tumor spheroid evaluation. *Biomed. Opt. Express* **12**, 6844–6863 (2021).

20. Holmes, C., Tabrizian, M. & Bagnaninchi, P. O. Motility imaging via optical coherence phase microscopy enables label-free monitoring of tissue growth and viability in 3D tissue-engineering scaffolds. *J. Tissue Eng. Regen. Med.* **9**, 641–645 (2015).

21. Martucci, N. J. *et al.* Nondestructive Optical Toxicity Assays of 3D Liver Spheroids with Optical Coherence Tomography. *Adv. Biosyst.* **2**, 1700212 (2018).

22. Mueller-Klieser, W. Tumor biology and experimental therapeutics. *Crit. Rev. Oncol. Hematol.* **36**, 123–139 (2000).

23. Pandkar, M. R., Dhamdhere, S. G. & Shukla, S. Oxygen gradient and tumor heterogeneity: The chronicle of a toxic relationship. *Biochim. Biophys. Acta Rev. Cancer* **1876**, 188553 (2021).

24. Huang, Y. *et al.* Optical Coherence Tomography Detects Necrotic Regions and Volumetrically Quantifies Multicellular Tumor Spheroids. *Cancer Res.* **77**, 6011–6020 (2017).

25. van der Meer, F. J. *et al.* Apoptosis- and necrosis-induced changes in light attenuation measured by optical coherence tomography. *Lasers Med. Sci.* **25**, 259–267 (2010).

26. Stefan, S. *et al.* Determination of confocal profile and curved focal plane for OCT mapping of the attenuation coefficient. *Biomed. Opt. Express* **9**, 5084–5099 (2018).

27. Yang, H. *et al.* Effect of image quality fluctuations on the repeatability of thickness measurements in swept-source optical coherence tomography. *Sci. Rep.* **10**, 13897 (2020).

28. Kim, J. H. *et al.* Effect of signal strength on reproducibility of circumpapillary retinal nerve fiber layer thickness measurement and its classification by spectral-domain optical coherence tomography. *Jpn. J. Ophthalmol.* **55**, 220–227 (2011).

29. Lee, E. S., Kim, H. & Kim, J. M. Effect of signal strength on reproducibility of peripapillary retinal nerve fiber layer thickness measurement and its classification by time-domain optical coherence tomography. *Jpn. J. Ophthalmol.* **54**, 414–422 (2010).

30. Lee, J., Wu, W., Jiang, J. Y., Zhu, B. & Boas, D. A. Dynamic light scattering optical coherence tomography. *Opt. Express* **20**, 22262–22277 (2012).

31. Harlow, L. L. Structural Equation Modeling. in *The Essence of Multivariate Thinking* (Routledge, 2023).

32. Principles and Practice of Structural Equation Modeling: Fifth Edition. *Guilford Press* https://www.guilford.com/books/Principles-and-Practice-of-Structural-Equation-Modeling/Rex-Kline/9781462551910?srsltid=AfmBOopa5JKPVkyPh2bs8S6nVLQLzf72Hx0Ii-tzTRnwzQRW8aSdlan8.

33. Vermeer, K. A., Mo, J., Weda, J. J. A., Lemij, H. G. & Boer, J. F. de. Depth-resolved model-based reconstruction of attenuation coefficients in optical coherence tomography. *Biomed. Opt. Express* **5**, 322–337 (2014).

34. Daoud, J. I. Multicollinearity and Regression Analysis. *J. Phys. Conf. Ser.* **949**, 012009 (2017).

35. Kim, J. H. Multicollinearity and misleading statistical results. *Korean J. Anesthesiol.* **72**, 558–569 (2019).

36. Schielzeth, H. *et al.* Robustness of linear mixed-effects models to violations of distributional assumptions. *Methods Ecol. Evol.* **11**, 1141–1152 (2020).

37. Shi, D., Lee, T. & Maydeu-Olivares, A. Understanding the Model Size Effect on SEM Fit Indices. *Educ. Psychol. Meas.* **79**, 310–334 (2019).

CHAPTER 5: STUDY CONCLUSION

5.1 Summary

Functional precision medicine (FPM) approaches to cancer therapy involve directly testing antitumor drugs on a patient's tumor outside the body. This provides doctors with empirical evidence regarding the efficacy of prospective therapies. This approach has the potential to outperform the predictive power of genetic screens since many tumorigenic mutation drivers are unknown or aren't matched with a treatment. While very promising, FPM approaches face technological challenges that make it difficult to implement in the clinic. One major challenge with *in vitro* testing involves the loss of clinical relevance. Traditional two-dimensional models force tumors to grow on planar surfaces that are not representative of the native tissue. The changes in physiological conditions may cause the cells to genetically drift and express altered phenotypes compared to the cells from the original tissue. Tumor cells with altered phenotypes will respond differently to treatments which limit their ability to predict the patient's tumor drug response. The second major challenge involves generating and empirically testing multiple chemotherapeutic agents for a successful drug screen. This is logistically challenging and presents a major hurdle for the widespread implementation of FPM. Cell viability assays that are commonly used to assess the results from screening studies are cytotoxic, have constraints resolving thicker

3D tissues, and only provide information regarding a limited number of biomarkers. These barriers to implementation must be addressed prior to the successful application of FPM approaches.

First, the recent development of 3D *in vitro* models has transformed the field of tissue culture. 3D models successfully bridge the gap between complex *in vivo* models and highly reproducible *in vitro* models. These 3D cultures can be generated readily from patient-derived cells and successfully predict the patient's tumor drug response. Many platforms exist for the formation of these 3D cultures including self-assembling microtissues which was used in this study. These microtissues do not require specialized equipment or exogenous scaffolding proteins to promote tissue growth. The platform is also easily scalable and allows for the simultaneous testing of 96 spheroids in a high-throughput manner.

The second challenge, however, is not fully addressed. In this thesis, we propose the utilization of OCT viability imaging to overcome many challenges poised by current cell viability assays. OCT is a label-free, noninvasive, and 3D-capable imaging modality that enables the true longitudinal assessment of a sample. Its millimeter penetration depth makes it a versatile approach that can be implemented in free-floating or hydrogel cultures. Previous studies have shown the feasibility of implementing OCT as a viability imaging tool; however, the biological mechanisms that explain changes in OCT metrics are not fully understood. Furthermore, many studies implement a limited number of metrics or tissue culture samples which restrict the scope of their studies.

In this thesis, we present a comprehensive and detailed workflow that entails collecting cell viability data from optimized dose ranges (Chapter 2), extracting multivariate and multi-modal features (Chapter 3), and correlating the "gold standard" viability data to our OCT metrics using multivariate approaches (Chapter 4). We implemented this experimental design by culturing 3D microtissues from HepG2 liver cancer, MCF7 breast cancer, and primary neonatal cortical rat microtissues. We collected cell viability data from four assays covering distinct biological injuries including the CellTiter-Glo 3D assay, Live/Dead cytotoxicity assay, Caspase-Glo 3/7 3D assay, and the Click-iT EdU assay. Cellular injuries were elicited via metabolic inhibition, membrane poration, DNA damage, and cytoskeletal disruption. We then induced the same injuries to the microtissues using pre-optimized dose concentrations and imaged them with our OCT system.

A total of 77 OCT metrics were extracted covering a broad range of metrics including geometric parameters, intensity, decorrelation, normalized decorrelation, optical scattering attenuation, and diffusion coefficient. After data collection, the respective datasets were processed through a proposed workflow (Chapter 4) that identified prospective OCT metrics that could predict assay output. This was accomplished by utilizing a linear regression model to identify metrics with statistically significant fits. Next, the selected metrics were fitted using structural equation modeling (SEM). SEM allowed us to construct a predictive model that relates cell viability (as a difficult to measure, intangible factor) to measured assay outputs. From the assay outputs, we inferred causal relationships to OCT metrics based on the results from the linear regressions. Initial SEM fits were made then trimmed to maintain statistically significant paths. Relationships

between cell viability and assay data as well as OCT metrics were derived using the factor loadings provided by the analysis.

The future goal of this project involves developing a powerful, predictive model for OCT viability metrics. Ideally, the model would be able to provide viability predictions based on OCT inputs alone. Theoretically, OCT metrics should be sensitive and specific to different mechanisms of cellular injury and death. This thesis presented a potential framework to approach this goal through commonly used multivariate techniques. These techniques could be used independently or in conjunction with other analysis pipelines to establish a robust and reliable predictive model.

Once successful, OCT's introduction to FPM applications would provide substantial improvements to analytical power and workflow. OCT viability imaging would maximize the data that could be extracted from a limited biopsy. This approach would enable the longitudinal monitoring of the same samples which would allow for repeated measures assessment of biological data. This statistical approach is inherently less noisy than collecting data from multiple independent datasets. The temporal dynamics of tumor cells can also be observed and modeled using OCT-based methods. For example, the development of chemoresistance could be tracked longitudinally in the same patient-derived sample. OCT-based methods could also test the efficacy of second-line therapies in parallel or prior to their administration to the patient. Implementing the OCT-FPM screen would provide doctors with empirical evidence regarding the therapeutic capacity of various antitumor drugs. Ultimately, a patient would receive a therapy that is most effective against their cancer which would minimize the risk of unsuccessful treatment, recurrence, or death.

APPENDIX

A1. Summary Table of LCs and $MMLC_{50}$

Appendix 1. Lethal concentrations (LC) resulting in 25, 50, and 75 percent cell death utilizing "best fit" assays were reported alongside the multi-mechanisms LC_{50} ($MMLC_{50}$). The $MMLC_{50}$ values were derived from principal component analysis run on multimodal assay data. 2DG: 2-Deoxy-D-glucose, Oli: oligomycin A, Tri: Triton X-100, Mel: melittin, Cis: cisplatin, Mef: melphalan, Pac: paclitaxel, BPL: beyond the practical limit, NA: not applicable, ATP: CellTiter-Glo 3D assay, L/D: Live/Dead assay, Cas: Caspase-Glo 3/7 3D assay, EdU: Click-iT EdU proliferation assay, Neuro: neurospheroids. Published in Zein-Sabatto A., et al., 2025.

		2DG [mM]		**Oli [µM]**		**Tri [%]**		**Mel [µM]**		**Cis [µM]**		**Mef [µM]**		**Pac [µM]**	
		ATP	MMLC 50	ATP	MMLC 50	L/D	MMLC 50	L/D	MMLC 50	Cas	MMLC 50	Cas	MMLC 50	EdU	MMLC 50
HepG2	LC25	15		242		0.0034		2.8		11		31		37	
	LC50	52	55	BPL	NA	0.0054	0.0034	5.6	5.5	12	12	34	29	81	NA
	LC75	181		BPL		0.0090		11.1		14		38		BPL	
MCF7	LC25	3		0.002		0.0023		3.5		120		48		0.001	
	LC50	29	21	0.53	0.023	0.0050	0.0046	7.1	3.4	160	106	58	46	0.041	0.14
	LC75	354		190		0.0110		14.4		214		70		1.4	
Neuro	LC25	47		0.008		0.0034		0.3		5		18		20	
	LC50	110	96	0.058	0.011	0.0059	0.0043	0.6	0.36	7	5	22	17	BPL	NA
	LC75	265		0.455		0.0100		1.2		10		27		BPL	

A2. Longitudinal LME Regression Fits and PCA for MCF7 Microtissues Treated with Paclitaxel

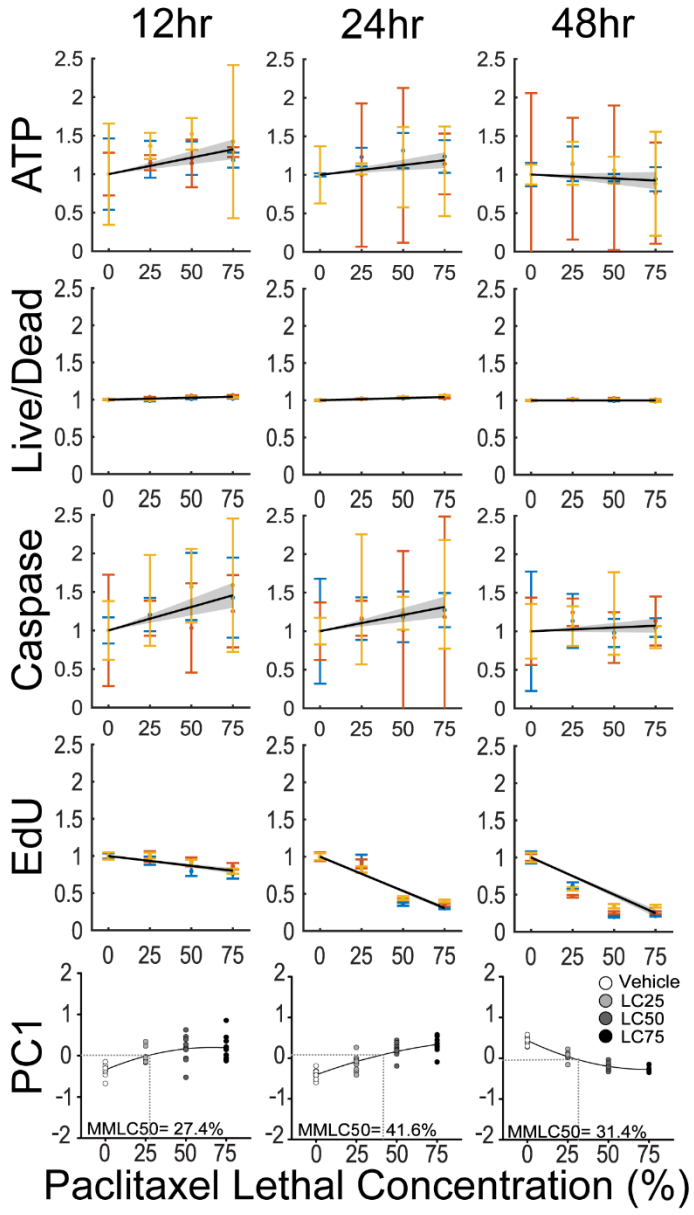

Appendix 2. Linear mixed effects (LME) and principal component analysis (PCA) model regressions were generated from MCF7 microtissues treated with paclitaxel for 12, 24, and 48 hours using previously derived lethal concentrations (LCs). ATP and caspase assay data were generated from three intact gels per condition (n=3 gels per condition; three independent experiments in different colors; N=36 gels). Live/Dead and EdU data were generated from 20 microtissues per condition (n=20 microtissues per condition; three independent experiments in different colors; N=240 microtissues). Prior to running PCA, the MCF7 datasets were matched by truncating the larger datasets to n=9 datapoints per condition. All datasets were normalized to their vehicle controls prior to analysis. Error bars and shaded gray regions signify the 95% confidence intervals. A dose-response was considered substantial when the p-value of the LME fit was $p<0.05$ and the absolute value of the slope was greater than 0.1 (dark gray). Multi-mechanisms LC_{50} ($MMLC_{50}$) was derived from the PCA regressions using methods previously described. Published in Zein-Sabatto A., et al., 2025.

A3. OCT Metric Descriptions

Appendix 3. Table summarizing all OCT metrics collected and their descriptions. Metrics labeled with an asterisk (*) included the standard deviation and coefficient of variation as additional metrics. Metrics labeled with a degree (°) included the standard deviation alone as an additional metric.

Volume	Volume of the microtissue
Area	Surface Area of the microtissue
AVR	Surface Area to Volume ratio
SR	Sphericity
Intensity*	Voxel intensity
Decorrelation*	Time-dependent change in intensity
NormDec*	Decorrelation normalized by Intensity raised to a power from 1-4
OAC*	Optical attenuation coefficient, measures scattering properties
OACcc*	Similar to OAC, but confocal corrected (Sabina et al., 2018)
DROAC*	Depth-resolved OAC, measured per voxel. 1-4 are unique derivation methods
DROACcc*	Similar to DROAC, but confocal corrected
Decay*	Measures random motions (value 0-1)
Decay 2*	Similar to Decay, but accounts for noise
Complex Shift*	Measures both random and translational motions
Shift 2*	Similar to Complex Shift, but accounts for noise
DopplerAbs*	Measures translational motions (>0)
Ms°	Ratio of static particles
Mf°	Ratio of fixed particles
Me°	Ratio of exiting particles
D°	Diffusion coefficient in $\mu m^2/s$
MfD°	Similar to D, but accounts for fixed particles

A4. Variance Inflation Factor Analysis

Appendix 4. Table summarizing the OCT metrics and their variation inflation factors (VIF) after addressing multicollinearity. Metrics with the highest VIF were iteratively removed until all metrics had a VIF<5. 2DG: 2-Deoxy-D-glucose, Oli: oligomycin A, Tri: Triton X-100, Mel: melittin, Cis: cisplatin, Mef: melphalan, Pac: paclitaxel.

Feature	2DG	Oli	Tri	Mel	Cis	Mef	Pac
Volume	1.88				1.98		
AVR			2.02			3.25	2.15
SR	1.40		3.17	2.02	1.55	1.64	1.40
Decorrelation	1.86			3.41			
DecorrelationCV	1.78			2.37	3.60		
NormDec4	1.51						
NormDecCV	2.46						
NormDecSD4	3.18						
OAC					4.88		
OAC_CV	1.90	3.14	2.18	1.84	3.65	1.58	2.08
OAC_SD		3.07	1.31	2.48		2.47	3.47
OACcc				4.09			
OACcc_CV	1.64	2.61	2.44	1.89	2.68	2.32	
OACcc_SD	1.55	2.59			3.22	2.46	4.48
DROAC1		3.63			2.40	1.83	
DROAC1SD	3.31						
DROAC2			3.53				
DROAC2SD							3.72
DROAC3			4.16				
DROAC3CV					1.75	1.56	
DROAC3SD	2.06	1.81					2.12
DROAC4CV	2.10	2.94	2.87	2.55			2.28
DROACcc1CV					3.56	3.87	
DROACcc1SD						3.23	
DROACcc2SD		3.16					
DROACcc3			2.90	2.82	1.55	1.78	2.89
DROACcc3CV	3.30		3.79	3.62	1.79	1.62	
DROACcc3SD	4.25						
DROACcc4CV	3.90						
DROACcc4SD			4.71	2.69	3.24		2.22
DecayCV		2.44					
Decay2						3.63	
Decay2CV							2.41
Decay2SD			3.38			3.20	
ComplexShift	2.78						
DopplerAbsCV	3.33				2.88	3.84	
DopplerAbsSD		3.89		1.92			
Shift2			3.36				
D							1.80
D_SD	1.52	2.83	1.93	2.56	1.84	2.06	1.50
Me_SD			2.67				
Mf						2.08	
Mf_SD	2.13			2.04	4.02		
Ms	2.63	3.33		3.57	4.39	3.72	

A5. Finalized SEM Path Diagrams

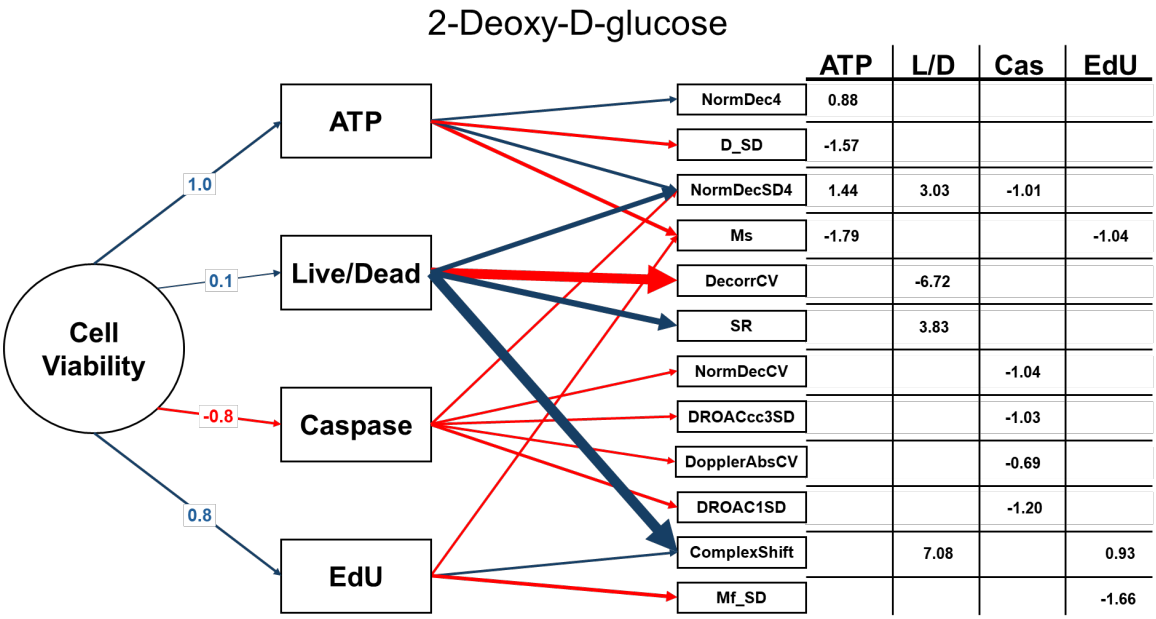

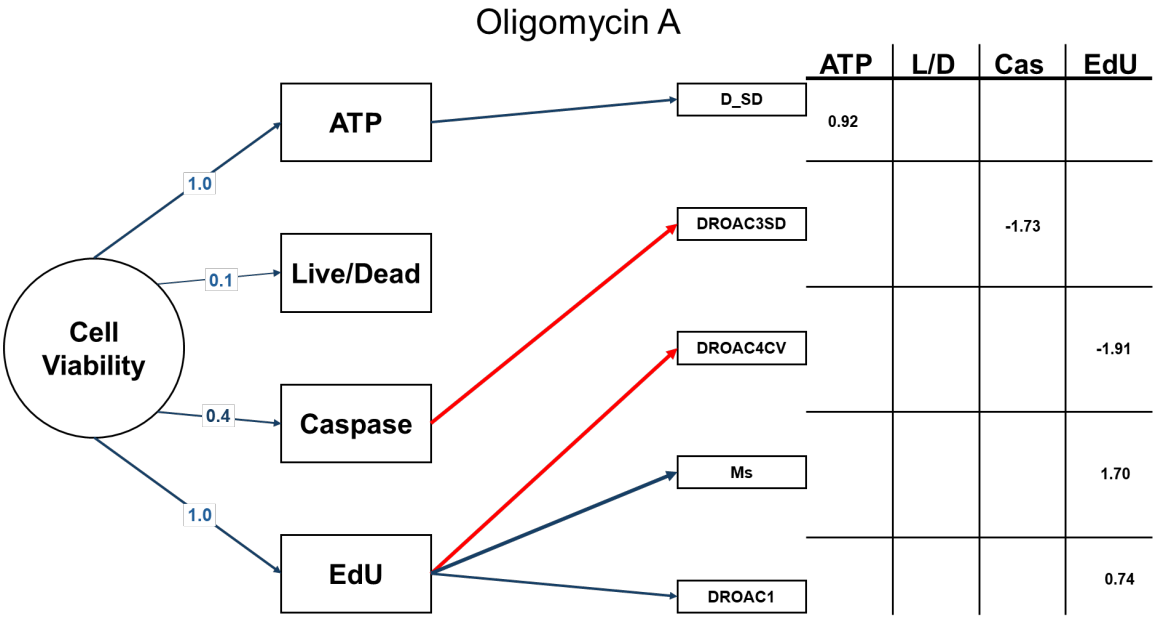

Triton X-100

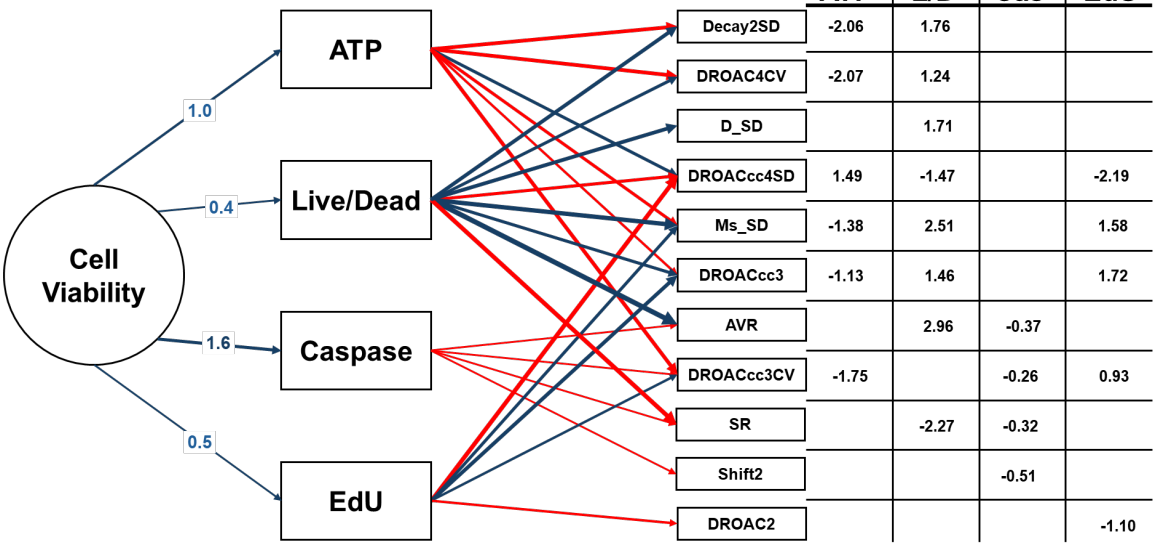

	ATP	L/D	Cas	EdU
Decay2SD	-2.06	1.76		
DROAC4CV	-2.07	1.24		
D_SD		1.71		
DROACcc4SD	1.49	-1.47		-2.19
Ms_SD	-1.38	2.51		1.58
DROACcc3	-1.13	1.46		1.72
AVR		2.96	-0.37	
DROACcc3CV	-1.75		-0.26	0.93
SR		-2.27	-0.32	
Shift2			-0.51	
DROAC2				-1.10

Melittin

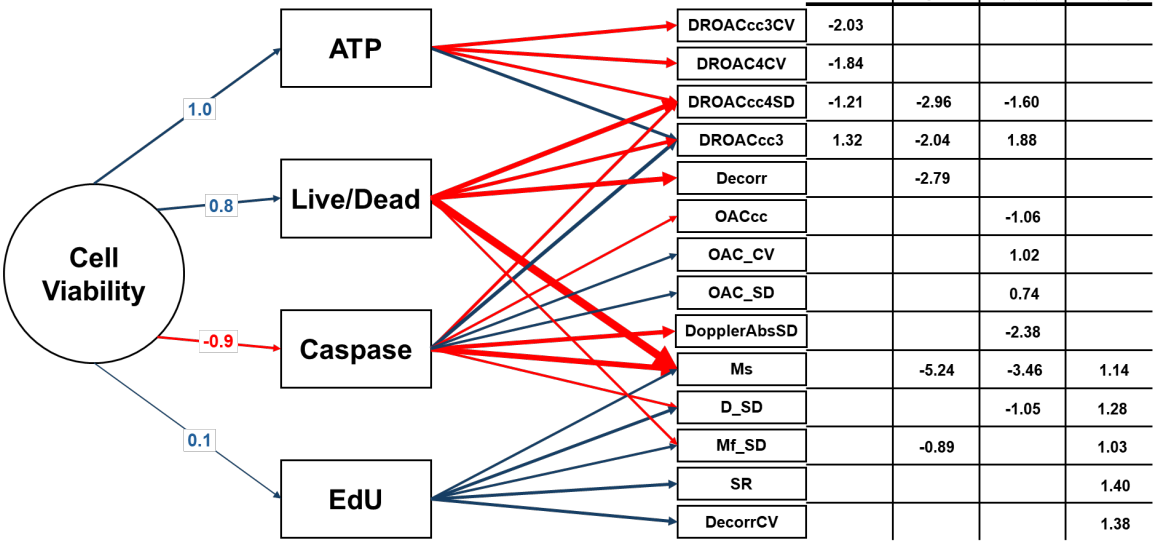

	ATP	L/D	Cas	EdU
DROACcc3CV	-2.03			
DROAC4CV	-1.84			
DROACcc4SD	-1.21	-2.96	-1.60	
DROACcc3	1.32	-2.04	1.88	
Decorr		-2.79		
OACcc			-1.06	
OAC_CV			1.02	
OAC_SD			0.74	
DopplerAbsSD			-2.38	
Ms		-5.24	-3.46	1.14
D_SD			-1.05	1.28
Mf_SD		-0.89		1.03
SR				1.40
DecorrCV				1.38

Cisplatin

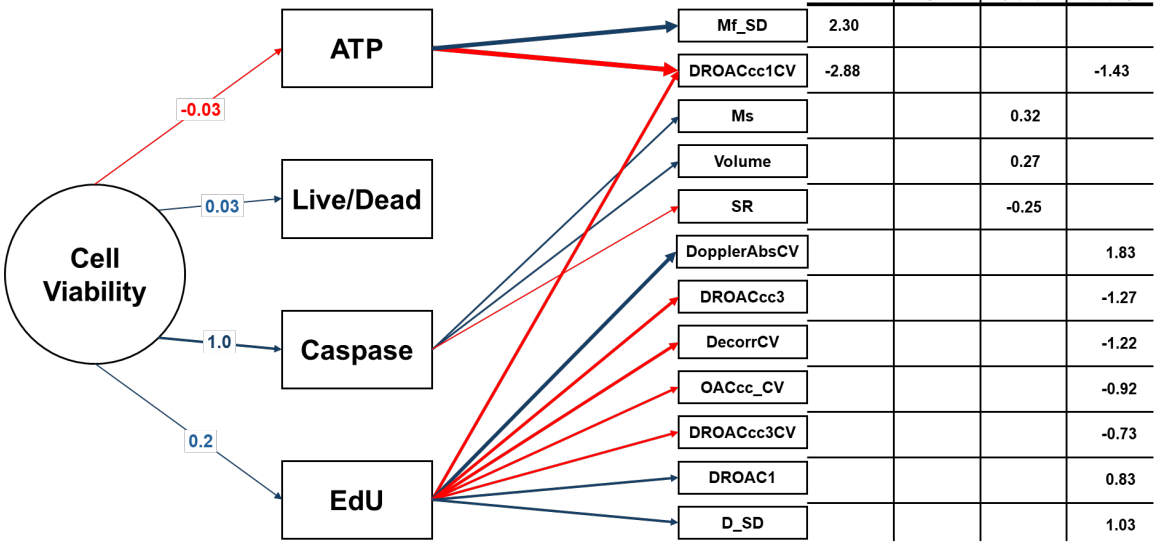

	ATP	L/D	Cas	EdU
Mf_SD	2.30			
DROACcc1CV	-2.88			-1.43
Ms			0.32	
Volume			0.27	
SR			-0.25	
DopplerAbsCV				1.83
DROACcc3				-1.27
DecorrCV				-1.22
OACcc_CV				-0.92
DROACcc3CV				-0.73
DROAC1				0.83
D_SD				1.03

Melphalan

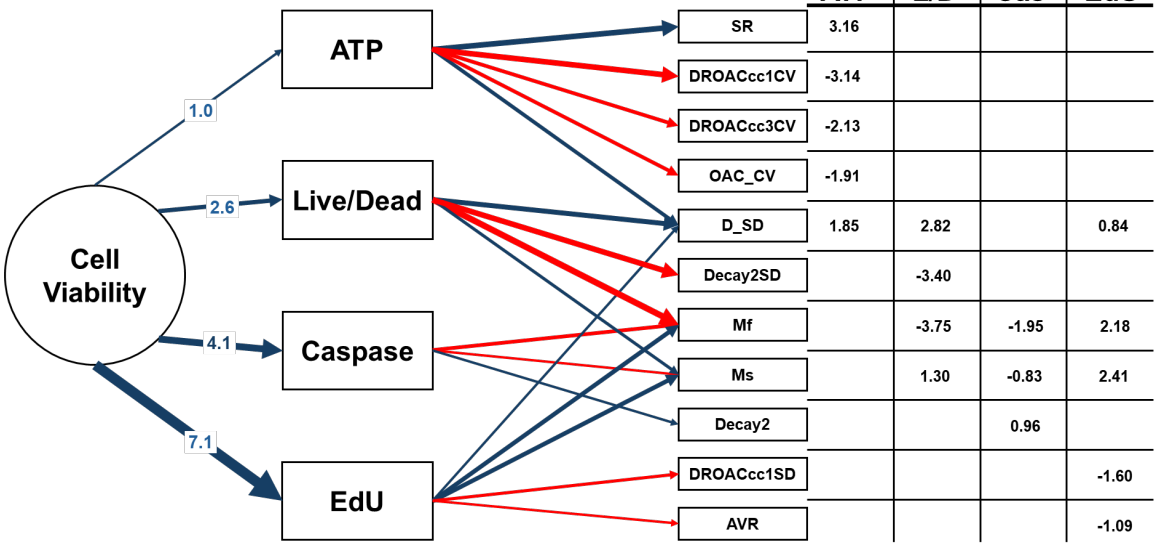

	ATP	L/D	Cas	EdU
SR	3.16			
DROACcc1CV	-3.14			
DROACcc3CV	-2.13			
OAC_CV	-1.91			
D_SD	1.85	2.82		0.84
Decay2SD		-3.40		
Mf		-3.75	-1.95	2.18
Ms		1.30	-0.83	2.41
Decay2			0.96	
DROACcc1SD				-1.60
AVR				-1.09

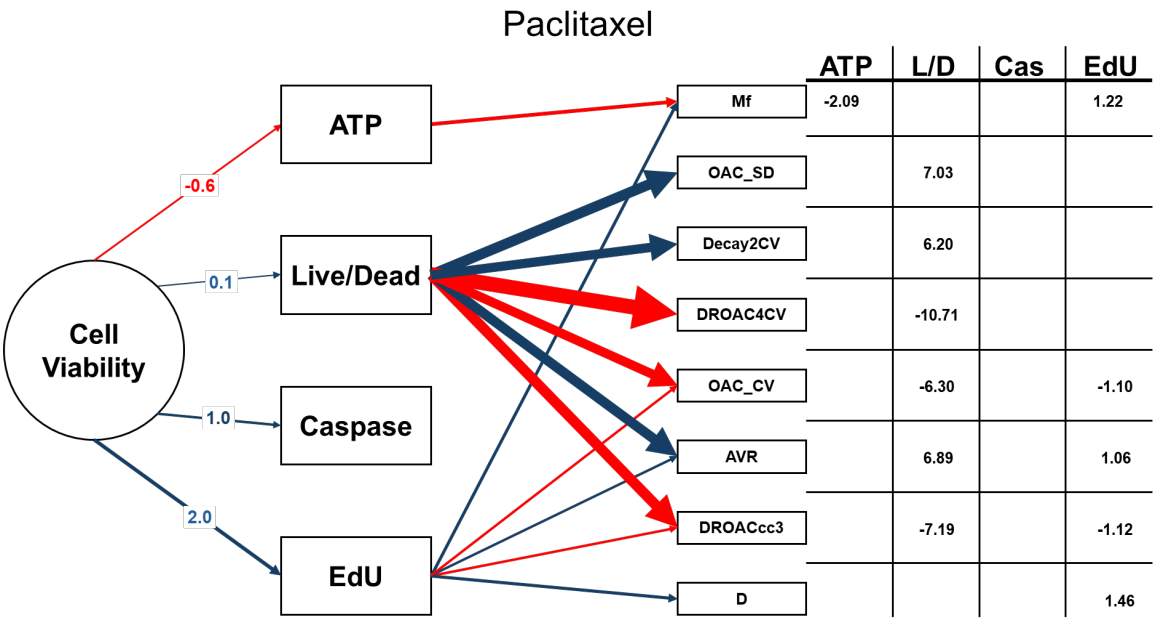

Appendix 5. Path diagrams from the fitted structural equation models. Individual models were fitted for each treatment condition in HepG2 microtissues. Circles represent the latent variable, and rectangles represent the manifest (or observable) variables. Arrows indicate a relationship between two variables. Paths were reported in blue or red and indicate whether the relationship between the variables is positive or negative, respectively. Loadings between the latent variable and each manifest assay variable were reported on the connecting paths. The thickness of the paths reflects the magnitude of the relationship between variables. Direct effects between assays and their OCT predictors were reported in the accompanying table. L/D: Live/Dead and Cas: caspase.

A6. SEM Total Effects

Appendix 6. Total effects estimated by the structural equation model fit. Both direct and indirect effects were calculated for each treatment type separately. Model loadings were reported under "Estimates." Indirect effects were reported when "Cell Viability" was selected as the predictor. A Wald statistical test was conducted to determine significance ($z < 0.05$).

2DG				
Predictor	**Outcome**	**Estimate**	**Std Error**	**Z-value**
ATP	NormDecSD4	1.44	0.29	<.0001
ATP	NormDec4	0.88	0.30	0.0039
ATP	D_SD	-1.57	0.28	<.0001
ATP	Ms	-1.79	0.34	<.0001
LiveDead	ComplexShift	7.08	1.72	<.0001
LiveDead	SR	3.83	1.79	0.0325
LiveDead	NormDecSD4	3.03	1.33	0.0232
LiveDead	DecorrelationCV	-6.72	1.72	<.0001
Caspase	DopplerAbsCV	-0.69	0.29	0.0157
Caspase	NormDecSD4	-1.01	0.28	0.0003
Caspase	DROACcc3SD	-1.03	0.28	0.0002
Caspase	NormDecCV	-1.04	0.28	0.0002
Caspase	DROAC1SD	-1.20	0.27	<.0001
EdU	ComplexShift	0.93	0.32	0.0039
EdU	Ms	-1.04	0.37	0.0051
EdU	Mf_SD	-1.66	0.31	<.0001
Cell Viability	NormDecSD4	2.43	0.23	<.0001
Cell Viability	ComplexShift	1.19	0.27	<.0001
Cell Viability	ATP	1.00	0.00	<.0001
Cell Viability	DROAC1SD	0.93	0.23	<.0001
Cell Viability	NormDec4	0.88	0.30	0.0039
Cell Viability	NormDecCV	0.80	0.23	0.0005
Cell Viability	DROACcc3SD	0.80	0.23	0.0006
Cell Viability	EdU	0.77	0.07	<.0001
Cell Viability	DopplerAbsCV	0.54	0.23	0.0193
Cell Viability	SR	0.26	0.14	0.0595
Cell Viability	LiveDead	0.07	0.02	<.0001
Cell Viability	DecorrelationCV	-0.46	0.16	0.0053
Cell Viability	Caspase	-0.77	0.08	<.0001
Cell Viability	Mf_SD	-1.27	0.26	<.0001
Cell Viability	D_SD	-1.57	0.28	<.0001
Cell Viability	Ms	-2.58	0.22	<.0001

Oligomycin A				
Predictor	**Outcome**	**Estimate**	**Std Error**	**Z-value**
ATP	D_SD	0.92	0.33	0.0047
Caspase	DROAC3SD	-1.73	0.39	<.0001
EdU	Ms	1.70	0.23	<.0001
EdU	DROAC1	0.74	0.30	0.0154
EdU	DROAC4CV	-1.91	0.20	<.0001
Cell Viability	Ms	1.65	0.26	<.0001
Cell Viability	ATP	1.00	0.00	<.0001
Cell Viability	EdU	0.97	0.08	<.0001
Cell Viability	D_SD	0.92	0.33	0.0047
Cell Viability	DROAC1	0.71	0.30	0.0176
Cell Viability	Caspase	0.39	0.08	<.0001
Cell Viability	LiveDead	0.07	0.01	<.0001
Cell Viability	DROAC3SD	-0.67	0.21	0.0012
Cell Viability	DROAC4CV	-1.84	0.25	<.0001

Triton X-100				
Predictor	Outcome	Estimate	Std Error	Z-value
ATP	DROACcc4SD	1.49	0.51	0.0037
ATP	DROACcc3	-1.13	0.52	0.0291
ATP	Ms_SD	-1.38	0.49	0.005
ATP	DROACcc3CV	-1.75	0.27	<.0001
ATP	Decay2SD	-2.06	0.31	<.0001
ATP	DROAC4CV	-2.07	0.28	<.0001
LiveDead	AVR	2.96	0.30	<.0001
LiveDead	Ms_SD	2.51	0.60	<.0001
LiveDead	Decay2SD	1.76	0.54	0.0012
LiveDead	D_SD	1.71	0.35	<.0001
LiveDead	DROACcc3	1.46	0.63	0.0214
LiveDead	DROAC4CV	1.24	0.50	0.0137
LiveDead	DROACcc4SD	-1.47	0.62	0.0181
LiveDead	SR	-2.27	0.27	<.0001
Caspase	DROACcc3CV	-0.26	0.07	0.0002
Caspase	SR	-0.32	0.06	<.0001
Caspase	AVR	-0.37	0.06	<.0001
Caspase	Shift2	-0.51	0.06	<.0001
EdU	DROACcc3	1.72	0.55	0.0016
EdU	Ms_SD	1.58	0.52	0.0024
EdU	DROACcc3CV	0.93	0.38	0.0159
EdU	DROAC2	-1.10	0.30	0.0002
EdU	DROACcc4SD	-2.19	0.54	<.0001
Cell Viability	Caspase	1.64	0.18	<.0001
Cell Viability	ATP	1.00	0.00	<.0001
Cell Viability	D_SD	0.72	0.16	<.0001
Cell Viability	AVR	0.64	0.17	0.0001
Cell Viability	EdU	0.51	0.04	<.0001
Cell Viability	Ms_SD	0.47	0.23	0.0362
Cell Viability	LiveDead	0.42	0.03	<.0001
Cell Viability	DROACcc3	0.35	0.23	0.1202
Cell Viability	DROACcc4SD	-0.24	0.23	0.2934
Cell Viability	DROAC2	-0.56	0.16	0.0004
Cell Viability	Shift2	-0.84	0.14	<.0001
Cell Viability	Decay2SD	-1.32	0.19	<.0001
Cell Viability	SR	-1.48	0.15	<.0001
Cell Viability	DROAC4CV	-1.55	0.17	<.0001
Cell Viability	DROACcc3CV	-1.72	0.16	<.0001

Melittin				
Predictor	Outcome	Estimate	Std Error	Z-value
ATP	DROACcc3	1.32	0.58	0.0228
ATP	DROACcc4SD	-1.21	0.52	0.0194
ATP	DROAC4CV	-1.84	0.23	<.0001
ATP	DROACcc3CV	-2.03	0.22	<.0001
LiveDead	Mf_SD	-0.89	0.34	0.0092
LiveDead	DROACcc3	-2.04	0.71	0.004
LiveDead	Decorrelation	-2.79	0.25	<.0001
LiveDead	DROACcc4SD	-2.96	0.63	<.0001
LiveDead	Ms	-5.24	0.59	<.0001
Caspase	DROACcc3	1.88	0.67	0.005
Caspase	OAC_CV	1.02	0.32	0.0013
Caspase	OAC_SD	0.74	0.32	0.0228
Caspase	D_SD	-1.05	0.30	0.0005
Caspase	OACcc	-1.06	0.32	0.0008
Caspase	DROACcc4SD	-1.60	0.59	0.0069
Caspase	DopplerAbsSD	-2.38	0.25	<.0001
Caspase	Ms	-3.46	0.56	<.0001
EdU	SR	1.40	0.39	0.0003
EdU	DecorrelationCV	1.38	0.39	0.0004
EdU	D_SD	1.28	0.38	0.0007
EdU	Ms	1.14	0.30	0.0002
EdU	Mf_SD	1.03	0.39	0.0086
Cell Viability	DopplerAbsSD	2.05	0.23	<.0001
Cell Viability	D_SD	1.06	0.27	0.0001
Cell Viability	ATP	1.00	0.00	<.0001
Cell Viability	OACcc	0.92	0.28	0.0009
Cell Viability	LiveDead	0.80	0.04	<.0001
Cell Viability	SR	0.16	0.10	0.1288
Cell Viability	DecorrelationCV	0.16	0.10	0.1297
Cell Viability	EdU	0.11	0.07	0.0937
Cell Viability	Mf_SD	-0.59	0.28	0.0356
Cell Viability	OAC_SD	-0.64	0.28	0.0235
Cell Viability	Caspase	-0.86	0.04	<.0001
Cell Viability	OAC_CV	-0.88	0.28	0.0015
Cell Viability	Ms	-1.07	0.28	0.0001
Cell Viability	DROAC4CV	-1.84	0.23	<.0001
Cell Viability	DROACcc3	-1.92	0.26	<.0001
Cell Viability	DROACcc3CV	-2.03	0.22	<.0001
Cell Viability	DROACcc4SD	-2.18	0.22	<.0001
Cell Viability	Decorrelation	-2.23	0.22	<.0001

Cisplatin				
Predictor	**Outcome**	**Estimate**	**Std Error**	**Z-value**
ATP	Mf_SD	2.30	0.89	0.0099
ATP	DROACcc1CV	-2.88	0.74	0.0001
Caspase	Ms	0.32	0.05	<.0001
Caspase	Volume	0.27	0.06	<.0001
Caspase	SR	-0.25	0.06	<.0001
EdU	DopplerAbsCV	1.83	0.19	<.0001
EdU	D_SD	1.03	0.24	<.0001
EdU	DROAC1	0.83	0.24	0.0006
EdU	DROACcc3CV	-0.73	0.24	0.003
EdU	OACcc_CV	-0.92	0.24	0.0001
EdU	DecorrelationCV	-1.22	0.23	<.0001
EdU	DROACcc3	-1.27	0.23	<.0001
EdU	DROACcc1CV	-1.43	0.21	<.0001
Cell Viability	Caspase	1.00	0.00	<.0001
Cell Viability	DopplerAbsCV	0.36	0.06	<.0001
Cell Viability	Ms	0.32	0.05	<.0001
Cell Viability	Volume	0.27	0.06	<.0001
Cell Viability	D_SD	0.20	0.05	0.0002
Cell Viability	EdU	0.19	0.03	<.0001
Cell Viability	DROAC1	0.16	0.05	0.0018
Cell Viability	LiveDead	0.03	0.00	<.0001
Cell Viability	ATP	-0.03	0.01	<.0001
Cell Viability	Mf_SD	-0.07	0.03	0.0266
Cell Viability	DROACcc3CV	-0.14	0.05	0.0057
Cell Viability	OACcc_CV	-0.18	0.05	0.0006
Cell Viability	DROACcc1CV	-0.19	0.06	0.0022
Cell Viability	DecorrelationCV	-0.24	0.05	<.0001
Cell Viability	SR	-0.25	0.06	<.0001
Cell Viability	DROACcc3	-0.25	0.05	<.0001

Melphalan				
Predictor	**Outcome**	**Estimate**	**Std Error**	**Z-value**
ATP	SR	3.16	0.89	0.0004
ATP	D_SD	1.85	0.75	0.0135
ATP	OAC_CV	-1.91	0.92	0.0377
ATP	DROACcc3CV	-2.13	0.92	0.02
ATP	DROACcc1CV	-3.14	0.89	0.0004
LiveDead	D_SD	2.82	0.78	0.0003
LiveDead	Ms	1.30	0.61	0.0345
LiveDead	Decay2SD	-3.40	0.69	<.0001
LiveDead	Mf	-3.75	1.10	0.0006
Caspase	Decay2	0.96	0.45	0.0311
Caspase	Ms	-0.83	0.35	0.0186
Caspase	Mf	-1.95	0.63	0.002
EdU	Ms	2.41	0.17	<.0001
EdU	Mf	2.18	0.31	<.0001
EdU	D_SD	0.84	0.27	0.0016
EdU	AVR	-1.09	0.23	<.0001
EdU	DROACcc1SD	-1.60	0.20	<.0001
Cell Viability	Ms	17.00	3.77	<.0001
Cell Viability	D_SD	15.24	3.14	<.0001
Cell Viability	EdU	7.07	1.52	<.0001
Cell Viability	Caspase	4.14	0.89	<.0001
Cell Viability	Decay2	3.99	2.04	0.0504
Cell Viability	SR	3.16	0.89	0.0004
Cell Viability	LiveDead	2.64	0.56	<.0001
Cell Viability	ATP	1.00	0.00	<.0001
Cell Viability	OAC_CV	-1.91	0.92	0.0377
Cell Viability	DROACcc3CV	-2.13	0.92	0.02
Cell Viability	Mf	-2.54	2.26	0.2609
Cell Viability	DROACcc1CV	-3.14	0.89	0.0004
Cell Viability	AVR	-7.74	2.31	0.0008
Cell Viability	Decay2SD	-8.98	2.63	0.0006
Cell Viability	DROACcc1SD	-11.28	2.81	<.0001

Paclitaxel				
Predictor	**Outcome**	**Estimate**	**Std Error**	**Z-value**
ATP	Mf	-2.09	0.77	0.0064
LiveDead	OAC_SD	7.03	2.73	0.01
LiveDead	AVR	6.89	2.79	0.0135
LiveDead	Decay2CV	6.20	2.75	0.0244
LiveDead	OAC_CV	-6.30	2.80	0.0243
LiveDead	DROACcc3	-7.19	2.72	0.0082
LiveDead	DROAC4CV	-10.71	2.59	<.0001
EdU	D	1.46	0.26	<.0001
EdU	Mf	1.22	0.31	<.0001
EdU	AVR	1.06	0.30	0.0004
EdU	OAC_CV	-1.10	0.30	0.0002
EdU	DROACcc3	-1.12	0.29	0.0001
Cell Viability	Mf	3.78	0.84	<.0001
Cell Viability	AVR	3.04	0.77	<.0001
Cell Viability	D	2.96	0.79	0.0002
Cell Viability	EdU	2.03	0.40	<.0001
Cell Viability	Caspase	1.00	0.00	<.0001
Cell Viability	OAC_SD	0.92	0.41	0.0267
Cell Viability	Decay2CV	0.81	0.40	0.0457
Cell Viability	LiveDead	0.13	0.03	<.0001
Cell Viability	ATP	-0.62	0.12	<.0001
Cell Viability	DROAC4CV	-1.40	0.47	0.0028
Cell Viability	OAC_CV	-3.05	0.77	<.0001
Cell Viability	DROACcc3	-3.21	0.79	<.0001

A7. Data Processing Code

The following python code was utilized to analyze OCT metrics for Chapter 4 and to extract structural equation models. Raw OCT data was processed using custom MATLAB code developed by Dr. Jonghwan Lee.

```
# %%
import pandas as pd
import numpy as np
from pathlib import Path
from scipy import stats
from scipy.stats import shapiro
from sklearn.linear_model import LinearRegression
from sklearn.metrics import mean_squared_error, r2_score
import statsmodels.api as sm
from statsmodels.stats.outliers_influence import variance_inflation_factor
from statsmodels.tools.tools import add_constant
from sklearn.preprocessing import StandardScaler
from tqdm import tqdm
import matplotlib.pyplot as plt
# ================================================================",
# Functions for data processing and analysis
# ================================================================",
# Function to bootstrap to fill any missing data points
def bootstrap_fill_exposure_24(df, n_bootstrap=2000, min_group_size=3):
    """
    Specialized bootstrapping filler for exposure_24 DataFrame.
    Fills missing values by sampling within LC × Exposure groups.
    Parameters:
    - df: Your exposure_24 DataFrame
    - n_bootstrap: Number of bootstrap samples (default: 50)
    - min_group_size: Minimum available values needed (default: 3)
    Returns:
    - Filled DataFrame
    - Detailed statistics dictionary
    """
    # Make copy and initialize stats
    df_filled = df.copy()
    stats = {
        'columns_processed': [],
        'total_values_filled': 0,
        'values_remaining_missing': 0,
        'groups_processed': {},
        'warnings': []
    }
    # Identify columns with missing values (excluding group columns)
    group_cols = ['LC', 'Exposure']
    cols_with_missing = [col for col in df.columns
```

```
                        if col not in group_cols
                        and df[col].isnull().any()]
    if not cols_with_missing:
        print("No missing values found in any columns.")
        return df_filled, stats
    stats['columns_processed'] = cols_with_missing
    # Main processing loop
    for col in tqdm(cols_with_missing, desc="Processing columns"):
        for group_key, group in df.groupby(group_cols):
            group_id = f"LC={group_key[0]}, Exposure={group_key[1]}"
            # Initialize group stats if not exists
            if group_id not in stats['groups_processed']:
                stats['groups_processed'][group_id] = {
                    'filled': 0,
                    'skipped_small_group': 0,
                    'available_values': 0
                }
            available_values = group[col].dropna()
            stats['groups_processed'][group_id]['available_values'] =
len(available_values)
            # Skip if not enough values
            if len(available_values) < min_group_size:
                missing_count = group[col].isnull().sum()
                stats['groups_processed'][group_id]['skipped_small_group'] +=
missing_count
                stats['values_remaining_missing'] += missing_count
                continue
            # Fill missing values
            null_indices = group[group[col].isnull()].index
            for idx in null_indices:
                bootstrap_sample = np.random.choice(available_values,
size=n_bootstrap, replace=True)
                df_filled.loc[idx, col] = bootstrap_sample.mean()
                stats['groups_processed'][group_id]['filled'] += 1
                stats['total_values_filled'] += 1
    # Generate summary statistics
    stats['values_remaining_missing'] =
df_filled[cols_with_missing].isnull().sum().sum()
    # Add warnings for problematic groups
    for group_id, group_stats in stats['groups_processed'].items():
        if group_stats['available_values'] == 0:
            stats['warnings'].append(f"{group_id} had NO available values for
filling")
        elif group_stats['skipped_small_group'] > 0:
            stats['warnings'].append(
                f"{group_id} had {group_stats['skipped_small_group']} values
not filled "
                f"(only {group_stats['available_values']} available, needed
{min_group_size})"
            )
    return df_filled, stats
# ================================================================",
# Normality Check
# ================================================================",
```

```
def check_normality(df, alpha=0.05):
    """
    Checks the normality of each column in a Pandas DataFrame using the
Shapiro-Wilk test.
    Parameters:
    - df: Pandas DataFrame containing the data.
    - alpha: Significance level for the Shapiro-Wilk test (default: 0.05).
    Returns:
    - normality_results: A dictionary containing the Shapiro-Wilk test results
for each column.
    """
    for column in df.columns:
        data = df[column].dropna()  # Drop NaN values before testing
        if len(data) < 3:
            normality_results[column] = {
                'statistic': None,
                'pvalue': None,
                'normal': False,
                'warning': "Too few data points to perform Shapiro-Wilk test."
            }
            continue
        stat, p = shapiro(data)
        normality_results[column] = {
            'statistic': stat,
            'pvalue': p,
            'normal': p > alpha,
            'warning': None
        }
    return normality_results
# ================================================================",
# Regression Analysis
# ================================================================",
def perform_regression_analysis(predictors, targets, output_dir, condition,
significance_level=0.05):
    """
    Performs regression analysis and identifies significant predictors, saving
plots of the fits.
    Parameters:
    - predictors: DataFrame containing predictor variables.
    - targets: DataFrame containing target assays.
    - output_dir: Path to save regression results and plots.
    - condition: The current condition being processed.
    - significance_level: Threshold for p-values (default: 0.05).
    Returns:
    - results_df: DataFrame with regression results.
    - significant_predictors: Dictionary of significant predictors for each
assay.
    """
    regression_results = []
    significant_predictors = {}
    plt.rcParams.update({'font.size': 12})
    for assay in targets.columns:
        print(f"\n{'='*50}")
        print(f"Regression analysis for {assay}")
```

```
        print(f"{'='*50}")
        significant_predictors[assay] = []  # Initialize list for each assay
        for predictor in predictors.columns:
            # Prepare data for regression
            X = predictors[[predictor]]  # Single predictor
            y = targets[assay]  # Single target assay
            # Fit linear regression model
            model = LinearRegression()
            model.fit(X, y)
            # Make predictions
            y_pred = model.predict(X)
            # Calculate R^2
            r2 = r2_score(y, y_pred)
            # Calculate Mean Squared Error (MSE)
            mse = mean_squared_error(y, y_pred)
            # Statsmodels for p-values
            X_sm = sm.add_constant(X)  # Add a constant for the intercept
            model_sm = sm.OLS(y, X_sm)
            results_sm = model_sm.fit()
            p_value = results_sm.pvalues[predictor]  # P-value for the
predictor
            slope = model.coef_[0] # Extract the slope
            # Store results
            regression_results.append({
                'Assay': assay,
                'Predictor': predictor,
                'Slope': slope,
                'R^2': r2,
                'MSE': mse,
                'P-value': p_value
            })
            # Check for significance
            if p_value < significance_level:
                significant_predictors[assay].append(predictor)
                if r2 > 0.25:  # Optional: Only plot if R^2 is above a
threshold
                    # Calculate confidence interval using statsmodels' built
in method
                    predictions = results_sm.get_prediction(X_sm)
                    predictions_summary =
predictions.summary_frame(alpha=0.05)
                    # Select appropriate CI type (true regression line vs.
individual predictions)
                    use_mean_ci = True  # Set to False for prediction
intervals
                    if use_mean_ci:
                        lower_bound =
predictions_summary["mean_ci_lower"].values
                        upper_bound =
predictions_summary["mean_ci_upper"].values
                        ci_label = "95% Mean CI"
                    else:
                        lower_bound =
predictions_summary["obs_ci_lower"].values
```

```
                        upper_bound =
predictions_summary["obs_ci_upper"].values
                        ci_label = "95% Prediction CI"
                    # Sort values for clean CI plotting
                    sorted_idx = np.argsort(X.values.ravel())
                    X_sorted = X.values.ravel()[sorted_idx]
                    y_pred_sorted = y_pred[sorted_idx]
                    lower_sorted = lower_bound[sorted_idx]
                    upper_sorted = upper_bound[sorted_idx]
                    # Create and save the plot only if p-value is significant
                    plt.figure(figsize=(5, 5))
                    plt.scatter(X, y, alpha=0.5, label="Observed Data")
                    plt.plot(X_sorted, y_pred_sorted, color='red',
label="Regression Line")
                    plt.fill_between(X_sorted, lower_sorted, upper_sorted,
                                     color='gray', alpha=0.3, label=ci_label)
                    plt.xlabel(predictor)
                    plt.ylabel(assay)
                    plt.title(f"{assay} vs {predictor}\n(R² = {r2:.2f}, MSE =
{mse:.2f}, p = {p_value:.2e})")
                    plt.legend()
                    plt.xlim(-4,4)
                    plt.ylim(-1.5, 1.5)
                    plt.tight_layout()
                    plot_output_path = output_dir /
f'{condition}_{assay}_vs_{predictor}.svg'
                    plt.savefig(plot_output_path, dpi=300)
                    plt.close()  # Close the plot to free memory
    # Convert results to DataFrame
    results_df = pd.DataFrame(regression_results)
    return results_df, significant_predictors
# ================================================================",
# Structural Equation Modeling (SEM)
# ================================================================",
def build_sem_model(condition, top_predictors_by_assay, zscored_df,
output_dir):
    """
    Build and fit a Structural Equation Model (SEM) for a given condition.
    Parameters:
    - condition: The current condition being processed.
    - top_predictors_by_assay: Dictionary mapping assays to their top
predictors.
    - zscored_df: DataFrame containing z-scored data for SEM.
    - output_dir: Path to save SEM results and diagrams.
    Returns:
    - None
    """
    print(f"\nBuilding SEM model for {condition}...")
    # Define the SEM model
    sem_model_description = """
    Viability =~ ATP + LiveDead + EdU + Caspase
    Viability ~~ Viability
    """
    # Add relationships between each assay and its top predictors
```

```
    for assay, predictors in top_predictors_by_assay.items():
        for predictor in predictors:
            sem_model_description += f"{predictor} ~ {assay}\n"
    # Save SEM model description to a file
    sem_model_path = output_dir / f"{condition}_sem_model.txt"
    with open(sem_model_path, "w") as f:
        f.write(sem_model_description)
    # Prepare and fit the SEM model
    try:
        import semopy
        from semopy import Model
        sem_model = Model(sem_model_description)
        sem_model.fit(zscored_df)
    except Exception as e:
        print(f"Error fitting SEM model for {condition}: {e}")
        return
    # Inspect and save SEM results
    try:
        sem_results = sem_model.inspect()
        sem_results_path = output_dir / f"{condition}_sem_results.xlsx"
        pd.DataFrame(sem_results).to_excel(sem_results_path, index=False)
        print(f"SEM results saved to {sem_results_path}")
    except Exception as e:
        print(f"Error saving SEM results for {condition}: {e}")
    # Save SEM statistics
    try:
        import semopy
        sem_stats = semopy.calc_stats(sem_model)
        sem_stats_path = output_dir / f"{condition}_sem_stats.xlsx"
        sem_stats.to_excel(sem_stats_path, index=False)
        print(f"SEM statistics saved to {sem_stats_path}")
    except Exception as e:
        print(f"Error saving SEM statistics for {condition}: {e}")
    # Save predicted factors
    try:
        factors = sem_model.predict_factors(zscored_df)
        factors_path = output_dir / f"{condition}_sem_factors.xlsx"
    except Exception as e:
        print(f"Error saving SEM factors for {condition}: {e}")
    # Generate SEM path diagram
    try:
        import semopy
        semopy.semplot(sem_model, str(output_dir /
f"{condition}_sem_path_diagram.svg"))
        print(f"SEM path diagram saved to {output_dir /
f'{condition}_sem_path_diagram.svg'}")
    except Exception as e:
        print(f"Error generating SEM path diagram for {condition}: {e}")
    # Generate SEM report
    try:
        import semopy
        semopy.report(sem_model, str(output_dir /
f"SEMreport_{condition}.html"))
```

```
        print(f"SEM report saved to {output_dir /
f'SEMreport_{condition}.html'}")
    except Exception as e:
        print(f"Error generating SEM report for {condition}: {e}")
# Set output directory (will create if doesn't exist)
output_dir = Path("C:/Users/azein/Documents/PredictorAnalysis")
output_dir.mkdir(parents=True, exist_ok=True)
# Dictionary to store all results
results = {}
normality_results = {}
# ================================================================",
# Main Processing Loop
# ================================================================",
for condition in ['230428-2DG', '230428-OLI', '240614-CIS', '240614-MEF',
'240426-MEL' ,'240426-TRI', '240621-PAC']:
    drug = condition[-3:]
    # Load and prepare data
    path = 'R:/azeinsab/OCT Data/'+drug
    # Load excel file and filter for the 24-hour timepoint
    df=pd.read_excel(path+'/'+condition+'.xlsx')
    exposure_24_df=df[df['Exposure']==24]
    exposure_24_df.head()
    # Execute on your exposure_24 DataFrame
    filled_exposure_24, fill_stats =bootstrap_fill_exposure_24(exposure_24_df)
    # Display summary results
    print("\n=== Bootstrapping Completion Summary ===")
    print(f"Filled {fill_stats['total_values_filled']} missing values")
    print(f"{fill_stats['values_remaining_missing']} values remain missing")
    print(f"\nProcessed columns: {fill_stats['columns_processed']}")
    if fill_stats['warnings']:
        print("\n=== Warnings ===")
        for warning in fill_stats['warnings']:
            print(f"- {warning}")
    # ================================================================",
    # Normalization of Target Assay Outputs
    # ================================================================",
    # Normalize specific columns based on the mean of rows where 'LC' == 0
    columns_to_normalize = ['ATP', 'LiveDead', 'EdU', 'Caspase']
    # Calculate the mean for each column where 'LC' == 0
    lc0_means = filled_exposure_24[filled_exposure_24['LC'] ==
0][columns_to_normalize].mean()
    # Normalize the specified columns
    normalized_df = filled_exposure_24.copy()
    normality_results = check_normality(normalized_df)
    for column, result in normality_results.items():
        print(f"Column: {column}")
        if result['warning']:
            print(f"  Warning: {result['warning']}")
        else:
            print(f"  Shapiro-Wilk Statistic: {result['statistic']:.3f}")
            print(f"  P-value: {result['pvalue']:.3f}")
            print(f"  Normally distributed: {result['normal']}")
        print("-" * 30)
    # Apply standard normalization for ATP, LiveDead, and EdU
```

```
    for col in ['ATP', 'LiveDead', 'EdU']:
        normalized_df[col] = filled_exposure_24[col] / lc0_means[col]
    # Apply inverted normalization for Caspase
    normalized_df['Caspase'] = 1 - (filled_exposure_24['Caspase'] /
lc0_means['Caspase'])
    # Save the normalized DataFrame to a new variable or file if needed
    normalized_df.to_excel(path + '/Normalized_' + condition + '.xlsx',
index=False)
    # ================================================================",
    # Prepare z-scored data
    # ================================================================",
    zscored_df = normalized_df.copy()
    exclude_cols = ['LC', 'Exposure', 'SpheroidNo', 'ATP', 'Caspase',
'LiveDead', 'EdU']
    scaled_cols = [col for col in normalized_df.columns if col not in
exclude_cols]
    scaler = StandardScaler()
    zscored_df[scaled_cols] = scaler.fit_transform(normalized_df[scaled_cols])
    zscored_df.to_excel(path + '/ZScored_' + condition + '.xlsx', index=False)
    # Extract predictors and targets from the z-scored data
    predictors = zscored_df.drop(
        ['ATP', 'Caspase', 'LiveDead', 'EdU', 'LC', 'Exposure', 'SpheroidNo'],
        axis=1
    )
    targets = zscored_df[['ATP', 'Caspase', 'LiveDead', 'EdU']]
    # ================================================================",
    # Variance Inflation Factor (VIF) Analysis
    # ================================================================",
    print("\nPerforming Variance Inflation Factor (VIF) analysis...")
    vif_threshold = 5
    predictors_filtered = predictors.copy()
    while True:
        # Add a constant to the predictors (required for VIF calculation)
        X = add_constant(predictors_filtered)
        # Calculate VIF for each predictor
        vif_data = pd.DataFrame()
        vif_data["Feature"] = X.columns
        vif_data["VIF"] = [variance_inflation_factor(X.values, i) for i in
range(X.shape[1])]
        # Remove the constant column from the VIF data
        vif_data = vif_data[vif_data['Feature'] != 'const']
        # Check if any VIF values exceed the threshold
        if (vif_data['VIF'] <= vif_threshold).all():
            break  # Exit the loop if all VIFs are below the threshold
        # Find the feature with the highest VIF
        highest_vif_feature = vif_data.loc[vif_data['VIF'].idxmax(),
'Feature']
        # Remove the feature with the highest VIF from the predictors
        predictors_filtered = predictors_filtered.drop(highest_vif_feature,
axis=1, errors='ignore')
        print(f"\nRemoved high VIF feature: {highest_vif_feature}")
        print(f"Remaining features after VIF analysis:
{predictors_filtered.columns.tolist()}")
        # If no predictors remain, exit the loop
```

```
        if predictors_filtered.shape[1] == 0:
            print("No predictors remaining after VIF filtering.")
            # Provide at least one predictor to pass to the next section
            if predictors.shape[1] > 0:
                # Recalculate VIFs on the original set of predictors
                X_original = add_constant(predictors)
                vif_data_original = pd.DataFrame()
                vif_data_original["Feature"] = X_original.columns
                vif_data_original["VIF"] =
[variance_inflation_factor(X_original.values, i) for i in
range(X_original.shape[1])]
                vif_data_original =
vif_data_original[vif_data_original['Feature'] != 'const']
                # Find the feature with the lowest VIF in the original set
                lowest_vif_feature =
vif_data_original.loc[vif_data_original['VIF'].idxmin(), 'Feature']
                predictors_filtered = predictors[[lowest_vif_feature]].copy()
                print(f"Using the predictor with the lowest VIF:
{lowest_vif_feature}")
            break
    # Save VIF results to a file
    vif_output_path = output_dir / f'{condition}_vif_results.xlsx'
    vif_data.to_excel(vif_output_path, index=False)
    print(f"VIF results saved to {vif_output_path}")
    # ======================================================================\",
    # Regression Analysis
    # ======================================================================\",
    print("\nPerforming Regression Analysis...")
    regression_results_df, significant_predictors =
perform_regression_analysis(predictors_filtered, targets, output_dir,
condition)
    # Filter regression results for significant predictors
    filtered_results = []
    for index, row in regression_results_df.iterrows():
        assay = row['Assay']
        predictor = row['Predictor']
        p_value = row['P-value']
        if predictor in significant_predictors.get(assay, []) and p_value <=
0.05:
            filtered_results.append(row)
    significant_results = pd.DataFrame(filtered_results)
    # Save regression results to a file
    regression_output_path = output_dir /
f'{condition}_regression_results.xlsx'
    if not significant_results.empty:
        significant_results.to_excel(regression_output_path, index=False)
    else:
        print("No significant results to save.")
    print(f"Regression results saved to {regression_output_path}")
    # ======================================================================\",
    # Structural Equation Modeling (SEM) with Assays and Top Predictors
    # ======================================================================\",
    # Ensure output directory exists
    condition_output_dir = output_dir / condition
```

```
    condition_output_dir.mkdir(parents=True, exist_ok=True)
    # Build and fit SEM model for the current condition
    build_sem_model(condition, significant_predictors, zscored_df,
condition_output_dir)
```

END